Accurate Prediction of Chiroptical Properties

Taylor J. Mach

Dissertation submitted to the Faculty of the

Virginia Polytechnic Institute and State University

in partial fulfillment of the requirements for the degree of

Doctor of Philosophy

in

Chemistry

T. Daniel Crawford, Chair

Paul A. Deck

Diego Troya

Edward F. Valeev

April 21, 2014

Blacksburg, Virginia

Keywords: Optical Rotation, Coupled Cluster, Gauge Invariance, N-Body

Accurate Prediction of Chiroptical Properties

Taylor J. Mach

(ABSTRACT)

Accurate theoretical predictions of optical rotation are of substantial utility to the chemical community enabling the determination of absolute configuration without the need for potentially lengthy total synthesis. The requirements for robust calculation of gas-phase optical rotation are well understood, but too expensive for routine use. In an effort to reduce this cost we have examined the performance of the LPol and ORP basis sets, created for use in density functional theory calculations of optical rotation, finding that at the coupled cluster level of theory they perform the same or better than comparably sized general basis sets that are often used.

We have also examined the performance of a perturbational approach to inclusion of explicit solvent molecules in an effort to extend the calculation of response properties from the gas

phase to the condensed phase. This N-body approach performs admirably for interaction energies and even dipole moments but breaks down for optical rotation, exhibiting large basis set superposition errors and requiring higher-order terms in the expansion to provide reasonable accuracy.

In addition, we have begun the process of implementing a gauge invariant version of coupled cluster response properties to address the fundamentally unphysical lack of gauge invariance in coupled cluster optical rotations. Correcting this problem, which arises from the non-variational nature of the coupled cluster wavefunction, involves reformulating the response amplitude and function expressions and solving for all necessary amplitudes simultaneously.

This work was supported by grants from the U.S. National Science Foundation: CHE-0715185, CHE-1058420, and a Multi-User Chemistry Research Instrumentation and Facility (CRIF:MU) award CHE-0741927, as well as by a graduate fellowship from the Institute for Critical Technology and Applied Science (ICTAS) at Virginia Tech.

Acknowledgments

There are many people who have been integral in my development as a scientist and person. There are far too many to name them all, and even more whose influence is not yet realized or fully appreciated.

⋆ John Severson for making my initial encounter with chemistry enthralling and intellectually rigorous.

⋆ Mom and Dad Bruns for unconditionally accepting me into their family despite stealing their daughter (and taking her 1200 miles away).

⋆ Mom and Dad Mach for having high standards and strict rules, while allowing me immense freedom.

⋆ Suzan Mauney for giving me free reign to try things, make mistakes, and enjoy the wonders of physical science with her 8^{th} graders, as well as staying late (even on Fridays) to talk education with me.

⋆ Theoretical chemistry colleagues at Virginia Tech during my tenure including: Florian

Bischoff, Ryan Fortenberry, Ashutosh Kumar, Harley McAlexander, and Ben Mintz, for discussions that often led to breakthroughs, bridging the gaps in research productivity, and making conference travel infinitely more adventurous.

⋆ My research advisors Rollin King and Daniel Crawford for their immense investment of time, patience, and instruction without which this work would not have been possible. Their constant support and respect for me as a colleague despite my clear inferiority has made a lasting impact.

⋆ Harley McAlexander deserves special thanks, in addition to that above, for being a wonderful housemate, putting up with innumerable food experiments and their constant odor (too bad he never started that blog. . .), early morning elephant feet, thermostat madness, and always being willing to have lengthy dinner conversations.

⋆ Mandy Mach, my constant companion and partner in crime, for always being up for an adventure, being contagiously awesome, and keeping my head on straight through the tough times. I couldn't have done it without her! She's also a Microsoft Office® wizard, one example of her work can be seen in Figure 1.3.

Attribution

The majority of Section 4.1 was completed during the summer and early fall of 2010 with a visiting undergraduate researcher Grant Lindh. I wrote the code that enabled OOCCD optical rotation calculations and served as his primary mentor assisting him with the calculations, data analysis, and determination of which systems should be studied. I also ran some of the calculations myself including all those on the stretched (*S*)-methyloxirane system.

Contents

List of Figures

List of Tables

Chapter 1

Introduction

Chiral molecules have very low symmetry; in the language of group theory they are defined as lacking an improper axis of rotation, which precludes them from having inversion symmetry or containing a mirror plane.[1] Human hands are a simple example of a pair of enantiomers, non-superposable mirror images, as no matter how they are twisted or rotated one can never be superposed upon the other. Chemically, two enantiomers have the same connectivity, meaning the exact same number and type of bonds; however, the bonds of each are arranged spatially in a different three-dimensional configuration. In organic compounds this arrangement often manifests itself as four different groups bonded to a central carbon atom. This stereogenic center (the carbon atom)[2] can be labeled (*R*) or (*S*) using the Cahn-Ingold-Prelog naming convention which prioritizes the bonded groups based on atomic number.[3] (*R*) or (*S*) [*rectus* and *sinister* from the Latin for right and left] is determined by tracing the priorities of the highest three groups (with the fourth group facing back) in a

Figure 1.1: Enantiomers of bromo-chloro-fluoro-methane. The group of lowest priority (hydrogen) is oriented to the back and is hidden from view by the central carbon atom. The order of priority of the remaining groups from highest to lowest is as follows, bromine (maroon), chlorine (green), and fluorine (ivory).

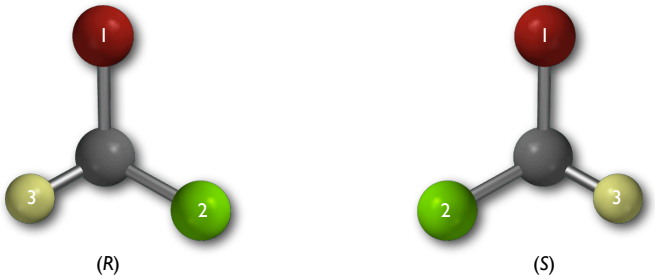

circular manner from highest to lowest clockwise or counterclockwise respectively. A simple example of a chiral system, bromo-chloro-fluoro-methane, is shown in Figure 1.1. The groups are labeled with their priorities and the enantiomers' (R) and (S) designations are shown.

Identical chemical composition means enantiomers have many of the same physical properties such as melting point, boiling point, and density; but their chemical reactivity in a chiral environment such as the human body is distinct ranging from the mundane creation of differing olfactory responses, to extremely deleterious birth defects as shown in Figure 1.2. The "handedness"[4] of each enantiomer also impacts optical properties through preferential scattering or absorption of the left- and right-circularly polarized components of incident light, giving rise to the properties of circular birefringence, electronic and vibrational circular dichroism, and raman optical activity.[5]

Circular birefringence, commonly known as optical rotation, is the rotation of plane polarized

Figure 1.2: Enantiomers of several compounds having various properties. The colors correspond to atom type as follows, carbon (grey), nitrogen (blue), oxygen (red), sulfur (yellow), and hydrogen (white). (a) A form of penicillin, 6-aminopenicillinic acid, one enantiomer has antibiotic properties, while the other does not. (b) The enantiomers of limonene have characteristically different scents; the (R) enantiomer smells of citrus fruits, while the (S) enantiomer smells like turpentine. (c) The most serious example included here, thalidomide, has drastically different properties; the (S) enantiomer is a teratogen (chemical that causes birth defects), while the (R) enantiomer is a mild sedative.

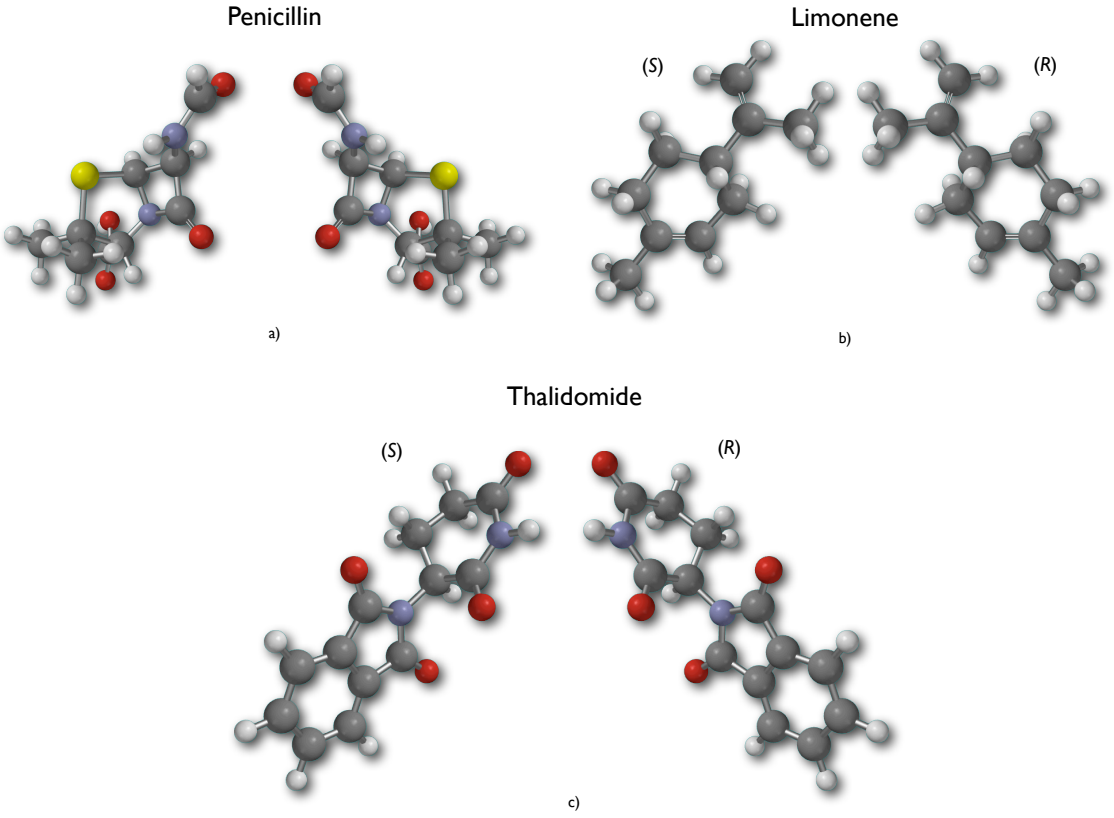

light caused by differences in an enantiomer's indices of refraction for left- and right-circularly polarized light (n_L and n_R respectively). This rotation

$$\alpha = \frac{\pi}{\lambda}(n_L - n_R) \tag{1.1}$$

is inversely proportional to the wavelength (λ) of incident light, and is typically normalized for sample concentration and path length, being reported as the specific rotation (in deg dm^{-1} $(\mathrm{g/mL})^{-1}$)

$$[\alpha]_\lambda = \frac{\alpha V}{ml} \tag{1.2}$$

where m is the mass of optically active sample contained in the volume V, and l is the path length of sample traversed by the light.

In 1928 Rosenfeld demonstrated,[6] using time-dependent perturbation theory, that the rotation per unit length could be written as

$$\phi = \frac{16\pi^3}{c^2} N\omega^2\beta. \tag{1.3}$$

In the above expression (Equation (1.3)) N is the number density of molecules and β is the mixed electric- and magnetic-dipole tensor

$$\beta = \frac{1}{3\pi h} \sum_{n \neq g} \frac{\mathrm{Im}(\langle g| \boldsymbol{\mu} |n\rangle \cdot \langle n| \mathbf{m} |g\rangle)}{\omega_{gn}^2 - \omega^2} \tag{1.4}$$

where $\boldsymbol{\mu} = e\sum_i \mathbf{r}_i$ and $\mathbf{m} = \frac{e}{2mc}\sum_i \mathbf{r}_i \times \mathbf{p}_i$ are the electric- and magnetic-dipole operators respectively. The Im refers to the fact that only the imaginary portions of the sum are retained, g denotes the ground state, n runs over all excited state wavefunctions, ω is the

frequency of incident radiation, ω_{gn} is the excitation energy, and c is the speed of light.[7] The explicit summation over excited states in Equation (1.4) is avoided in practice through the use of a linear response formalism as discussed in Section 4.2.1.[8]

Figure 1.3: Schematic of a polarimeter for measuring optical rotations of solution-phase samples.

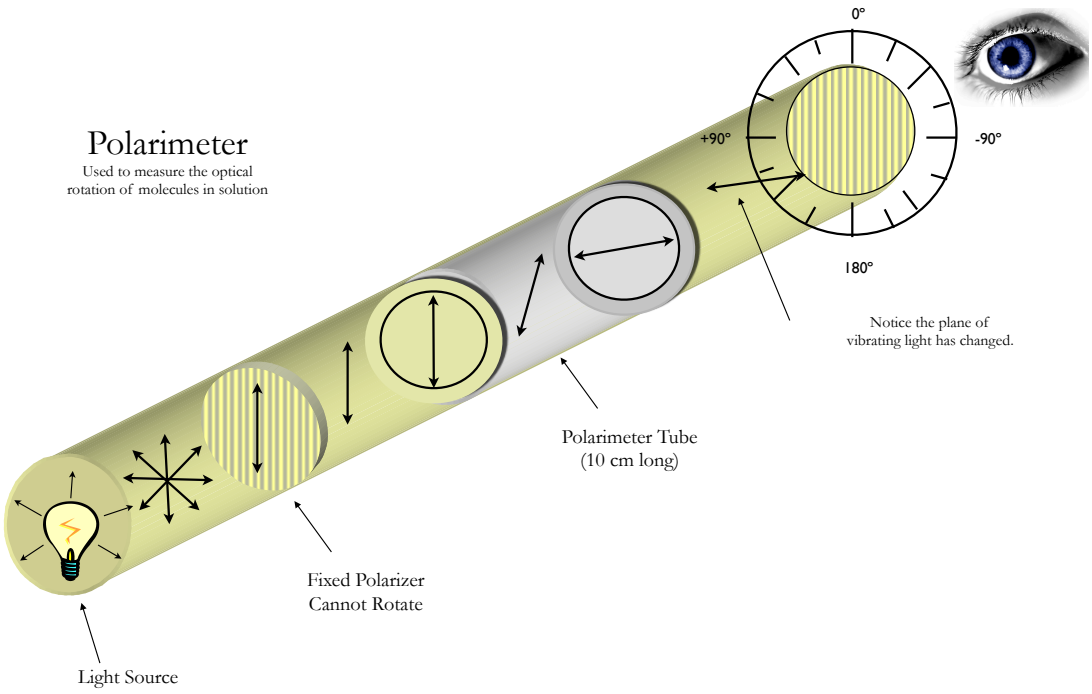

Figure 1.3 shows a simplified graphic of the apparatus used to measure optical rotation. The angle of rotation of the plane polarized light is reported from the perspective of the viewer facing the light source with a clockwise rotation denoted as positive and a counterclockwise rotation being denoted negative. The rotations produced by enantiomers are diametric opposites, *i.e.* if one enantiomer has a specific rotation of +50 deg dm^{-1} $(g/mL)^{-1}$, then

the other's specific rotation will be exactly -50 deg dm^{-1} (g/mL)$^{-1}$, where the sign refers to the direction of rotation, clockwise and counterclockwise respectively.

The binary nature of both the rotation directions and the enantiomer naming convention, as well as the manner in which the name is determined, suggests that a relationship exists between a molecule's absolute configuration and the direction (at least) of its optical rotation. However, no simple relationship between the two or even chemical intuition about the sign or magnitude of rotation has been established. Currently, to confirm the identity of a chemical via optical rotation, its optical rotation must be known *a priori* through measurement of a previously synthesized or isolated sample of known configuration. Theoretical chemistry is uniquely positioned in this respect to study this phenomenon at the molecular level, analyzing the contributions of individual excited states, conformers, or even specific portions of molecules to begin to understand optical rotation at the most fundamental level. It is with this ultimate goal in mind that the following work has been pursued to advance the theoretical foundations of the quantum chemical calculation of optical rotation.

Chapter 2

Theoretical Foundations

The basis of all quantum mechanical prediction lies in the solution of the Schrödinger equation

$$H\Psi = E\Psi \tag{2.1}$$

where H is the Hamiltonian,

$$H = -\frac{1}{2}\sum_{i=1}^{N}\nabla_i^2 - \sum_{A=1}^{M}\frac{1}{2M_A}\nabla_A^2 - \sum_{i=1}^{N}\sum_{A=1}^{M}\frac{Z_A}{r_{iA}} + \sum_{i=1}^{N}\sum_{j>i}^{N}\frac{1}{r_{ij}} + \sum_{A=1}^{M}\sum_{B>A}^{M}\frac{Z_A Z_B}{R_{AB}}, \tag{2.2}$$

Ψ is the wavefunction, and E is the energy. In Equation (2.2) uppercase indices refer to nuclei and lowercase to electrons, M_A and Z_A are the mass and charge of nucleus A respectively, r defines the electron coordinates, and R defines the nuclear positions. Solving this particular eigenvalue equation is exceedingly difficult. In fact, the electron-electron repulsion term (4^{th} term) of the Hamiltonian makes obtaining an analytic solution impossible for any system with two or more electrons.

For such systems a series of approximations is necessary, the most fundamental of which is the Born-Oppenheimer, or clamped nuclei, approximation.[9] This approximation simplifies the problem by assuming that the nuclei are fixed, ordinarily a valid assumption due to their slow motion relative to that of the electrons. Thus the nuclear kinetic energy is zero, and the nuclear-nuclear repulsion energy is a constant. The resulting eigenvalue equation is the electronic Schrödinger equation,

$$H_{\text{elec}}\Psi_{\text{elec}} = E_{\text{elec}}\Psi_{\text{elec}} \tag{2.3}$$

$$H_{\text{elec}} = -\frac{1}{2}\sum_{i=1}^{N}\nabla_i^2 - \sum_{i=1}^{N}\sum_{A=1}^{M}\frac{Z_A}{r_{iA}} + \sum_{i=1}^{N}\sum_{j>i}^{N}\frac{1}{r_{ij}} \tag{2.4}$$

where H_{elec} is now the electronic Hamiltonian, Ψ_{elec} is the electronic wavefunction, and E_{elec} is the electronic energy. From this point forward the subscript "elec" is dropped from all terms and all mention of the Schrödinger equation, Hamiltonians, wavefunctions, and energies are implicitly of the electronic persuasion.

2.1 Hartree-Fock Theory

Hartree-Fock theory is an approximate solution to the Schrödinger equation in which the wavefunction is constructed through variational minimization of the energy while maintaining orthonormality amongst the spin orbitals.[9] This optimization produces a set of functions that are linear combinations of the input basis functions (atomic orbitals) commonly referred to as molecular orbitals. The resulting wavefunction is a single Slater determinant made up

of the lowest energy molecular orbitals, and due to the variational nature of the optimization the energy is an upper bound to the true energy. The remaining molecular orbitals are unoccupied and of no consequence in Hartree-Fock theory, but will be used to incorporate the missing electron-electron interactions or correlation in higher levels of theory discussed below.

2.2 Coupled Cluster Theory

In the 1960's Čížek and Paldus published[10,11] a method of accounting for electron correlation by adding substituted determinants to a reference determinant, $|R\rangle$, (often from Hartree-Fock) via an exponential scheme

$$|\Psi_{\mathrm{CC}}\rangle = e^{T}\,|R\rangle\,, \tag{2.5}$$

where T is a substitution operator that contains single substitutions (T_1), double substitutions (T_2), and so on up to n-tuple substitutions (T_n) where n is the number of electrons in the system

$$T = T_1 + T_2 + \cdots + T_n. \tag{2.6}$$

The coupled cluster (CC) Schrödinger equation

$$He^{T}\,|R\rangle = Ee^{T}\,|R\rangle \tag{2.7}$$

is solved by projecting on the left by the reference, $\langle R|$, and substituted determinants, $\langle \nu|$, to obtain expressions for the energy and cluster amplitudes (substitution coefficients)

respectively. In order to decouple the amplitude equations from the energy equation it is customary to multiply Equation (2.7) on the left by e^{-T}

$$e^{-T}He^{T}\left|R\right\rangle = e^{-T}Ee^{T}\left|R\right\rangle \tag{2.8}$$

before projection.

The exponentials on the right hand side cancel, and those on the left form a similarity transformation of H typically represented as $\overline{H}$. Projecting and writing the resulting expressions in terms of $\overline{H}$ yields an equation for the energy

$$E = \left\langle R\right|\overline{H}\left|R\right\rangle \tag{2.9}$$

and one for the cluster amplitudes

$$0 = \left\langle \nu\right|\overline{H}\left|R\right\rangle . \tag{2.10}$$

While succinct, the above expressions (Equations (2.9) and (2.10)) do not give any indication of their practical solution. Using the power series expansion of an exponential

$$e^{T} = 1 + T + \frac{T^{2}}{2!} + \frac{T^{3}}{3!} + \cdots \tag{2.11}$$

and its inverse

$$e^{-T} = 1 - T + \frac{T^{2}}{2!} - \frac{T^{3}}{3!} + \cdots \tag{2.12}$$

to explicitly write out $\overline{H}$ appears to make the equation unmanageable

$$\overline{H} = H + HT + H\frac{T^{2}}{2!} - TH - THT - TH\frac{T^{2}}{2!} + \frac{T^{2}}{2!}H + \frac{T^{2}}{2!}HT + \frac{T^{2}}{2!}H\frac{T^{2}}{2!} + \cdots . \tag{2.13}$$

However, rearranging the terms enables rewriting Equation (2.13) as a commutator series

$$\overline{H} = H + [H,T] + \frac{1}{2!}[[H,T],T] + \frac{1}{3!}[[[H,T],T],T] + \frac{1}{4!}[[[[H,T],T],T],T] \quad (2.14)$$

known as the Campbell-Baker-Hausdorff expansion,[12] which due to the two-electron nature of the Hamiltonian and the pure excitation nature of T truncates at the fourth order commutator.

At this point the T operator must be defined algebraically to make further progress towards meaningful solutions to Equations (2.9) and (2.10). Considering the action of the T operator on a determinant leads to a simple algebraic definition. In the case of T_1 a single occupied orbital in the reference wavefunction is replaced by a single unoccupied orbital. This behavior is easily represented using second quantized operators

$$T_1 = \sum_{\substack{i \\ a}} t_i^a a_a^\dagger a_i, \quad (2.15)$$

where $a_a^\dagger$ creates unoccupied orbital a, a_i destroys occupied orbital i, and t_i^a is the probability of this substitution. In the case of the double substitution operator, T_2, two occupied orbitals are destroyed and replaced by the creation of two unoccupied orbitals

$$T_2 = \frac{1}{4}\sum_{\substack{ij \\ ab}} t_{ij}^{ab} a_a^\dagger a_b^\dagger a_j a_i. \quad (2.16)$$

The Hamiltonian can also be represented in second quantized form as

$$H = \sum_{pq} F_{pq} a_p^\dagger a_q + \frac{1}{4}\sum_{pqrs} \langle pq||rs\rangle \, a_p^\dagger a_q^\dagger a_s a_r, \quad (2.17)$$

where F is the Fock matrix

$$F_{pq} = \langle p| \, h \, |q\rangle + \frac{1}{2}\sum_m \langle pm||qm\rangle \quad (2.18)$$

and $\langle pq||rs\rangle$ is an anti-symmetric two-electron integral

$$\langle pq||rs\rangle = \langle pq|rs\rangle - \langle pq|sr\rangle \,. \tag{2.19}$$

In Equation (2.18) h is the one-electron component of the Hamiltonian.

The above expressions (and those that follow) adopt an index convention of $i, j, k, \ldots$ for occupied orbitals, $a, b, c, \ldots$ for unoccupied orbitals, and $p, q, r, \ldots$ for those from the entire space of occupied and unoccupied orbitals.

The above definitions of the operators enable the evaluation of the energy and amplitude expressions (Equations (2.9) and (2.10)) algebraically, but evaluating the commutators between long strings of creation and annihilation operators explicitly can be tedious and error prone. Various algebraic techniques exist that accelerate this evaluation, such as Wick's theorem[12] and utilizing generators of the unitary group.[13] However, these methods still require many algebraic manipulations and the creation and collection of equivalent terms. Coupled cluster diagrams eliminate this redundancy reducing the opportunity for error and are a particularly powerful method of arriving at programmable algebraic expressions.

2.2.1 Coupled Cluster Diagrams

To the newcomer, diagrams may be intimidating because they have no relation to any commonly used mathematical tools learned previously. However, diagrams are just a pictorial representation of matrix elements that can be interpreted into algebra using simple rules. Using diagrammatics successfully consists of three distinct phases of thinking — diagram

fragment determination, connection and labeling of fragments in all unique topologically allowed ways, and algebraic interpretation — and is best done algorithmically, that is by following a consistent pattern.

Each operator has a diagrammatic representation, for instance the T_1 operator (Figure 2.1) has two vertical lines that meet at an interaction line. The incoming line (according to the

Figure 2.1: Diagrammatic representation of the T_1 operator.

arrows) represents the annihilation operator, a_i, and the outgoing line represents the creation operator, $a_a^\dagger$, in Equation (2.15). The T_2 operator (Figure 2.2) is very similar having two

Figure 2.2: Diagrammatic representation of the T_2 operator.

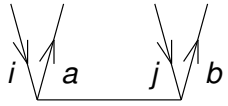

incoming lines and two outgoing lines representing the four second quantized operators in Equation (2.16)

The Hamiltonian has many possible diagram pieces due to the general orbital spaces it encompasses. The Fock matrix pieces (Figure 2.3) are similar to the T_1 in that they have two lines associated with annihilation/creation, while the two-electron integral pieces have four (Figure 2.4).

Figure 2.3: Diagrammatic representation of the Fock operator.

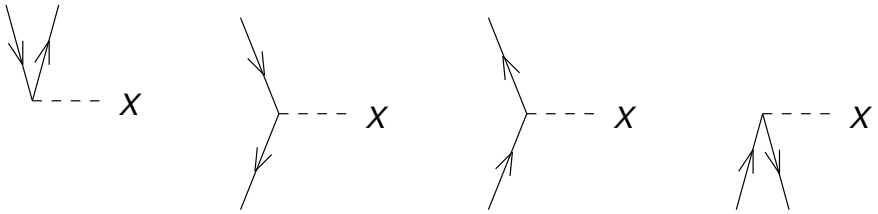

Which of the above fragments are used in a diagram is determined by the operators and determinants of each matrix element. In addition, matrix elements also contain information about diagram connectivity and topology. Each commutator in the matrix element enforces a connection via at least one annihilation or creation line between the two involved operators. The overall structure of the diagram (its topology) is based on the substitution level of the matrix element determinants, with each level contributing a pair of lines extending beyond the diagram. Diagrams are drawn from bottom to top according to the matrix element from right to left, *i.e.* the bottom of the diagram represents the right matrix element and the top the left. All unique diagrams that meet the connectivity requirements for each topology contribute to the matrix element. Again, the enumerated steps may seem confusing, but if done systematically diagram drawing is simple. For example, starting with the double commutator term of Equation (2.9)

$$\langle R| \overline{H} |R\rangle \leftarrow \frac{1}{2} \langle R| [[H,T],T] |R\rangle \tag{2.20}$$

and converting the commutator into the diagram connectivity yields

$$\langle R| [[H,T],T] |R\rangle = \langle R| (HTT)_c |R\rangle \tag{2.21}$$

Figure 2.4: Diagrammatic representation of the two-electron integral operator.

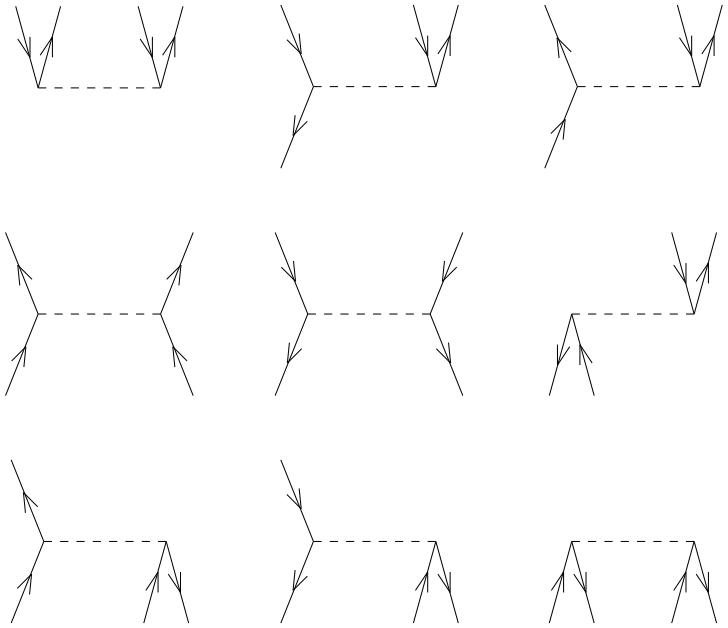

where the subscript c denotes that each T must be connected to the Hamiltonian by at least one creation or annihilation line. In this case only Figure 2.5 satisfies the connectivity requirements and has no lines extending above or below the diagram (reference for the left and right determinants).

Figure 2.5: Diagram representing the quadratic T_1 contribution to the coupled cluster correlation energy.

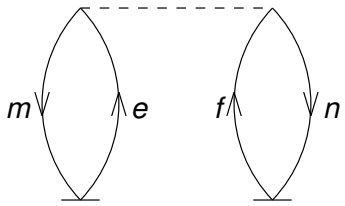

Diagrams for the amplitude equations (Equation (2.10)) are determined in the same manner, where the only difference is the presence of lines extending above the diagrams. One of the

contributing terms to the doubles amplitudes arises due to the single commutator of the Hamiltonian with T

$$\langle D|\,\overline{H}\,|R\rangle \leftarrow \langle D|\,[H,T]\,|R\rangle \tag{2.22}$$

$$\langle D|\,[H,T]\,|R\rangle = \langle D|\,(HT)_c\,|R\rangle\,, \tag{2.23}$$

where $\langle D|$ is a doubly excited determinant. This matrix element has seven unique possibilities that satisfy the topology and connectivity diagrammatically. The first two (Figure 2.6) involve a T_1 connected to the Hamiltonian by a single creation or annihilation line, two

Figure 2.6: Doubles amplitude diagrams involving a two-electron integral and T_1.

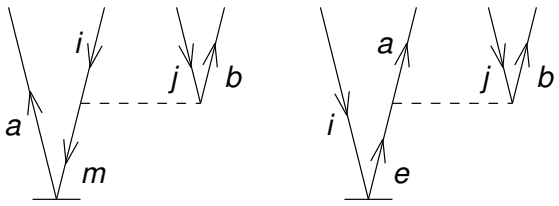

others involve F and T_2 (Figure 2.7), and the remaining have two-electron integrals connected

Figure 2.7: Doubles amplitude diagrams arising from the Fock matrix and T_2.

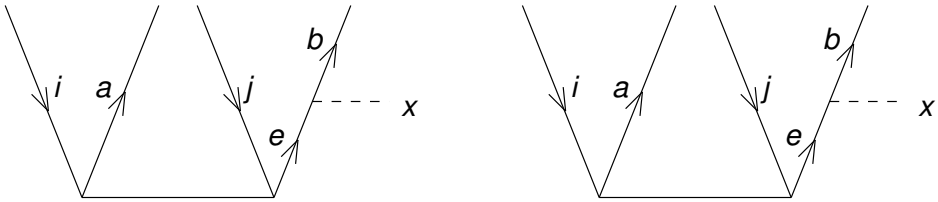

by creation lines, annihilation lines, or both to a T_2 (Figure 2.8). In each case there is a single T operator connected by at least one line to the Hamiltonian fragment, two pairs

Figure 2.8: Diagrams contributing to the doubles amplitudes containing a two-electron integral and a single T_2 operator.

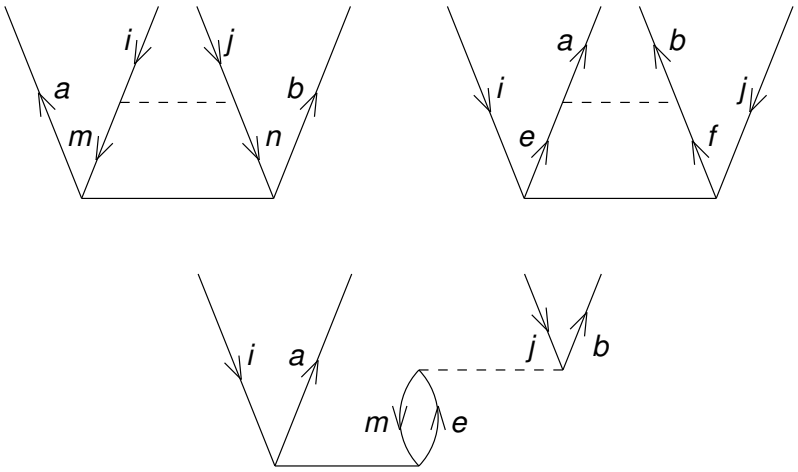

of lines extending above the diagram (doubly substituted determinant), and no lines below (reference). The annihilation and creation lines in the diagrams shown above are labeled according to a convenient convention that makes interpretation quick and easy. External lines are labeled from left to right starting with i and a for annihilation and creation respectively and internal lines are labeled from left to right starting with m and e. This disjoint index convention makes internal and external lines obvious at a glance, limits indexing errors, and goes along with the left to right interpretation outlined below.

Once all the unique diagrams are drawn and labeled they must be interpreted algebraically using the seven rules of CC diagrams.

Sign The sign of the diagram is positive if the number of annihilation lines (down arrows) plus the number of loops (a pair of annihilation and creation lines that start and end at the same point — interaction line or determinant) is

even and negative if the sum is odd.

Prefactor Each pair of equivalent lines, that is a pair of lines that start and end on the same interaction line, contributes a factor of $\frac{1}{2}$ to the diagram prefactor.

Prefactor In addition, pairs of interaction lines that have identical connectivity (equivalent vertices) contribute a factor of $\frac{1}{2}$ to the prefactor.

Summation Internal lines, those that go from an interaction line to an interaction line, are summed over.

Integral The integral operators (Fock and two-electron) are interpreted as elements of a matrix where the line entering the interaction line is first followed by the line leaving the interaction line. In the case of two-electron integrals this amounts to left-out, right-out, left-in, right-in.

T Operator Each T operator gives rise to its own cluster amplitude coefficient. The annihilation lines (occupied orbitals) are evaluated as the subscripts and creation (unoccupied) as the superscripts of that coefficient. This is typically done from left to right through the diagram.

Permutation The final rule deals with external lines (lines extending beyond the diagram) and is only an issue in diagrams contributing to the doubles (and higher) amplitudes. If external lines of the same type (annihilation or creation) originate on different interaction lines they are termed nonequivalent external

lines. Each pair of nonequivalent external lines contributes a permutation operator for those indices, P_{ab}, that creates a second algebraic term with the two indices permuted and the opposite sign.

The energy diagram (Figure 2.5) above has two annihilation lines and two loops (each pair of lines connecting a T_1 is a loop); since four is even, the sign of the diagram is positive. There are no equivalent lines in the diagram, but the two T_1's make up a pair of equivalent vertices yielding a prefactor of $\frac{1}{2}$. All lines are internal so the summation runs over m, n, e, and f. The two-electron integral fragment evaluates to $\langle mn||ef\rangle$, and the two T_1's become t_m^e and t_n^f. Since all lines are internal there is no chance for nonequivalent external lines, and thus no permutation operator. Putting all this together gives a complete algebraic expression for the diagram:

$$+\frac{1}{2}\sum_{\substack{mn\\ef}} \langle mn||ef\rangle\, t_m^e t_n^f \tag{2.24}$$

The doubles amplitudes diagrams (Figures 2.6 to 2.8) are interpreted in the same manner (as are all diagrams) with the following points of note. First, loops like those in the energy diagram (Figure 2.5) are obvious, but a set of lines that begin and end above the diagram is also a loop to be counted towards the sign convention. Second, none of the doubles diagrams shown have equivalent vertices as in the energy diagram, but the top two diagrams in Figure 2.8 have a pair of equivalent lines. Last, several of the shown doubles diagrams have permutations. In the case of the T_1-containing diagrams there is a single permutation, arising from the pair of nonequivalent external lines (creation or annihilation), from the T_1 and the integral. The diagrams in Figure 2.7 have nonequivalent lines arising from the

external line on the Fock operator and the corresponding creation or annihilation line on the T_2. The bottom diagram of Figure 2.8 has two pairs of nonequivalent external lines as both the creation and annihilation pairs each have one line on the T_2 and one line on the two-electron operator. Using the same procedure detailed for the energy diagram, the algebra shown in Figure 2.9 is obtained for the amplitude diagrams. For further diagram examples as well as an in depth explanation of diagram equivalency see Reference 12.

2.2.2 Lambda

Due to the non-Hermitian nature of the similarity transformed Hamiltonian, the left and right CC wavefunctions are not simple complex conjugates of one another. The right hand wavefunction (discussed above) is sufficient for computing energies of chemical systems, but when energy gradients or more complicated properties are desired the left hand wavefunction is also required. The form of the left hand wavefunction

$$\langle \Phi_{\mathrm{CC}}| = \langle R|\, e^{-T} + \sum_{\mu} \lambda_{\mu} \langle \mu|\, e^{-T}, \tag{2.25}$$

where the λ_{μ} are the lambda amplitudes and $\langle \mu|$ are substituted determinants, can be derived through the CC Lagrangian[13] and is also seen during the derivation of CC analytic energy gradients.

Multiplying on the right by e^{T} and projecting the left hand Schrödinger equation

$$\langle \Phi_{\mathrm{CC}}|\, H = \langle \Phi_{\mathrm{CC}}|\, E \tag{2.26}$$

Figure 2.9: Algebraic expressions (and associated diagrams) for those diagrams given as examples earlier.

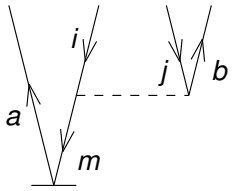

$$-P(ab)\sum_{m}\langle mb||ij\rangle\, t_m^a$$

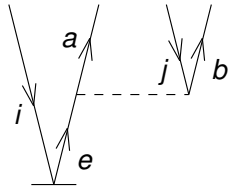

$$+P(ij)\sum_{e}\langle ab||ej\rangle\, t_i^e$$

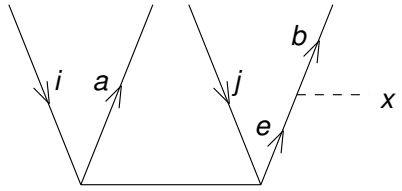

$$+P(ab)\sum_{e}F_{be}t_{ij}^{ae}$$

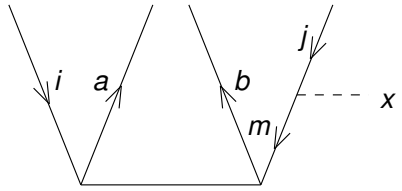

$$-P(ij)\sum_{m}F_{mj}t_{im}^{ab}$$

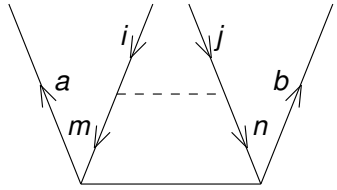

$$+\frac{1}{2}\sum_{mn}\langle mn||ij\rangle\, t_{mn}^{ab}$$

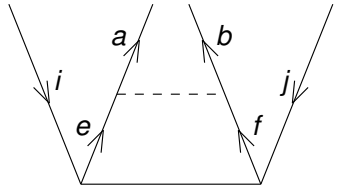

$$+\frac{1}{2}\sum_{ef}\langle ab||ef\rangle\, t_{ij}^{ef}$$

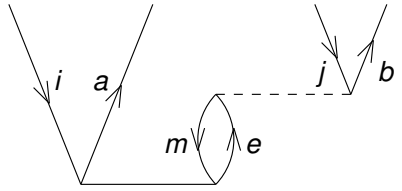

$$+P(ij)P(ab)\sum_{me}\langle mb||ej\rangle\, t_{im}^{ae}$$

by the reference gives the energy

$$\langle R|\,\overline{H}\,|R\rangle + \sum_{\mu} \lambda_{\mu}\,\langle \mu|\,\overline{H}\,|R\rangle = E, \tag{2.27}$$

which at first glance seems different than the expression shown earlier (Equation (2.9)). However, the first term on the left hand side is the same as Equation (2.9) and the second term is just lambda amplitudes multiplied by the cluster amplitude equations which once solved are zero (Equation (2.10)).

Projecting by substituted determinants

$$\langle R|\,\overline{H}\,|\nu\rangle + \sum_{\mu} \lambda_{\mu}\,\langle \mu|\,\overline{H}\,|\nu\rangle = E \sum_{\mu} \lambda_{\mu}\,\langle \mu|\nu\rangle \tag{2.28}$$

and utilizing the definition of the lambda de-excitation operator

$$\langle R|\,\Lambda_{\mu} = \lambda_{\mu}\,\langle \mu| \tag{2.29}$$

yields the lambda amplitude equations

$$0 = \langle R|\,\overline{H}\,|\nu\rangle + \langle R|\,\Lambda_{\mu}\overline{H}\,|\nu\rangle - \langle R|\,\Lambda_{\mu}\,|\nu\rangle\,E. \tag{2.30}$$

Algebraic expressions for the lambda amplitudes can be obtained using diagrams in the manner demonstrated for the cluster amplitudes. The lambda de-excitation operator (Figure 2.10) is represented as an upside-down T diagram with a thick interaction line and is also interpreted very similarly, producing lambda amplitudes whose subscript indices are unoccupied orbitals and superscripts are occupied. Two major differences exist between the lambda amplitude equations and those for the cluster amplitudes. First, the lambda operator enters the equations linearly so no terms quadratic or higher in the lambda amplitudes

Figure 2.10: Diagrammatic representation of the Λ_1 and Λ_2 operators.

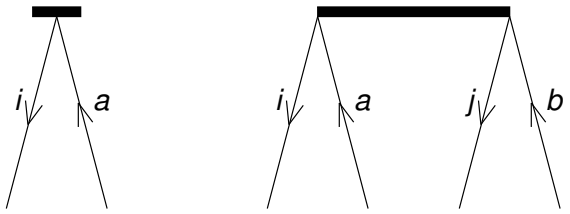

arise. Second, the only connectivity restrictions on the lambda fragment are those required to create the matrix element topology, which means that unconnected diagrams *are allowed* and do arise in the lambda equations. This foundational knowledge of CC diagrams and their interpretation will be returned to and extended in Section 4.2 when discussing the derivation and implementation of gauge invariant response properties.

Chapter 3

Basis Set Dependence

Coupled cluster optical rotation calculations exhibit significant basis set dependence with the addition of diffuse functions and higher angular momentum functions changing the rotations drastically, even changing the sign of rotation at times. Section 3.1 presents a published study on the efficacy of basis sets created for linear electric properties in the computation of CC level optical rotations. This work is extended in Section 3.2 to a basis set designed specifically with optical rotations in mind.

3.1 Basis Set Dependence of Coupled Cluster Optical Rotation Computations

3.1.1 Introduction

The past decade and a half has witnessed tremendous advances in the understanding of chiroptical phenomena and their computation.[8,15–21] Three years after the first *ab initio* calculations of optical rotation were published by Polavarapu,[22] Cheeseman et al. showed that the basis set quality is of critical importance in a study of (*S*)-methyloxirane and (*R*,*R*)-dimethylthiirane with 38 basis sets ranging in size from 48 to 596 functions at both the Hartree-Fock (HF) and density functional (DFT) levels of theory.[23] Through comparison of the Pople split-valence, Huzinaga-Dunning segmented, and Dunning correlation-consistent basis sets, they concluded that diffuse functions on all atoms are essential in these molecules and that the aug-cc-pVDZ and 6-311++G(2d,2p) basis sets are the most cost-effective.

In addition to the requirement of large basis sets, it has also been shown that high levels of electron correlation are needed for reliable reproduction of gas phase experimental results. In 2003 Ruud et al. compared the sodium D line specific rotations of 13 molecules calculated using HF, DFT, and coupled cluster methods to experiment.[24] This study was

the first systematic study of specific rotations using correlated wave function based methods. The discovery that all correlated methods outperformed HF definitively demonstrated correlation's importance. Further evidence of the impact of electron correlation on optical properties has recently come to light with the ability to study increasingly larger molecular systems. One such example is β-pinene, whose gas phase specific rotation at 633 nm is 4.66 $\pm$ 0.6 deg dm^{-1} (g/mL)$^{-1}$.[25] B3LYP yields a rotation of -20.0 deg dm^{-1} (g/mL)$^{-1}$ while the coupled cluster singles and doubles (CCSD) rotation (using the modified velocity gauge[26]) is -0.5 deg dm^{-1} (g/mL)$^{-1}$.[27] The remaining discrepancy between CCSD and experiment can be remedied by the inclusion of an inexpensive B3LYP-based vibrational correction.[28] This hybrid scheme has been applied to several molecules yielding encouraging results and, more importantly, the conclusion that a high level of electron correlation is more important than consideration of vibrational effects.

The simultaneous need for large, flexible basis sets and highly correlated methods, which have high-degree polynomial scaling, has been a significant barrier to the utilization of high accuracy methods on large molecules. There are at least two routes to surpassing this barrier: reduced scaling techniques[29] and basis set optimization.[30] Baranowska and co-workers recently reported an effort along the second route through the design of basis sets created specifically for the computation of linear electric properties.[31] These LPol basis sets were constructed by first augmenting the basis sets of van Duijneveldt[32] with diffuse functions (one *s*-type function for hydrogen and *s*- and *p*-type sets for other atoms). Spin-restricted open-shell Hartree-Fock eigenvectors from atomic calculations using this source basis set were

then used to derive first- and second-order polarization functions which were subsequently added to the source set of functions. The final LPol-fl basis set (where "f" denotes f-type angular momentum functions and "l" simply means "large") has the contraction scheme [11s6p4d/5s4p3d] for hydrogen and [14s9p6d4f/7s6p4d3f] for first-row atoms. The LPol-fl basis was then used to form LPol-fs (where "s" means "small") by reducing the number of both contracted and polarization functions. Removing the second-order polarization functions from each of the above mentioned sets results in LPol-dl and LPol-ds sets, respectively (and "d" denotes d-type angular momentum functions).

These basis sets have shown promising results when used in conjunction with DFT for the computation of optical rotation.[30] Baranowska et al. have demonstrated that these basis sets achieve results comparable to the augmented correlation consistent basis sets with fewer functions and therefore a computational savings in terms of both cpu time and storage requirements. They also presented especially encouraging specific rotations for (1S,5S)-β-pinene in which their new basis sets get the sign of the rotation correct, a first for DFT and this molecule.[30]

The purpose of this work is to test the performance of these newly minted basis sets when used in combination with coupled cluster theory, the current state of the art for optical activity modeling.[21,27] The two key aspects of performance that will be analyzed are (1) whether they provide results of comparable accuracy to the augmented correlation consistent basis sets of Dunning and co-workers and (2) whether such results can be obtained at significant computational savings. In order to ensure that our analysis is applicable to

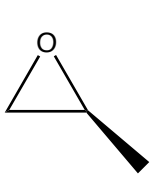

(*S*)-methyloxirane

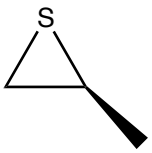

(*S*)-methylthiirane

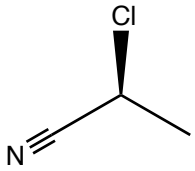

(*S*)-chloropropionitrile

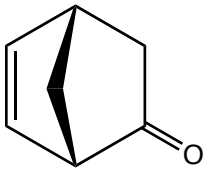

(1*S*,4*S*)-norbornenone

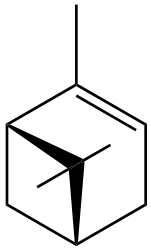

(1*R*,5*R*)-β-pinene

a wide variety of molecular structures and bonding motifs, we have chosen five molecules whose specific rotations are notoriously difficult to compute, including those listed above and two others, (*S*)-methyloxirane,[33,34] (*S*)-methythiirane,[35] (*S*)-2-chloropropionitrile,[36] (1*S*,4*S*)-norbornenone, and (1*R*,5*R*)-β-pinene.[27]

3.1.2 Computational Details

The specific rotations reported here were computed using the Rosenfeld optical activity tensor,[5,6]

$$\mathbf{G}'(\omega) = -\frac{2\omega}{\hbar} \sum_{j \neq 0} \frac{\mathrm{Im}(\langle \psi_0 | \boldsymbol{\mu} | \psi_j \rangle \langle \psi_j | \mathbf{m} | \psi_0 \rangle)}{\omega_{j0}^2 - \omega^2} \tag{3.1}$$

where ω is the frequency of plane-polarized light, $\boldsymbol{\mu}$ and $\mathbf{m}$ are the electric- and magnetic-dipole operators, respectively, and the summation runs over the excited electronic (unperturbed) wave functions, ψ_j, each associated with an excitation frequency, ω_{j0}. The specific

rotation is related to the trace of this tensor. The explicit summation over all electronically excited states in Equation (3.1) is avoided in practice through the use of the formally equivalent and more efficient linear response approach.[37,38] This technique is utilized in many quantum chemistry program suites including those used in this work: PSI3[39] and a January 2010 version of DALTON.[40]

Specific rotations were computed at four wavelengths, 355, 436, 589, and 633 nm, using time-dependent density functional theory (TD-DFT) with the B3LYP[41,42] functional in DALTON as well as the CC2[43] and CCSD[44,45] methods in PSI3. Origin-independent results were obtained for all three methods. For DFT, gauge-including atomic orbitals (GIAOs)[46,47] were employed, while the CC methods made use of the modified dipole-velocity gauge (MVG).[26] In all CC calculations the core orbitals ($1s$ for C, N, and O, and $1s2s2p$ for S and Cl) were held frozen. The molecular geometries of the five molecules studied were taken to be the optimized structures previously reported.[27,30,33,35,36]

Two different types of basis sets were examined in this work: the double- and triple-ζ versions of Dunning's correlation-consistent basis sets augmented with one and two sets of diffuse functions[48–50] as well as the large polarized (LPol) basis sets of Sadlej.[31] For simplicity the Dunning basis sets, n-aug-cc-pVXZ, will be abbreviated throughout this paper as naXZ, *e.g.* d-aug-cc-pVDZ will be referred to as daDZ. The data gathered using the Dunning basis sets are used as reference data to evaluate the performance of the Sadlej basis sets. In the cases of (*S*)-methylthiirane and (*S*)-2-chloropropionitrile the LPol and doubly augmented Dunning bases are not defined for the sulfur and chlorine atoms, so aDZ and aug-cc-pV(D+d)Z were

used on these atoms for all such computations. As both exhibited similar convergence trends, only the aDZ results are presented below.

3.1.3 Results and Discussion

(*S*)-methyloxirane has been extensively studied both experimentally and computationally. The experimental interest in methyloxirane began with the discovery that its specific rotation is extremely solvent dependent, exhibiting a different sign in water than in all other measured solvents.[51] The availability of experimental rotations in a variety of solvents as well as its small size made methyloxirane a natural choice for theoretical studies, and it was included in the first computational study of optical rotation by Polavarapu.[22] These initial results were expanded upon by Cheeseman et al. to include a much larger sampling of basis sets as well as the DFT level of theory.[23] Specific rotations have also been calculated using more highly correlated methods including CCSD[33] and the inclusion of approximate triples with the CC3 method.[52] Although high levels of electron correlation do not completely close the gap between the experimental gas phase[25,53] and computed specific rotations, vibrational corrections do appear to resolve the discrepancies. It was first shown by Ruud and Zanasi that the addition of a simple B3LYP vibrational correction to CCSD specific rotations brought the sign of the CCSD rotations into agreement with experiment.[34] Kongsted et al. later showed that improving the vibrational correction to the CCSD level not only alleviated the sign problem but also brought the computed values within three deg dm^{-1} $(g/mL)^{-1}$ of experiment.[52]

Table 3.1: Specific rotations (deg dm^{-1} (g/mL)$^{-1}$) for (*S*)-methyloxirane[1]

Basis set (# fxns)	aDZ (146)	daDZ (206)	aTZ (322)	daTZ (440)	LPol-ds (222)	LPol-dl (282)	LPol-fs (338)	LPol-fl (456)
λ (nm)	B3LYP							
355	12.1	23.7	30.7	34.4	34.1	35.6	35.3	35.2
436	−14.1	−6.6	−0.8	1.2	0.6	1.6	1.6	1.8
589	−14.7	−10.7	−7.3	−6.3	−6.7	−6.2	−6.2	−6.0
633	−13.5	−10.1	−7.1	−6.2	−6.6	−6.2	−6.1	−6.0
	CC2[2]							
355	−74.6	−34.6	−52.0	−39.9	−34.6	−36.5	−36.9	−37.6
436	−71.6	−46.5	−52.7	−45.3	−44.7	−45.6	−44.7	−44.6
589	−45.6	−32.4	−34.2	−30.4	−30.9	−31.3	−30.5	−30.3
633	−40.1	−28.8	−30.2	−27.0	−27.4	−27.8	−27.0	−26.9
	CCSD[2]							
355	−56.4	−26.7	−28.3	−20.0	−21.7	−22.4	−20.2	−19.8
436	−48.4	−29.5	−28.6	−23.5	−25.4	−25.8	−24.0	−23.6
589	−30.1	−20.1	−19.0	−16.3	−17.6	−17.8	−16.7	−16.5
633	−26.5	−17.8	−16.8	−14.5	−15.7	−15.8	−14.9	−14.7

[1] Gas-phase experimental rotations from Ref. 25, (355 nm) 7.5 ± 0.3, (633 nm) -8.4 ± 0.2

[2] Modified dipole-velocity gauge.

Despite the established need for large basis sets, high levels of electron correlation, and vibrational corrections, we have choosen to test the LPol basis sets on methyloxirane due to its historical prominence in the literature as well as the feasibility of using very large basis sets. This is reasonable because our main purpose in this study is comparison between basis sets, although comparison with experiment is also important, and thus we have included experimental data where available. Table 3.1 reports the computed specific rotations of (*S*)-methyloxirane at the three levels of theory and four wavelengths outlined previously. The dispersion curve of (*S*)-methyloxirane has been shown previously to be most sensitive at 355 nm,[33] and we focus our discussion there accordingly. All three methods show smooth convergence to clear basis set limits of approximately 35, -38, and -20 deg dm^{-1} $(g/mL)^{-1}$ at 355 nm for B3LYP, CC2, and CCSD, respectively. For B3LYP at 355 nm, LPol-ds yields 34.1 deg dm^{-1} $(g/mL)^{-1}$ with 222 functions while the comparable Dunning basis result, requiring 440 functions, is 34.4 deg dm^{-1} $(g/mL)^{-1}$ with daTZ. The CCSD results with the Dunning basis sets are similar to those obtained by Tam et al.,[33] and diffuse functions are required as reported by Cheeseman et al.,[23] but in this case at least two sets, daDZ, are required to approach the basis set limit. Increasing the quality of the basis to the triple-ζ level does not result in specific rotation magnitudes appreciably different from those of the doubly augmented double-ζ. When two sets of diffuse functions (daTZ) are used, the results change by approximately 25% from -26.7 to -20.0 deg dm^{-1} $(g/mL)^{-1}$; however, this change comes at the price of a substantial increase in number of basis functions, from 206 to 440. This doubling of the basis size would be reasonable if the results approached the gas phase

value of 7.5 ± 0.3 deg dm^{-1} $(g/mL)^{-1}$ put forth by Wilson et al., but this is not the case.[25] The basis set limit is reached in CCSD by the daTZ Dunning basis returning -20.0 deg dm^{-1} $(g/mL)^{-1}$, while LPol-fs achieves nearly the same result, -20.2 deg dm^{-1} $(g/mL)^{-1}$, with 102 fewer functions. The performance of the much smaller LPol-ds is only slightly worse, achieving a final rotation of -21.7 deg dm^{-1} $(g/mL)^{-1}$. The CC2 specific rotations exhibit trends in response to basis set size similar to those of CCSD, only differing in magnitude throughout the dispersion curve due to the reduced level of electron correlation. Regardless of the level of theory utilized and whether or not the computed specific rotations approach the experimental value, those computed with the Sadlej basis sets approach the basis set limit faster, requiring fewer functions to adequately describe the one-electron space.

(*S*)-methylthiirane is structurally very similar to (*S*)-methyloxirane and thus enables one to probe a valuable question: are the difficulties encountered in reproducing gas phase experimental results for methyloxirane universal problems to be faced for the majority of molecules? (*S*)-methylthiirane's dispersion curve is simpler than methyloxirane's as it is not bisignate, viz. it remains negative throughout the wavelength range. Crawford et al. concluded, based on their systematic study of methylthiirane's excited states, vibrational frequencies, and specific rotations using both B3LYP and CCSD, that methylthiirane faces difficulties similar to those faced by methyloxirane.[35]

Table 3.2: Specific rotations (deg dm^{-1} $(g/mL)^{-1}$) for (*S*)-methylthiirane[1]

Basis set (# fxns)	aDZ (150)	daDZ* (201)	aTZ (326)	daTZ* (428)	LPol-ds* (213)	LPol-dl* (264)	LPol-fs* (315)	LPol-fl* (417)
λ (nm)	B3LYP							
355	52.1	151.4	140.0	161.4	161.7	161.8	150.1	145.6
436	−66.5	−6.8	−14.3	−3.2	−0.5	0.3	−5.4	−7.6
589	−55.8	−26.0	−29.4	−24.5	−22.8	−22.2	−24.8	−25.8
633	−49.8	−24.5	−27.3	−23.2	−21.7	−21.2	−23.4	−24.2
	CC2[2]							
355	−114.1	−15.8	−56.2	−34.9	−26.7	−30.5	−34.4	−36.9
436	−114.4	−52.5	−72.3	−59.9	−58.2	−60.6	−62.0	−63.3
589	−69.8	−37.8	−46.4	−40.3	−40.3	−41.6	−42.1	−42.6
633	−60.9	−33.5	−40.7	−35.5	−35.6	−36.7	−37.1	−37.6
	CCSD[2]							
355	−146.0	−55.2	−96.2	−78.0	−65.9	−72.5	−77.7	−79.6
436	−121.8	−65.1	−85.9	−75.0	−70.1	−74.0	−76.3	−77.3
589	−70.7	−41.5	−50.8	−45.4	−43.6	−45.5	−46.5	−47.0
633	−61.4	−36.4	−44.2	−39.6	−38.1	−39.8	−40.6	−41.0

[1] Gas-phase experimental rotations from Ref. 25, (355 nm) -64.7 ± 2.3, (633 nm) -36.5 ± 1.7

* aDZ basis on sulfur atom.

[2] Modified dipole-velocity gauge.

Table 3.2 reports the relevant optical rotation data for (*S*)-methylthiirane. Again for simplicity the discussion of the results will be centered on the specific rotations at 355 nm as this is the wavelength that shows the most variation among basis sets and methods. As stated earlier, the LPol, daDZ, and daTZ bases are not defined for the sulfur atom, so the aDZ basis set was used in all cases. The basis set limits for B3LYP, CC2, and CCSD are approximately 160, -35, and -78 deg dm^{-1} $(g/mL)^{-1}$, respectively. The difference between the two largest Dunning basis sets, aTZ and daTZ, is at least 18 deg dm^{-1} $(g/mL)^{-1}$ for all three methods, while the difference between LPol-fs and LPol-fl, the two largest Sadlej bases, is no greater than 2.5 deg dm^{-1} $(g/mL)^{-1}$. The agreement between the largest Dunning and LPol basis sets lend confidence to our CC2 and CCSD basis set limit approximations. This is not the case for the B3LYP limit, where the difference between the Dunning and Sadlej basis sets is over six times larger at 15.8 deg dm^{-1} $(g/mL)^{-1}$. For B3LYP the comparison of the performance of LPol to that of the Dunning bases is complicated by the uncertainty of the true basis set limit. Both the LPol-ds and -dl sets achieve specific rotations that are within 0.4 deg dm^{-1} $(g/mL)^{-1}$ of the daTZ result of 161.4 deg dm^{-1} $(g/mL)^{-1}$. This seems to suggest that LPol-ds is performing comparably to daTZ and has reached the basis set limit. However, the LPol-fs result drops below the daTZ value by 11.3 deg dm^{-1} $(g/mL)^{-1}$ but is very similar to the LPol-fl value, casting doubt on the performance of the LPol-ds basis. The situation is clearer in the case of the CC methods for which the LPol-fs basis set is near the basis set limit, performing as well as daTZ for both CC2 and CCSD. The LPol-fs rotations are also substantially closer to the basis set limit at 355 nm than those of the larger

aTZ basis. While for CC2 and CCSD the LPol-ds results are not as encouraging as those of methyloxirane, they are closer to the basis set limit than the comparably sized daDZ of Dunning for both methods. Despite not being able to state definitively the cost effectiveness of the Sadlej basis sets based on basis set limit for all three methods, we do notice that the Sadlej basis sets appear to reach the basis set limit more quickly than the Dunning sets, smoothly converging from LPol-ds to LPol-fl, while the Dunning sets take large oscillatory steps towards the limit.

Table 3.3: Specific rotations (deg dm^{-1} (g/mL)$^{-1}$) for (*S*)-2-chloropropionitrile[1]

Basis set (# fxns)	aDZ (155)	daDZ* (207)	aTZ (326)	daTZ* (426)	LPol-ds* (223)	LPol-dl* (275)	LPol-fs* (319)	LPol-fl* (419)
λ (nm)				B3LYP				
355	−62.0	−72.1	−74.1	−71.4	−75.7	−78.4	−77.2	−78.4
436	−33.4	−42.3	−40.7	−39.4	−41.4	−43.4	−42.6	−43.4
589	−15.5	−18.5	−19.2	−18.2	−19.4	−20.5	−20.2	−20.5
633	−13.1	−15.6	−16.3	−15.4	−16.4	−17.4	−17.7	−17.4
				CC2[2]				
355	−36.8	−47.4	−45.0	−46.7	−46.5	−45.2	−46.6	−45.4
436	−20.8	−27.6	−25.9	−27.0	−27.0	−26.3	−27.1	−27.3
589	−10.0	−13.5	−12.6	−13.2	−13.2	−12.9	−13.3	−13.4
633	−8.5	−11.5	−10.7	−11.2	−11.3	−11.0	−11.3	−11.4
				CCSD[2]				
355	−25.8	−35.3	−34.0	−35.5	−34.6	−33.5	−34.5	−33.5
436	−14.4	−20.4	−19.5	−20.4	−20.0	−19.4	−20.0	−19.3
589	−6.8	−10.0	−9.5	−9.9	−9.8	−9.5	−10.1	−9.4
633	−5.8	−8.5	−8.0	−8.5	−8.3	−8.1	−8.6	−8.0

[1] Gas-phase experimental rotations from Ref. 25, (355 nm) -37.9 ± 2.9, (633 nm) -6.8 ± 2.3

* aDZ basis on chlorine atom.

[2] Modified dipole-velocity gauge.

The results for (*S*)-2-chloropropionitrile, shown in Table 3.3, show very little basis set dependence, regardless of method or wavelength. The basis set limits for CC2 and CCSD are -46 and -35 with great agreement between the Dunning and LPol basis sets. As was the case with methylthiirane, the differences between LPol and Dunning sets are larger for B3LYP than for the CC methods. Within the B3LYP LPol results LPol-dl obtains the same rotation as LPol-fl, namely -78.4 deg dm^{-1} $(g/mL)^{-1}$. Reducing the size even further, LPol-ds increases the rotation by 2.7 to -75.7 deg dm^{-1} $(g/mL)^{-1}$. The LPol results are very internally consistent, but the largest set, LPol-fl, differs from Dunning's daTZ by 7.0 deg dm^{-1} $(g/mL)^{-1}$. The LPol sets seem to have reached the basis set limit by LPol-dl and are no longer changing with additional functions. The CC2 results show similar behavior reaching the basis set limit early: LPol-ds differs from daTZ by only 0.2 deg dm^{-1} $(g/mL)^{-1}$. For CCSD the Dunning basis sets reach the basis set limit by daDZ and the LPol results are all within 1.1 deg dm^{-1} $(g/mL)^{-1}$ of each other, having reached the basis set limit by LPol-ds. For all three methods the basis set limit has essentially been reached by daDZ. Thus the chloropropionitrile data do not provide much insight into our comparison of the LPol bases with those of Dunning because the basis set limit is reached with such a small basis.

(1*S*,4*S*)-norbornenone is a molecule of intense interest due to its confounding properties. In 2001 an analysis[54] of 30 molecules demonstrated that for 28 of them the mean absolute deviation between experiment and aDZ calculated rotations for B3LYP is 20.1 deg dm^{-1} $(g/mL)^{-1}$ and HF is 35.5 deg dm^{-1} $(g/mL)^{-1}$; norbornenone was one of the two molecules whose results were analyzed separately. The difference between the 589 nm B3LYP value of

-1215.8 and the experimental value of -1146 deg dm^{-1} $(g/mL)^{-1}$ for norbornenone is 69.8 deg dm^{-1} $(g/mL)^{-1}$. While this difference is nearly 3.5 times larger than the mean absolute deviation for the other molecules, in relative terms it is only a mere six% difference. The interesting difference is between the HF computed rotation of -606.7 deg dm^{-1} $(g/mL)^{-1}$ and those already mentioned.[54] These results seemed to indicate the extreme importance of electron correlation in this system. A study by Ruud et al. two years later muddied the waters further when they showed that the aDZ specific rotation for norbornenone computed with CCSD is -740.6 and with CC2 it is -1000.0 (both using the origin-dependent length-gauge representation).[24] B3LYP and CC2 are in the same ballpark and closest to experiment, while CCSD and HF are together, but neither can see the game. Vibrational effects were considered by Mort and Autschbach,[55] who found that at the B3LYP level, zero-point corrections made no appreciable difference. The influence of basis set on the rotations has been tested by Crawford and Stephens, but without conclusion.[27] One possible reason for the discrepancy between CCSD and experiment is that the only published experimental value was measured in the solution phase, although solvent effects are not expected to be large in this case based on data from measurements in a variety of solvents.[56–58]

Table 3.4: Specific rotations (deg dm^{-1} (g/mL)$^{-1}$) for (1*S*,4*S*)-norbornenone[1]

Basis set (# fxns)	aDZ (256)	daDZ (360)	aTZ (552)	daTZ (752)	LPol-ds (392)	LPol-dl (496)	LPol-fs (584)	LPol-fl (784)
λ (nm)				B3LYP				
355	−12 573.9	−12 319.2	−11 815.9	−11 837.1	−11 931.3	−11 958.9	–	–
436	−3650.7	−3564.0	−3484.6	−3489.0	−3507.1	−3506.7	−3494.3	−3492.0
589	−1250.9	−1218.9	−1198.1	−1199.5	−1205.0	−1203.7	−1200.6	−1199.8
633	−1015.6	−989.3	−972.9	−974.1	−978.5	−977.3	−974.9	−974.2
				CC2[2]				
355	−6194.8	−6257.7	−6347.4	–	−6371.6	−6434.9	–	–
436	−2199.1	−2211.8	−2248.0	–	−2250.1	−2265.1	–	–
589	−814.3	−817.1	–	–	−831.3	–	–	–
633	−667.1	−669.2	–	–	−680.8	–	–	–
				CCSD[2]				
355	−3896.0	−3923.0	−3818.8	–	−3902.3	–	–	–
436	−1462.4	−1467.2	–	–	−1466.3	–	–	–
589	−559.9	−560.5	–	−556.4	−561.5	–	–	–
633	−460.8	−461.2	–	–	−462.2	–	–	–

[1] Hexane solution experimental rotations from Ref. 58, (589 nm) -1146.0

[2] Modified dipole-velocity gauge.

Our results for (1*S*,4*S*)-norbornenone are shown in Table 3.4. The B3LYP specific rotations exhibit systematic convergence to the basis set limit of approximately -1200 deg dm^{-1} (g/mL)$^{-1}$ at 589 nm. This limit is reached with aTZ and LPol-fs bases. However, the large magnitude of the specific rotation makes it unnecessary to go past the -1250.9 deg dm^{-1} (g/mL)$^{-1}$ of the aDZ basis as it represents only a 4% difference from the basis set limit. Due to the size of norbornenone only a few basis sets are currently accessible at the CCSD level, for which the basis set limit appears to be around -556 deg dm^{-1} (g/mL)$^{-1}$. LPol-ds performs comparably to aDZ and daDZ, the two Dunning bases fully tested, differing from both by less than 0.3 %. Norbornenone's large specific rotations have very little basis set dependence at the CCSD level, as seen by the two rotations computed with even larger basis sets. The small percent differences and the cost of those two points, roughly four months for the daTZ rotation, make completing the columns frivolous. The LPol-dl basis set was tested at the CC2 level yielding results comparable to aTZ and LPol-ds. The LPol-dl basis set can be assumed to exhibit similar behavior at the CCSD level as the trends in the earlier test cases suggest. From these more complete basis sets the CC2 limit appears to be -825 deg dm^{-1} (g/mL)$^{-1}$, although CC2 changes slightly more than CCSD does with increasing basis size. The evidence from CC2 lends further confidence to the statement that basis sets larger than aDZ are not required at the CCSD level for norbornenone. One other feature of note is the large difference in magnitude of the B3LYP rotations at 355 nm compared to those of CCSD. The specific rotations for both methods are in the same direction, but the B3LYP rotations are nearly twice as large for all tested basis sets. This is possibly due to

the close proximity of a resonance at 307 nm (aDZ), which is distorting the results.

Table 3.5: Specific rotations (deg dm^{-1} (g/mL)$^{-1}$) for (1*R*,5*R*)-β-pinene[1]

Basis set (# fxns)	aDZ (374)	daDZ (528)	aTZ (828)	daTZ (1132)	LPol-ds (568)	LPol-dl (722)	LPol-fs (868)
λ (nm)				B3LYP			
355	−264.9	−261.0	−252.5	−252.6	−250.4	−250.3	−253.7
436	−94.3	−91.9	−87.7	−87.8	−87.2	−86.8	−88.5
589	−27.3	−26.1	−24.3	−24.3	−24.2	−23.9	−24.7
633	−21.0	−20.0	−18.4	−18.5	−18.4	−18.1	−18.8
				CC2[2]			
355	−202.9	−203.7	–	–	−187.8	–	–
436	−79.1	−80.2	–	–	−73.5	–	–
589	−25.5	−26.2	–	–	−23.4	–	–
633	−20.0	−20.3	–	–	−18.4	–	–
				CCSD[2]			
355	−84.7	−85.9	–	–	−74.1	–	–
436	−21.7	–	–	–	–	–	–
589	−0.7	–	–	–	–	–	–
633	0.7	0.4	–	–	2.0	–	–

[1] Gas-phase experimental rotations from Ref. 25, (355 nm) -69.7 ± 3.2, (633 nm) 4.7 ± 0.6

[2] Modified dipole-velocity gauge.

In the 2010 report by Baranowska et al. the LPol bases were shown to perform significantly better than the correlation consistent bases of Dunning for β-pinene, even providing the correct sign for the rotation when compared to the gas phase experimental value.[30,59,60] However, we are unable to reproduce the reported result with any of the LPol bases. Rather we find that they perform similarly to the Dunning bases as seen in the results shown in Table 3.5. B3LYP obtains the correct sign at 355 nm, but the incorrect sign at 633 nm for all tested basis sets. Despite having the correct sign at 355 nm the magnitudes of all 355 nm results are off by a factor of approximately 3.5. The increase from 374 to 528 basis functions when moving from aDZ to daDZ is not warranted by the small change in computed rotation of 3.9 deg dm^{-1} (g/mL)$^{-1}$. The LPol-ds result of -250.4 deg dm^{-1} (g/mL)$^{-1}$ is closer to the basis set limit than the comparably sized daDZ rotation of -261.0 deg dm^{-1} (g/mL)$^{-1}$ at a reasonable size increase of 40 functions. However, the most cost-effective basis for B3LYP is aDZ and in the case of (1*R*,5*R*)-β-pinene the LPol basis sets are unnecessary. The smallest computed basis set for CCSD, aDZ, has the correct sign at both 355 and 633 nm as well as magnitudes that are nearly within the experimental error bars. The difference between the aDZ and daDZ bases once again does not warrant the use of the larger basis. However, the LPol-ds basis improves upon the daDZ result significantly enough to justify its use. The 355 nm specific rotation of -74.1 falls outside the experimental range by just 1.2 deg dm^{-1} (g/mL)$^{-1}$, and the 633 nm result becomes more positive, moving closer to the experimental value compared to aDZ. Unfortunately, the Dunning basis of comparable accuracy remains unknown as the aTZ basis is currently too large for CC-level optical rotation computations.

3.1.4 Conclusions

The goal of this work was to determine the efficacy of the newly developed LPol basis sets for use in coupled cluster optical rotation computations. We have compared the specific rotations of five notoriously difficult cases, (*S*)-methyloxirane, (*S*)-methythiirane, (*S*)-2-chloropropionitrile, (1*S*,4*S*)-norbornenone, and (1*R*,5*R*)-β-pinene, using these new basis sets to those obtained with the standard correlation-consistent basis sets. The computed rotations for these five test molecules demonstrate that the LPol basis sets from the Sadlej group perform well for computing specific rotations, and that the smallest one, LPol-ds, performs as well as the other three larger LPol sets. Our results exhibit diminishing returns gained from increasing from the LPol-ds to the -dl variant. The difference between the computed specific rotations is negligible, and this is also the case between the LPol-fs and -fl versions. The difference between LPol-ds and -fs is often more substantial, but still not great enough to justify the large increase in number of functions. The most cost effective Sadlej basis, LPol-ds, yields equivalent, if not better, results as the comparably sized daDZ basis.

The convergence behavior of the two sets is at times substantially different, with the correlation-consistent sets showing oscillatory behavior around the basis set limit while the LPol sets typically exhibit a clear convergence trend. When the LPol sets do oscillate, the variations are small, with all results being near the basis set limit. One foreseeable problem, albeit perhaps a computationally impractical one, is that the correlation-consistent basis sets are more extensible than those of Sadlej allowing for further extension in the search for the basis set limit. The LPol basis sets are an efficient choice, although they do not overwhelmingly

surpass the abilities of the correlation-consistent sets. Of course, the utility of these new basis sets does not alleviate the need for higher levels of electron correlation, vibrational corrections, and the inclusion of solvent effects, etc. in order to achieve reliable comparison to experiment.

3.2 The ORP Basis: Coupled Cluster Performance

3.2.1 Introduction

Motivated by the success of their LPol bases in optical rotation calculations for both DFT[30] and CC[14] levels of theory one of the LPol creators, Baranowska, has recently created the optical rotation prediction (ORP) basis, specifically for use in optical rotation calculations.[61] The goals of development were two-fold: (1) reduce the size compared to the LPol sets which are too large for regular use and (2) reduce the linear dependencies found in the LPol bases while retaining the quality of optical rotation calculations computed using the LPol basis sets. To accomplish these goals, the ORP basis was constructed using a process similar to that of the LPol sets, starting in this case from the uncontracted VTZ basis of Ahlrichs and co-workers.[62] To ensure an adequate treatment of regions far from the nucleus, the basis was expanded in an even-tempered manner to include diffuse functions (one s-type for hydrogen and one s- and p-type for all other atoms) based on the two lowest original exponents. In addition, three uncontracted first-order polarization functions were added whose exponent values were optimized by minimizing the error in ROHF atomic polarizabilities relative to the reference data of Stiehler and Hinze and the exact value of 4.5 a.u. for hydrogen.[63] Contracting this basis (except the polarization functions) yielded a slightly smaller and less linearly dependent basis than LPol-ds, the smallest of the LPol sets, of the form $[6s3p/4s3p]$ for hydrogen and $[11s7p3d/5s4p3d]$ for all other atoms.

Results for a test suite of 32 molecules are promising, showing that B3LYP rotations com-

puted using the ORP basis are very close to the quality of those computed using the daTZ basis. Since the LPol basis sets yield comparable quality results across methods we have endeavored, in collaboration with Baranowska, to test the quality of CC level optical rotations computed with the ORP basis.

3.2.2 Computational Details

Initially we have chosen four molecules to test CC level optical rotations computed with the ORP basis, (*S*)-methyloxirane, (*R*)-fluorooxirane, (1*S*,4*S*)-norbornenone, (1*R*,5*R*)-β-pinene. The same series of basis sets as presented in the LPol basis testing (Section 3.1), that is the Dunning and LPol series, are compared to analyze the performance of the ORP basis. We will continue the abbreviation scheme used above for basis names. For (*S*)-methyloxirane, (1*S*,4*S*)-norbornenone, and (1*R*,5*R*)-β-pinene we have used the molecular geometries from Reference 14 and for (*R*)-fluorooxirane we have used the geometry from Reference 61. Specific rotations were computed using PSI4 at four wavelengths, 355, 436, 589, and 633 nm. As the success of the ORP basis for density functional level calculations has been previously demonstrated our work is restricted to coupled cluster levels of theory including the CC2[43] and CCSD[44,45] methods. The modified dipole-velocity gauge (MVG)[26] was used in all cases to ensure origin-independent results and core orbitals (1*s* for C, N, O, and F) were held frozen.

3.2.3 Results and Discussion

As mentioned in Section 3.1.3 the small size of (*S*)-methyloxirane enables the use of large basis sets improving our ability to determine the basis set limit. In Table 3.6 optical rotations for the ORP basis are shown alongside rotations for Dunning and LPol basis sets (reproduced from Reference 14 for ease of analysis). For the CC2 method the ORP basis performs slightly better than the daDZ basis (which coincidentally has the same number of functions), yielding a 355 nm specific rotation of -35.7 deg dm^{-1} $(g/mL)^{-1}$. This rotation falls between the rotations produced by the LPol-ds and LPol-dl sets of -34.6 deg dm^{-1} $(g/mL)^{-1}$ and -36.5 degrees respectively. In both cases ORP is closer to the basis set limit than the comparably sized Dunning and LPol bases. While the improvement is minor it comes at no increase in cost, and in the case of LPol-ds at a savings of 16 functions. The CCSD performance is not as uniform, focusing again on the 355 nm results the ORP rotation of -24.2 deg dm^{-1} $(g/mL)^{-1}$ falls between the aTZ and daTZ results. However, in comparison to the LPol results, the ORP results are not as promising. For all four wavelengths the rotations are further from the basis set limit than those of the smallest LPol set, LPol-ds.

Table 3.6: Specific rotations (deg dm^{-1} $(g/mL)^{-1}$) for (*S*)-methyloxirane[1]. All data except that for the ORP basis is reproduced from Mach and Crawford.[14]

Basis set (# fxns)	aDZ (146)	daDZ (206)	aTZ (322)	daTZ (440)	LPol-ds (222)	LPol-dl (282)	LPol-fs (338)	LPol-fl (456)	ORP (206)
λ (nm)					CC2[2]				
355	−74.6	−34.6	−52.0	−39.9	−34.6	−36.5	−36.9	−37.6	−35.7
436	−71.6	−46.5	−52.7	−45.3	−44.7	−45.6	−44.7	−44.6	−45.8
589	−45.6	−32.4	−34.2	−30.4	−30.9	−31.3	−30.5	−30.3	−31.6
633	−40.1	−28.8	−30.2	−27.0	−27.4	−27.8	−27.0	−26.9	−28.0
					CCSD[2]				
355	−56.4	−26.7	−28.3	−20.0	−21.7	−22.4	−20.2	−19.8	−24.2
436	−48.4	−29.5	−28.6	−23.5	−25.4	−25.8	−24.0	−23.6	−27.1
589	−30.1	−20.1	−19.0	−16.3	−17.6	−17.8	−16.7	−16.5	−18.5
633	−26.5	−17.8	−16.8	−14.5	−15.7	−15.8	−14.9	−14.7	−16.5

[1] Gas-phase experimental rotations from Ref. 25, (355 nm) 7.5 ± 0.3, (633 nm) -8.4 ± 0.2

[2] Modified dipole-velocity gauge.

(*R*)-fluorooxirane is another small molecule for which it is possible to use large basis sets at the CC level of theory. Table 3.7 reports specific rotations for (*R*)-fluorooxirane at the CC2 and CCSD levels of theory as well B3LYP results of Baranowska[61] as we have yet to investigate this system in this document. The B3LYP results show ORP performing nearly as well as daTZ with ORP rotations differing by at most 1.0 deg dm^{-1} (g/mL)$^{-1}$ across the range of wavelengths shown. The LPol sets all perform comparably, with the largest, LPol-fl, producing rotations very similar to those of daTZ and thus ORP is performing nearly as well as LPol-fl. In both cases this performance comes at a savings of nearly 200 functions, meaning ORP produces daTZ/LPol-fl quality rotations using less than half the functions. The CC results show stronger basis set dependence and are thus less easily interpreted. In the CC2 case the Dunning series begins at aDZ with positive rotations for all four wavelengths and ends with a bisignate dispersion curve at the daTZ basis. The ORP basis captures this bisignate character and changes sign between 436 and 589 nm in agreement with the daTZ data. The magnitude of the ORP rotations differ significantly from those of daTZ though with the largest difference at 355 nm being greater than 50%. In addition, the LPol-ds and -dl rotations agree more closely with the daTZ rotations, differing by at most 2.0 deg dm^{-1} (g/mL)$^{-1}$, than the ORP rotations. The oscillations in the Dunning rotations leave room for the basis set limit to be slightly lower than the -9.9 deg dm^{-1} (g/mL)$^{-1}$ rotation of daTZ, but it is unlikely that going to daQZ will lower the rotation by 5.6 deg dm^{-1} (g/mL)$^{-1}$ to the ORP rotation of -15.5 deg dm^{-1} (g/mL)$^{-1}$.

Table 3.7: Specific rotations (deg dm^{-1} (g/mL)$^{-1}$) for (*R*)-fluorooxirane. All CC2 and CCSD results except those for the ORP basis are reproduced from Mach and Crawford.[14]

Basis set (# fxns)	aDZ (119)	daDZ (167)	aTZ (253)	daTZ (344)	LPol-ds (183)	LPol-dl (231)	LPol-fs (269)	LPol-fl (360)	ORP (167)
λ (nm)					B3LYP[1]				
355	−30.8	−50.3	−56.9	−61.0	−61.4	−58.6	−62.4	−60.6	−60.0
436	–	–	–	–	–	–	–	–	–
589	−4.9	−11.4	−13.6	−15.0	−15.2	−14.3	−15.6	−14.9	−14.8
633	−4.0	−9.6	−11.5	−12.6	−12.8	−12.1	−13.1	−12.6	−12.5
					CC2[2]				
355	12.1	−8.5	−2.5	−9.9	−9.7	−7.9	–	–	−15.5
436	14.6	0.8	3.9	−1.2	−1.1	0.6	–	–	−3.5
589	10.3	2.8	4.1	1.3	1.3	2.4	–	–	0.5
633	9.2	2.7	3.8	1.4	1.4	2.3	–	–	0.7
					CCSD[2]				
355	18.9	−1.3	−0.5	−8.3	−9.6	−5.1	–	–	−7.4
436	15.8	2.5	2.8	−2.3	−3.2	−0.1	–	–	−1.4
589	9.9	2.7	2.8	0.0	−0.5	1.2	–	–	0.7
633	8.7	2.5	2.6	0.2	−0.3	1.2	–	–	0.7

[1] Results of Baranowska-Łaczkowska and Łaczkowski[61] computed with DALTON.

[2] Modified dipole-velocity gauge.

In opposition to those of (*S*)-methyloxirane, the (*R*)-fluorooxirane rotations computed with the ORP basis at the CCSD level are of higher quality than comparably sized Dunning and LPol basis sets. As at the CC2 level, the ORP basis captures the correct bisignate nature of the dispersion curve changing sign between 436 and 589 nm. The rotations are between those of aTZ and daTZ, for instance at 589 nm the ORP rotation of 0.7 deg dm^{-1} $(g/mL)^{-1}$ falls between the 2.8 deg dm^{-1} $(g/mL)^{-1}$ of aTZ and the -0.0 deg dm^{-1} $(g/mL)^{-1}$ (where the sign is negative only to indicate that before rounding the rotation produced was negative) of daTZ. This high performance is comparable to that seen at the B3LYP level for this molecule. In terms of the LPol basis sets, the performance of the ORP basis falls between LPol-ds and -dl for CCSD. These basis sets are closer to the basis set limit than the comparably sized Dunning basis sets, so while this comparison seems less impressive, the ORP basis is still performing quite well.

Table 3.8: Specific rotations (deg dm^{-1} (g/mL)$^{-1}$) for (1*S*,4*S*)-norbornenone[1]. All rotations except those for the ORP basis reproduced from Mach and Crawford.[14]

Basis set (# fxns)	aDZ (256)	daDZ (360)	aTZ (552)	daTZ (752)	LPol-ds (392)	LPol-dl (496)	ORP (360)
λ (nm)				CC2[2]			
355	−6194.8	−6257.7	−6347.4	–	−6371.6	−6434.9	−6166.0
436	−2199.1	−2211.8	−2248.0	–	−2250.1	−2265.1	−2194.8
589	−814.3	−817.1	–	–	−831.3	–	−814.1
633	−667.1	−669.2	–	–	−680.8	–	−667.1
				CCSD[2]			
355	−3896.0	−3923.0	−3818.8	–	−3902.3	–	−3840.3
436	−1462.4	−1467.2	–	–	−1466.3	–	−1447.4
589	−559.9	−560.5	–	−556.4	−561.5	–	–
633	−460.8	−461.2	–	–	−462.2	–	−457.4

[1] Hexane solution experimental rotations from Ref. 58, (589 nm) -1146.0

[2] Modified dipole-velocity gauge.

Table 3.9: Specific rotations (deg dm^{-1} (g/mL)$^{-1}$) for (1*R*,5*R*)-*β*-pinene[1]. All results except those for the ORP basis reproduced from Mach and Crawford.[14]

Basis set (# fxns)	aDZ (374)	daDZ (528)	aTZ (828)	daTZ (1132)	LPol-ds (568)	ORP (528)
λ (nm)			CC2[2]			
355	−202.9	−203.7	–	–	−187.8	−188.6
436	−79.1	−80.2	–	–	−73.5	–
589	−25.5	−26.2	–	–	−23.4	–
633	−20.0	−20.3	–	–	−18.4	−18.5
			CCSD[2]			
355	−84.7	−85.9	–	–	−74.1	−75.8
436	−21.7	–	–	–	–	–
589	−0.7	–	–	–	–	–
633	0.7	0.4	–	–	2.0	1.7

[1] Gas-phase experimental rotations from Ref. 25, (355 nm) -69.7 ± 3.2, (633 nm) 4.7 ± 0.6
[2] Modified dipole-velocity gauge.

The remaining two test systems, (1*S*,4*S*)-norbornenone (Table 3.8) and (1*R*,5*R*)-*β*-pinene (Table 3.9), both exhibit very little basis set dependence and their size limits the basis sets we are capable of studying at the CC level of theory. For (1*S*,4*S*)-norbornenone the CC2 ORP results are extremely similar to those of aDZ, even producing the same rotation of -667.1 deg dm^{-1} (g/mL)$^{-1}$ at 633 nm. For the CCSD level of theory at 355 nm the ORP rotation of -3840.3 deg dm^{-1} (g/mL)$^{-1}$ is between the rotations for aDZ (-3896.0 deg dm^{-1} (g/mL)$^{-1}$) and aTZ (-3818.8 deg dm^{-1} (g/mL)$^{-1}$) and is slightly smaller than the -3902.3 deg dm^{-1} (g/mL)$^{-1}$ of LPol-ds, which according to the aTZ and daTZ results puts ORP closer to the basis set limit than LPol-ds. The available (1*R*,5*R*)-*β*-pinene ORP rotations with the ORP basis are sparse, but they demonstrate that it works as well as the LPol-ds set does for large systems at both CC2 and CCSD levels of theory. Additionally, this is another example of a system whose dispersion curve is bisignate at the CCSD level and the ORP

basis captures this as well as the daDZ and LPol-ds bases do.

3.2.4 Conclusions

In our test set of four molecules, (*S*)-methyloxirane, (*R*)-fluorooxirane, (1*S*,4*S*)-norbornenone, and (1*R*,5*R*)-β-pinene, coupled cluster level optical rotations computed with the ORP basis set are at least as good and often better than those computed with either the Dunning or LPol basis sets. In the cases of high basis set dependence studied here ((*S*)-methyloxirane and (*R*)-fluorooxirane) the ORP basis performed as well as much larger sets. In the case of lower basis set dependence, which in this case corresponded to molecules made purely of carbon and hydrogen ((1*S*,4*S*)-norbornenone and (1*R*,5*R*)-β-pinene), it performed at least as well as comparably sized basis sets. While the improvement to CC level optical rotations computed with the ORP basis set is not as drastic as to those computed at the B3LYP level of theory (as was the case with the LPol basis sets in Section 3.1) we recommend its use in such computations. The admirable performance of the ORP basis set for (*R*)-fluorooxirane is especially influential in our recommendation as it has the highest basis set dependence of the systems tested here. Most importantly, this dependence included a change in the nature of the dispersion curve from monosignate to bisignate, behavior that is properly captured by the ORP basis from the outset.

Chapter 4

Gauge Invariant Coupled Cluster Response Properties

This chapter opens with published work (Section 4.1) examining optical rotations computed at the coupled cluster doubles level of theory using optimized orbitals as an initial proof of concept for gauge invariant optical rotations. This is followed by a discussion of the theory of a truly gauge invariant CC linear response formalism and our advances towards an implementation of such a theory for computing optical rotations in Section 4.2.

4.1 The Optimized Orbital Coupled Cluster Doubles Method and Optical Rotation

Reprinted with permission from G. D. Lindh, T. J. Mach, and T. D. Crawford. *Chem. Phys.*, 401:125–129, 2012.

4.1.1 Introduction

Enantiomeric pairs of chiral molecules may be distinguished from one another spectroscopically through a variety of optical responses in refraction (optical rotation or circular birefringence), absorption (circular dichroism), or scattering (Raman optical activity).[5] However, the assignment of the absolute stereochemical configuration of a given enantiomer is possible only if the sign of its response is known in advance, and first-principles computations of chiroptical properties can often provide a reference point for such identifications. Over the last fifteen years, quantum chemical methods for predicting chiral responses have seen tremendous advances. For example, the most common chiral property measured in synthetic laboratories is optical rotation, the first *ab initio* calculations of which were carried out by Polavarapu[22] at the Hartree-Fock self-consistent field (SCF) level of theory in 1997. Since that time, the theory has been extended to methods that include essential electron correlation effects, such as density-functional theory (DFT)[15,23,54,65–67] and coupled cluster theory,[8,24,33,66] and the latter have been found to provide highly accurate rotations when compared with experimental gas-phase measurements.[18,27]

A complication arising in the simulation of chiroptical spectra is gauge invariance — specifically in the choice of representation of the electric-dipole operator in either the "length gauge", in which $\vec{\mu} = -\vec{r}$, or the "velocity gauge", where the linear momentum $-\vec{p}$ is used instead.[68] For quantum chemical methods in which the underlying molecular orbitals are variationally optimized, such as SCF, multiconfigurational SCF (MCSCF), or Kohn-Sham DFT, the two options yield identical results in the limit of a complete one-electron basis set. However, for conventional coupled cluster theory, in which a fixed set of orbitals is used, the conundrum remains even in the complete basis-set limit and even when gauge-including atomic orbitals (GIAOs) are employed.[46,69,70] For example, for the problematic chiral molecule (*1S,4S*)-norbornenone, the coupled cluster singles and doubles (CCSD) approach gives a sodium D-line specific rotation of -737 deg dm^{-1} (g/mL)$^{-1}$ in the length gauge, and -412 deg dm^{-1} (g/mL)$^{-1}$ in the velocity gauge with a correlation consistent double-zeta basis set augmented with diffuse functions. In addition, this lack of invariance results in an artificial origin dependence in the length representation, as well as an unphysical non-zero specific rotation in the static-field limit in the velocity representation. (Pedersen and co-workers have suggested a "modified velocity gauge" correction for the latter, in which the $\omega = 0$ value is subtracted from the desired non-zero result.[26] For the norbornenone case above, this yields an origin-independent specific rotation of -561 deg dm^{-1} (g/mL)$^{-1}$, roughly halfway between its length and velocity counterparts.)

Gauge invariance can be achieved within the coupled cluster model through a careful reformulation of the response theory[71] in conjunction with the variational optimization of the

correlation energy with respect to the molecular orbitals — the OO-CC method. A key to this approach is the formulation of the orbital rotations as coupled excitation/de-excitation pairs in a manner analogous to that appearing in the random-phase approximation (RPA).[72] Pedersen, Koch, and co-workers described such an approach more than ten years ago[68,73] and applied it to the computation of oscillator strengths in UV/Vis absorption spectra.[74,75]

Optimized orbitals have been considered several times within the context of coupled cluster theory, beginning with the work of Purvis and Bartlett in 1982 when they demonstrated the relative insensitivity of the CCSD method to the choice of reference wave function.[76] Later, Scuseria and Schaefer[77] used the orbital Z-vector approach from analytic gradient theory to optimize the orbitals with the coupled cluster doubles method (OO-CCD), and found them to be comparable to Brueckner-type orbitals.[78,79] More than a decade later, Sherrill *et al.* reported[80] an efficient implementation of OO-CCD, which they applied to artifactual symmetry-breaking problems in O_4^+. Soon thereafter, Krylov *et al.* reported[81] an active-space variant of OO-CCD as an alternative to complete-active-space SCF (CASSCF) wave functions for describing non-dynamical correlation effects, an approach that was extended by Gwaltney *et al.* to include dynamical correlation effects via perturbational corrections[82] and by Krylov *et al.* to electronically excited states.[83]

The purpose of the present work is to examine the impact of the use of optimized orbitals in the coupled cluster framework on the optical rotations of chiral compounds. While the implementation reported here is not (yet) gauge invariant, it represents a necessary step towards achieving such invariance for the first time for chiroptical properties, for which the

distinction between length and velocity representations can be dramatic. In subsequent subsections, we briefly describe the theoretical underpinnings of the OO-CCD approach, followed by the first application of optimized orbitals to the computation of the coupled cluster linear response function. Our test set of chiral compounds includes a number of problematic cases, including (*S*)-methyloxirane and (*1S,4S*)-norbornenone.

4.1.2 Computational Details

In the OO-CC approach,[76,77,80] the coupled cluster correlation energy functional,[12,84]

$$E_{\mathrm{CC}} = \langle 0| \left(1 + \hat{\Lambda}\right) e^{-\hat{T}} \hat{H} e^{\hat{T}} |0\rangle \,, \tag{4.1}$$

is optimized with respect to rotations among the molecular orbitals, *i.e.*,

$$\frac{\partial E_{\mathrm{CC}}}{\partial \kappa_{ai}} = 0. \tag{4.2}$$

In the above equations, the cluster operator, $\hat{T}$, generates at least doubly excited determinants from the reference wave function, $|0\rangle$, and $\hat{\Lambda}$ is a corresponding de-excitation operator. The dependence on the orbital rotation parameters, κ_{ai} (where a and i index virtual and occupied molecular orbitals, respectively) is implicit in the above notation, though a more explicit formulation is often advantageous.[68,75,80] The energy derivative with respect to orbital rotations in Eq. (4.2) is obtained naturally as the so-called orbital Lagrangian[85] of analytic gradient theory,[77,86–88] which appears as the inhomogeneous term in the linear Z-vector equations of Handy and Schaefer.[89] As shown by Scuseria and Schaefer,[77] the Z-vector

itself serves as the orbital rotation parameters via a unitary transformation operator, $\exp(Z)$, and iterative optimization of the orbitals using this transformation ultimately satisfies the condition in Eq. (4.2). The OO-CC approach typically excludes single excitations from the definitions of the $\hat{T}$ and $\hat{\Lambda}$ operators, as these exhibit considerable linear dependence upon the orbital rotation parameters themselves.[77,80] An important repercussion of this choice is that the OO-CC method is not formally exact, unlike its conventional CC counterpart, as shown by Köhn and Olsen.[90]

In the present implementation, the $\hat{T}$ and $\hat{\Lambda}$ equations are limited to double excitations (OO-CCD) and solved using an initial set of Hartree-Fock orbitals. The resulting cluster amplitudes are then used to build the orbital Lagrangian and associated Z-vector and to compute a new set of orthonormal orbitals, which subsequently parametrize a new set of amplitude equations. This process is repeated until Eq. (4.2) is satisfied to some specified numerical criterion (typically 10^{-5}). As demonstrated by Sherrill *et al.*,[80] this approach can be somewhat streamlined by fusing the computation of the cluster amplitudes, orbital Lagrangian, and new orbitals, but this technique is not employed in the present pilot implementation. Once the orbital macroiterations have converged, perturbed wave functions with respect to electric- and magnetic-dipole moments are computed and used to obtain the standard coupled cluster optical activity tensor,

$$\mathbf{G}'(\omega) = -\frac{2\omega}{\hbar} \sum_{j \neq 0} \frac{\mathrm{Im}(\langle \psi_0 | \boldsymbol{\mu} | \psi_j \rangle \langle \psi_j | \mathbf{m} | \psi_0 \rangle)}{\omega_{j0}^2 - \omega^2}. \tag{4.3}$$

However, the sum over states implied by the above equation is avoided in our work through the use of the coupled cluster linear response function,[37] which is mathematically equivalent,

but significantly less computationally demanding to evaluate.[91] The specific rotation [the total rotation normalized for concentration and path length, in units of deg dm^{-1} $(g/mL)^{-1}$] is obtained through the trace of the $\mathbf{G}'(\omega)$ tensor.[8,27] It should be noted that, while the $\hat{T}$ and $\hat{\Lambda}$ operators are limited to include only double excitations, the perturbed wave functions must include singles as well, because the latter contain the leading-order contribution to the response. (For example, the first-order contribution to the electric-dipole perturbed wave function involves dipole integrals divided by orbital energy denominators, which correspond to matrix elements between the reference and singly excited determinants.) In addition, we note that a more complete derivation of the OO-CCD linear response requires proper consideration of the orbital rotations (both excitations and de-excitations), which should play the role of the singles ($\hat{T}_1$ and $\hat{\Lambda}_1$) parameters in the corresponding CCSD approach. This has not been done in the present work because our goal is to examine primarily the variation of chiroptical properties using current (non-gauge-invariant) methods with the choice of orbtials (Hartree-Fock vs. CC optimized orbitals). In a future study, we will report a complete implementation of a gauge-invariant formulation of OO-CCD response theory. The specific rotations reported in this work were computed using the modified velocity gauge (MVG) of Pedersen and co-workers,[26] and are thus origin independent (but not gauge invariant).

Four chiral molecules were chosen to test the OO-CCD approach: (*S*)-methyloxirane, (*S*)-methylthiirane, (*S*)-2-chloropropionitrile, and (*1S,4S*)-norbornenone. Each of these compounds has been considered in earlier work and the equilibrium structures used here are

the same as those described in previous studies.[27,33,35,36] In addition, pyramidalized fluoroformaldehyde and hydrogen peroxide are also considered for benchmarking. The correlation-consistent basis sets of Dunning[48] augmented with diffuse functions[49,50] were used in all cases, and core orbitals ($1s$ for carbon, oxygen, and nitrogen; $1s2s2p$ for sulfur and chlorine) were held frozen. All computations reported here were carried out using a locally modified version of the PSI3 suite of quantum chemical programs.[39]

4.1.3 Results and Discussion

Table 4.1 reports RHF-CCSD and OO-CCD specific rotations of four of the test molecules at polarized field wavelengths of 633, 589, 436, and 355 nm. Not surprisingly, given the relatively simple electronic structures of the four test molecules, Hartree-Fock and CC optimized orbitals yield essentially identical specific rotations, with the largest absolute discrepancy between the two approaches occurring for (*1S,4S*)-norbornenone at shorter wavelengths. We consider this a positive result, given the observed reliability of CCSD in reproducing gas-phase specific rotations.[27] Although only MVG results are reported in Table 4.1 (because of their origin independence), it is worth noting that the disagreement between RHF-CCSD and OO-CCD is even smaller for the length-gauge rotations, but actually somewhat larger for the velocity-gauge itself. For example, the 355 nm specific rotation of (*S*)-methyloxirane in the length gauge is -50.8 and -50.5 deg dm^{-1} (g/mL)$^{-1}$ for the RHF-CCSD and OO-CCD methods, respectively, while the velocity-gauge rotation for each method is -323.6 and -335.8 deg dm^{-1} (g/mL)$^{-1}$. (The shift of the velocity-gauge rotations by their zero-frequency coun-

Table 4.1: Coupled cluster specific rotations using Hartree-Fock orbitals (CCSD) and variationally optimized orbitals (OO-CCD).[a]

	(*S*)-methyloxirane	(*S*)-methylthiirane	(*S*)-2-chloropropionitrile	(1*S*,4*S*)-norbornenone
Wavelength			RHF-CCSD	
355 nm	-56.4	-146.0	-25.8	-3896.0
436 nm	-48.4	-121.8	-14.4	-1462.4
589 nm	-30.1	-70.7	-6.8	-559.9
633 nm	-26.5	-61.4	-5.8	-460.8
			OO-CCD	
355 nm	-57.3	-147.2	-25.8	-4033.0
436 nm	-49.4	-122.6	-14.3	-1490.8
589 nm	-30.7	-71.1	-6.8	-567.9
633 nm	-27.0	-61.8	-5.7	-467.1

[a] Specific rotations are given in deg dm^{-1} $(g/mL)^{-1}$ using the modified velocity gauge and the aug-cc-pVDZ basis set.

terparts to produce the MVG results removes almost all of this difference.) On the other hand, the origin-dependence vector, which depends on the mixed length-gauge/velocity-gauge polarizability tensor, is essentially identical between the two methods. In addition, the basis-set dependence of the two approaches is the same: d-aug-cc-pVDZ specific rotations of (*S*)-methyloxirane differ by only a few tenths of a deg dm^{-1} $(g/mL)^{-1}$ between RHF-CCSD and OO-CCD.

The comparison between the two methods is further supported by Figure 4.1, which presents RHF-CCSD and OO-CCD specific rotations at 589 nm for hydrogen peroxide as a function of the H−O−O−H dihedral angle. Again, the two methods yield nearly identical results, including the well known $\sin(2\theta)$ dependence of the specific rotation on the torsional motion.[92] The largest differences occur at the extrema of the curves at only *ca.* 8 deg dm^{-1} $(g/mL)^{-1}$.

Larger discrepancies between the RHF-CCSD and OO-CCD approaches can be expected when the contributions of singly excited determinants become significant, *e.g.*, in electronic

Figure 4.1: Coupled cluster specific rotations [in deg dm^{-1} $(g/mL)^{-1}$] at 589 nm for hydrogen peroxide as a function of the H−O−O−H dihedral angle using Hartree-Fock orbitals (CCSD) and variationally optimized orbitals (OO-CCD) and the aug-cc-pVDZ basis set. The two methods yield essentially identical results.

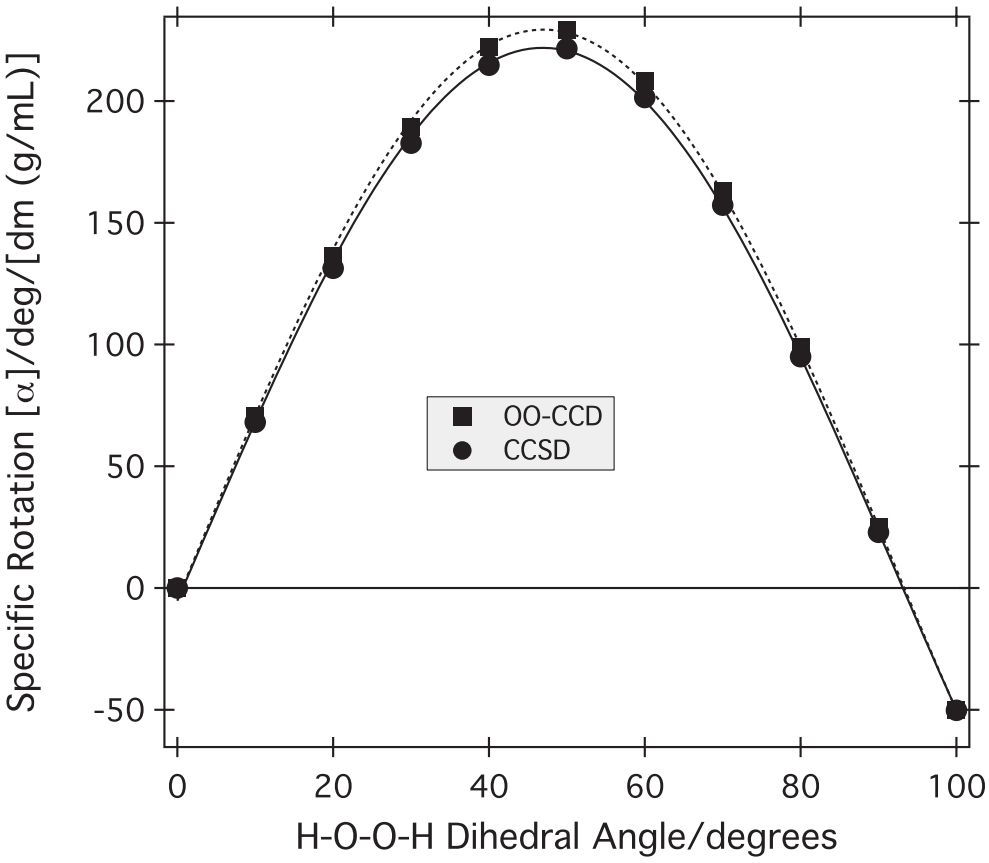

structures with partial or strong multireference character. (Indeed, this was the motivation of Sherrill *et al.* in pursuing the OO-CCD method for symmetry breaking problems in the first place.[80]) In order to examine such a circumstance, Table 4.2 reports specific rotations for several structures of (*S*)-methyloxirane for which the C−O bond involving the stereogenic carbon is stretched away from its equilibrium value of 1.442 Å. Divergence between the two methods is observed even after a shift of only 0.1 Å, with the 355 nm rotations differing by more than 30 deg dm^{-1} $(g/mL)^{-1}$. The discrepancies increase dramatically as the bond

Table 4.2: Coupled cluster specific rotations of stretched (*S*)-methyloxirane using Hartree-Fock orbitals (CCSD) and variationally optimized orbitals (OO-CCD).[a]

.

r(C−O)/Å	1.442	1.542	1.642	1.742	1.842
Wavelength			RHF-CCSD		
355 nm	-56.4	-101.4	-154.5	-179.4	70.2
436 nm	-48.4	-81.6	-118.5	-149.0	-140.9
589 nm	-30.1	-48.3	-67.3	-83.2	-83.7
633 nm	-26.5	-42.1	-58.4	-71.9	-72.1
			OO-CCD		
355 nm	-57.3	-134.2	-230.5	-347.7	-449.1
436 nm	-49.4	-95.1	-152.0	-219.0	-285.7
589 nm	-30.7	-53.4	-81.2	-112.3	-139.7
633 nm	-27.0	-46.4	-69.9	-96.1	-118.6
$\hat{T}_1$ diagnostic[b]	0.012	0.014	0.017	0.020	0.025

[a] Specific rotations are given in deg dm^{-1} $(\mathrm{g/mL})^{-1}$ using the modified velocity gauge and the aug-cc-pVDZ basis set.
[b] Computed using the RHF-CCSD wave function.

is stretched further, and the OO-CCD approach yields much larger (absolute) rotations than RHF-CCSD in this case. We note that the magnitude of the $\hat{T}_1$ diagnostic,[93] which is sometimes used as a measure of the reliability of the CC method, remains below the conventional cutoff of 0.02 even as the two methods disagree substantially as to the magnitude of the specific rotations. Interestingly, the RHF-CCSD method exhibits a singularity between r(C−O) =1.742 and 1.842 Å, as indicated by the change in sign of the 355 nm rotation in Table 4.2. The OO-CCD method, on the other hand, either pushes the singularity further away or perhaps changes the sign of the pole (which would indicate a reversal in the order of the lowest-lying excited state(s) between the two methods).

An important chromophore in the optical activity of many chiral compounds, including that of norbornenone, is the carbonyl group, which gives rise to an $n \rightarrow \pi^*$ transition that

often plays a crucial role in the evaluation of the $\mathbf{G}'(\omega)$ tensor of Eq. (4.3). Table 4.3 reports coupled cluster specific rotations for a pyramidalized (and thus chiral) fluoroformaldehyde in which the DFT (B3LYP/6-31G*) optimized geometry is distorted to an F−C−O−H dihedral angle of +100.0 degrees from its C_s symmetry angle of 180.0. [Using the standard Cahn-Ingold-Prelog rules, the "empty" valence position around the carbon atom should be assigned lowest priority and thus the enantiomer is identified as (*R*) in this case.] This deformation leads to $\hat{T}_1$ diagnostic values close to the standard cutoff and relatively large differences between the RHF-CCSD and OO-CCD specific rotations, even at long wavelengths. [The 589 nm rotation differs by roughly 40 deg dm^{-1} (g/mL)$^{-1}$, for example.] As the C=O bond is stretched away from its "equilibrium" value of 1.186 Å, the disagreement between the methods is magnified, such that even the position of the pole is changed. A distortion of the carbonyl bond by 0.1 Å leads to a difference of 85 deg dm^{-1} (g/mL)$^{-1}$ at 589 nm. When the C=O bond is further extended by 0.13 Å to 1.306 Å, the OO-CCD method exhibits a singularity due to near resonance of its lowest $n \rightarrow \pi^*$ transition at 3.57 eV with the external field at 355 nm (3.50 eV). The RHF-CCSD method exhibits a similar pole, but at somewhat longer bond lengths, as indicated in Table 4.3.

The importance of vibrational effects on specific rotations is now well documented,[28,34,52,55,94–96] and thus the repercussions of the intensified structural dependence revealed by the above examples may include an correspondingly enhanced vibrational dependence in some cases. For methyloxirane, in particular, the incorporation of zero-point vibrational motions (including anharmonic contributions) has been shown to be essential (along with high levels of

Table 4.3: Coupled cluster specific rotations of pyramidalized fluoroformaldehyde[a] using Hartree-Fock orbitals (CCSD) and variationally optimized orbitals (OO-CCD).[b]

.

r(C=O)/Å	1.186	1.286	1.296	1.306	1.316
Wavelength			RHF-CCSD		
355 nm	1152.0	1775.1	1994.8	2601.3	$-\infty$
436 nm	643.3	759.4	757.0	748.8	733.1
589 nm	314.0	360.6	359.8	357.3	352.8
633 nm	267.3	306.4	305.8	304.0	300.5
			OO-CCD		
355 nm	1394.7	4126.4	7062.0	$+\infty$	−5135.6
436 nm	741.6	1038.9	1079.0	1124.2	1176.1
589 nm	353.5	445.7	453.1	460.0	466.3
633 nm	300.0	374.9	380.7	385.9	390.5
$\hat{T}_1$ diagnostic[c]	0.019	0.023	0.023	0.023	0.024

[a] Chiroptical data correspond to the (*R*) enantiomer.
[b] Specific rotations are given in deg dm^{-1} (g/mL)$^{-1}$ using the modified velocity gauge and the aug-cc-pVDZ basis set.
[c] Computed using the RHF-CCSD wave function.

electron correlation and large, diffuse basis sets) in order to reproduce the gas-phase experimental specific rotation at 355 nm.[34,52,95] Figure 4.2 plots selected data from Table 4.2 for (*S*)-methyloxirane, as well as interpolating curves obtained by least squares fits to a simple Gaussian function. From this analytic form, the slope and curvature — which are related, respectively, to anharmonic and harmonic vibrational corrections — of the specific rotation as a function of the C−O distance can be computed trivially at the equilibrium structure. Even for the longest wavelength (633 nm), the two differ substantially: for RHF-CCSD the slope and gradient are -143 deg dm^{-1} (g/mL)$^{-1}$/Å and -316 deg dm^{-1} (g/mL)$^{-1}$/Å^2, respectively, while the corresponding values for OO-CCD are -171 deg dm^{-1} (g/mL)$^{-1}$/Å and -461 deg dm^{-1} (g/mL)$^{-1}$/Å^2. These differences are magnified at shorter wavelengths, but the slope computed with the OO-CCD method is consistently larger than that given by

RHF-CCSD.

Figure 4.2: Coupled cluster specific rotations [in deg dm^{-1} $(g/mL)^{-1}$] at 589 and 355 nm for stretched (*S*)-methyloxirane using Hartree-Fock orbitals (CCSD) and variationally optimized orbitals (OO-CCD) and the aug-cc-pVDZ basis set. The OO-CCD approach exhibits a significantly stronger geometry dependence than RHF-CCSD.

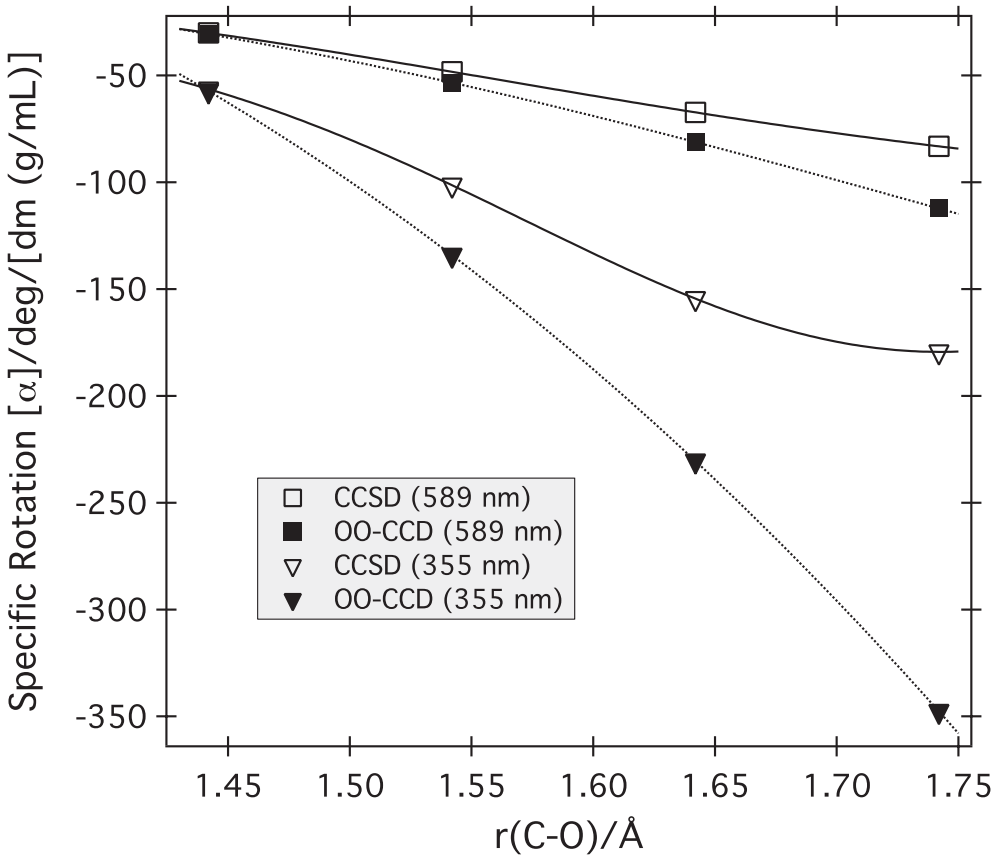

4.1.4 Conclusions

We have extended the optimized orbital coupled cluster (OO-CC) method to the computation of optical rotations of chiral compounds as a first step towards the implementation of a gauge-invariant formulation of coupled cluster response theory. For molecules with relatively simple electronic structures, such as the singlet ground states of the organic compounds examined

here, the OO-CCD approach yields specific rotations that are essentially identical to those obtained using conventional Hartree-Fock orbitals. This result is both unsurprising and welcome because the insensitivity of coupled cluster theory has been known since the original formulation of the CCSD method by Purvis and Bartlett nearly three decades ago[76] and because the success observed to date for CC linear response theory in reproducing gas-phase specific rotations is thus further solidified. However, molecules exhibiting even moderate multireference character, such as that arising from the stretching of bonds in a chemical reaction, produce substantial differences between the OO-CCD and RHF-CCSD methods. Furthermore, for the systems considered in this work, the OO-CCD method consistently displays much greater variation with respect to distortion of the molecular geometry than its RHF-based counterpart. This observation may have an impact on the computation of zero-point and temperature-dependent vibrational corrections, and future systematic studies of this effect are clearly warranted. The source of these discrepancies may reside in the fact that the response of the orbital rotation parameters, which play the role of the singles in the response function, has not been taken into account in the present implementation. On the other hand, it remains to be seen whether a fully gauge-invariant formulation of the coupled cluster linear response function, which is currently in progress, will perhaps ameliorate the structural dependence introduced by the use of variationally optimized orbitals.

4.2 Towards Gauge Invariant Coupled Cluster Response Properties

A standalone orbital optimization procedure is not adequate to achieve gauge invariance; instead a reformulation of CC response theory is required, in which orbital rotation parameters are included in the exponential *ansatz*. The orbital rotation operator takes the place of the singles excitation operator (T_1) and is of mixed excitation and de-excitation character. The presence of both excitation and de-excitation singles in the exponential changes the structure of the response equations for both the response amplitudes and response function.

4.2.1 Response Theory

According to response theory for exact states,[97,98] the expectation value of a time-independent operator A can be expanded perturbationally with respect to a time-dependent perturbation as follows

$$\langle \Psi(t)| A |\Psi(t)\rangle = \langle \Psi| A |\Psi\rangle + \langle \Psi| A |\Psi\rangle^{(1)} + \langle \Psi| A |\Psi\rangle^{(2)} + \cdots \tag{4.4}$$

which in the notation of response theory is often written

$$\langle \Psi(t)| A |\Psi(t)\rangle = \langle \Psi| A |\Psi\rangle + \langle\langle A; V(t)\rangle\rangle + \langle\langle A; V(t); V(t)\rangle\rangle + \cdots \tag{4.5}$$

where the second term on the right hand side is the linear response function, encompassing the first order response of the system to the perturbation. Expanding the CC expectation value of the A operator in an analogous way and grouping orders of perturbation

$$\begin{aligned}\langle\Phi_{\mathrm{CC}}(t)|\, A\,|\Psi_{\mathrm{CC}}(t)\rangle = \langle\Phi_{\mathrm{CC}}|\, A\,|\Psi_{\mathrm{CC}}\rangle + \sum_{\mu}\lambda_{\mu}^{(1)}(t)\,\langle\mu|\, e^{-T^{(0)}}A\,|\Psi_{\mathrm{CC}}\rangle \\ + \langle\Phi_{\mathrm{CC}}|\left[A, T^{(1)}(t)\right]|\Psi_{\mathrm{CC}}\rangle + \sum_{\mu}\lambda_{\mu}^{(2)}(t)\,\langle\mu|\, e^{-T^{(0)}}A\,|\Psi_{\mathrm{CC}}\rangle \\ + \langle\Phi_{\mathrm{CC}}|\left[A, T^{(2)}(t)\right]|\Psi_{\mathrm{CC}}\rangle + \sum_{\mu}\lambda_{\mu}^{(1)}(t)\,\langle\mu|\, e^{-T^{(0)}}\left[A, T^{(1)}(t)\right]|\Psi_{\mathrm{CC}}\rangle \\ + \frac{1}{2}\,\langle\Phi_{\mathrm{CC}}|\left[\left[A, T^{(1)}(t)\right], T^{(1)}(t)\right]|\Psi_{\mathrm{CC}}\rangle + \cdots\end{aligned} \tag{4.6}$$

yields an expression for the CC linear response function

$$\langle\langle A; V(t)\rangle\rangle = \sum_{\mu}\lambda_{\mu}^{(1)}(t)\,\langle\mu|\, e^{-T^{(0)}}A\,|\Psi_{\mathrm{CC}}\rangle + \langle\Phi_{\mathrm{CC}}|\left[A, T^{(1)}(t)\right]|\Psi_{\mathrm{CC}}\rangle \tag{4.7}$$

Introducing Fourier transforms of the perturbed amplitudes

$$t_{\mu}^{(1)}(t) = \int_{-\infty}^{+\infty} d\omega_1 X_{\mu}^{(1)}(\omega_1) e^{(-i\omega_1)t} \tag{4.8}$$

$$\lambda_{\mu}^{(1)}(t) = \int_{-\infty}^{+\infty} d\omega_1 Y_{\mu}^{(1)}(\omega_1) e^{(-i\omega_1)t} \tag{4.9}$$

and inserting them, as well as the explicit form of $V(t)$ (shown later in Equation (4.14)) into Equation (4.7), removes all explicit time-dependence

$$\langle\langle A; V(\omega_1)\rangle\rangle = \sum_{\mu} Y_{\mu}^{(1)}(\omega_1)\,\langle\mu|\, e^{-T^{(0)}(t)}A\,|\Psi_{\mathrm{CC}}(t)\rangle + \sum_{\mu}\langle\Lambda|\,[A, \tau_{\mu}]\,|\Psi_{\mathrm{CC}}(t)\rangle\, X_{\mu}^{(1)}(\omega_1), \tag{4.10}$$

where $X_{\mu}^{(1)}(\omega_1)$ and $Y_{\mu}^{(1)}(\omega_1)$ are the frequency-dependent response amplitudes.

Programmable algebraic equations for the CC linear response function may be obtained in a straightforward manner from Equation (4.10) through the traditional derivational techniques presented earlier. Expressions for the other remaining quantity of interest, the response amplitudes — which are required to solve the CC linear response function, are obtained from examining the time evolution of the CC wavefunction.

4.2.2 Time-Dependent Coupled Cluster Theory

The time-dependent CC wavefunction

$$|\Psi_{\mathrm{CC}}(t)\rangle = e^{T(t)}\,|R\rangle\,e^{i\epsilon(t)} \tag{4.11}$$

is parametrized much the same way as the time-independent one, where now the cluster amplitudes are time-dependent

$$T(t) = \sum_{\mu} t_{\mu}(t)\tau_{\mu}, \tag{4.12}$$

and the wavefunction includes a time-dependent phase factor

$$e^{i\epsilon(t)}. \tag{4.13}$$

In the current definition of T (Equation (4.12)) μ refers to the substitution level and τ_{μ} is a substitution operator notation that compactly represents the second quantized operators in the earlier definitions of T_1 (Equation (2.15)) and T_2 (Equation (2.16)).

The time dependence of the Hamiltonian is relegated to a time-dependent perturbation $V(t)$ of the form

$$V(t) = \int_{-\infty}^{+\infty} d\omega_1 V(\omega_1) e^{(-i\omega_1)t} \tag{4.14}$$

added to the standard electronic Hamiltonian

$$H(t) = H + V(t). \tag{4.15}$$

The time derivative of the time-dependent T operator becomes just a derivative of the amplitude itself

$$\frac{d}{dt}T(t) = \sum_{\mu} \frac{dt_{\mu}(t)}{dt}\tau_{\mu} \tag{4.16}$$

making the time derivative of the wavefunction

$$\frac{d}{dt}\left|\Psi_{\mathrm{CC}}(t)\right\rangle = \sum_{\mu} \frac{dt_{\mu}(t)}{dt}\tau_{\mu}\left|\Psi_{\mathrm{CC}}(t)\right\rangle + i\frac{d\epsilon(t)}{dt}\left|\Psi_{\mathrm{CC}}(t)\right\rangle. \tag{4.17}$$

Expressions for the time evolution of the phase factor and amplitudes are determined by solving the time-dependent Schrödinger equation

$$i\frac{d}{dt}\left|\Psi_{\mathrm{CC}}(t)\right\rangle = \left(H + V(t)\right)\left|\Psi_{\mathrm{CC}}(t)\right\rangle \tag{4.18}$$

via projection onto the reference and all substituted determinants respectively.

$$i\frac{d\epsilon(t)}{dt} = \langle R|\left(\overline{H} + \overline{V}(t)\right)|R\rangle \tag{4.19}$$

$$i\frac{dt_{\nu}(t)}{dt} = \langle \nu|\left(\overline{H} + \overline{V}(t)\right)|R\rangle \tag{4.20}$$

Multiplying by $e^{-T(t)}$ prior to projection is mathematically convenient as in the time-independent case (see Equation (2.7)) and allows for the introduction of $\overline{H}$ and $\overline{V}(t)$ similarity transforms.

Expanding the cluster amplitudes in orders of the perturbation and collecting terms of similar order yields expressions for each order of amplitude

$$i\frac{dt_\nu^{(0)}(t)}{dt} = \langle\nu|\,\overline{H}\,|R\rangle \tag{4.21}$$

$$i\frac{dt_\nu^{(1)}(t)}{dt} = \langle\nu|\left[\overline{H}, T^{(1)}(t)\right]|R\rangle + \langle\nu|\,\overline{V}(t)\,|R\rangle\,, \tag{4.22}$$

where the equation for the zeroth order cluster amplitudes confirms that they are just the regular time-independent cluster amplitudes ($\overline{H}$ now only contains the similarity transform of the zeroth order Ts).

Expressions for the time evolution of the lambda amplitudes can be obtained in the same manner using the left hand CC wavefunction

$$\langle\Phi_{\rm CC}(t)| = \langle R|\,e^{-T(t)}e^{-i\epsilon(t)} + \sum_\mu \lambda_\mu(t)\,\langle\mu|\,e^{-T(t)}e^{-i\epsilon(t)} \tag{4.23}$$

and Schrödinger equation

$$\left(\frac{d}{dt}\,\langle\Phi_{\rm CC}(t)|\right)e^{T(t)} = i\,\langle\Phi_{\rm CC}(t)|\,(H+V(t))e^{T(t)}. \tag{4.24}$$

In this case the time derivative of the wavefunction has more terms

$$\begin{aligned}\frac{d}{dt}\,\langle\Phi_{\rm CC}(t)| = \Bigg(&-\sum_\nu \frac{dt_\nu(t)}{dt}\,\langle R|\,\tau_\nu - i\frac{d\epsilon(t)}{dt}\,\langle R|\, + \sum_\mu \frac{d\lambda_\mu(t)}{dt}\,\langle\mu| \\ &- \sum_\nu \frac{dt_\nu(t)}{dt}\sum_\mu \lambda_\mu(t)\,\langle\mu|\,\tau_\nu - i\frac{d\epsilon(t)}{dt}\sum_\mu \lambda_\mu(t)\,\langle\mu|\Bigg)\,e^{-T(t)}e^{-i\epsilon(t)},\end{aligned} \tag{4.25}$$

but projecting by $|R\rangle$ still yields the expression for ϵ, and projecting by $|\eta\rangle$ gives the time evolution of the lambda amplitudes. The latter is less obvious as it requires rewriting one of

the resulting terms as a commutator plus the piece of the commutator that was originally missing as well as utilization of resolution of the identity, but is ultimately of a simple form

$$\frac{d\lambda_{\mu}(t)}{dt} = i \left\langle \Phi_{\mathrm{CC}}(t) \right| \left[(\overline{H} + \overline{V}(t)), \tau_{\eta} \right] \left| R \right\rangle . \tag{4.26}$$

Expanding in orders of the perturbation and grouping like terms provides expressions for the zeroth order lambda amplitudes that are the same as the time-independent case, and first order lambdas that are dependent on the first order Ts and lambdas.

$$i\frac{d\lambda_{\nu}^{(0)}(t)}{dt} = - \left\langle R \right| (1 + \Lambda^{(0)}) \overline{H} \left| \nu \right\rangle \tag{4.27}$$

$$\begin{aligned} i\frac{d\lambda_{\nu}^{(1)}(t)}{dt} = & - \left\langle R \right| (1 + \Lambda^{(0)}) \left[\overline{H}, T^{(1)}(t) \right] \left| \nu \right\rangle - \left\langle R \right| (1 + \Lambda^{(0)}) \overline{V}(t) \left| \nu \right\rangle \\ & - \left\langle R \right| \Lambda^{(1)}(t) \overline{H} \left| \nu \right\rangle \end{aligned} \tag{4.28}$$

Using the Fourier transforms from earlier (Equations (4.8) and (4.9)) these first order response amplitude expressions can be transformed from the time to the frequency domain

$$i\omega_1 X_{\nu}^{(1)}(\omega_1) = - \left\langle \nu \right| \left[\overline{H}, X_{\mu}^{(1)}(\omega_1) \right] \left| R \right\rangle + \left\langle \nu \right| \overline{V}(\omega_1) \left| R \right\rangle \tag{4.29}$$

$$\begin{aligned} i\omega_1 Y_{\nu}^{(1)}(\omega_1) = & - \left\langle R \right| (1 + \Lambda^{(0)}) \left[\overline{H}, X_{\mu}^{(1)}(\omega_1) \right] \left| \nu \right\rangle \\ & - \left\langle R \right| (1 + \Lambda^{(0)}) \overline{V}(\omega_1) \left| \nu \right\rangle - \left\langle R \right| \Lambda^{(1)}(\omega_1) \overline{H} \left| \nu \right\rangle \end{aligned} \tag{4.30}$$

just as the response function was.

4.2.3 Gauge Invariant Coupled Cluster Response Amplitudes

The gauge invariant response amplitude expressions can be derived in much the same way as those shown above for CC response theory starting instead from the non-orthogonal orbital optimized CC (NOCC) wavefunction

$$|\Psi_{\mathrm{NOCC}}\rangle = e^{\kappa_0} e^{\kappa(t)} e^{T(t)} |R\rangle \,, \tag{4.31}$$

where the orbital rotations are defined as

$$\kappa = \sum_{\mu_1} \kappa^e_{\mu_1} \tau_{\mu_1} + \sum_{\mu_1} \kappa^d_{\mu_1} \tau^\dagger_{\mu_1}. \tag{4.32}$$

As mentioned earlier, the κs are of mixed excitation and de-excitation character. The superscript e denotes the excitation portion while d corresponds to the de-excitation part. The summation runs over μ_1 as the κs are parametrized over the singles space only, while the Ts are defined as in Equation (4.12), with the sum beginning at double excitations since the singles are accounted for by the κs. The mixed excitation and de-excitation nature of the κs means care must be exercised when differentiating, similarity transforming, and performing other algebraic manipulations as the two components naturally do not commute with each other, and the de-excitation operator does not commute with the Ts either. The time derivative of the wavefunction in this case is

$$\begin{aligned} \frac{d}{dt} |\Psi_{\mathrm{NOCC}}(t)\rangle = &\sum_{\mu_1} \frac{d\kappa^e_{\mu_1}(t)}{dt} e^{\kappa_0} \tau_{\mu_1} e^{\kappa(t)} e^{T(t)} |R\rangle + \sum_{\mu_1} \frac{d\kappa^d_{\mu_1}(t)}{dt} e^{\kappa_0} e^{\kappa(t)} \tau^\dagger_{\mu_1} e^{T(t)} |R\rangle \\ &+ \sum_{\mu} \frac{dt_\mu(t)}{dt} e^{\kappa_0} e^{\kappa(t)} \tau_\mu e^{T(t)} |R\rangle \end{aligned} \tag{4.33}$$

where the $\tau_{\mu_1}^\dagger$ is to the right of the exponential due to the form of the exponential

$$e^{\kappa(t)} = e^{\kappa^e(t)} e^{\kappa^d(t)}. \tag{4.34}$$

Plugging the wavefunction derivative into the time-dependent Schrödinger equation and left multiplying by $e^{-T(t)} e^{-\kappa(t)} e^{-\kappa_0}$ for convenience

$$e^{-T(t)} e^{-\kappa(t)} e^{-\kappa_0} i \frac{d}{dt} |\Psi_{\mathrm{NOCC}}(t)\rangle = e^{-T(t)} e^{-\kappa(t)} e^{-\kappa_0} (H + V(t)) |\Psi_{\mathrm{NOCC}}(t)\rangle \tag{4.35}$$

and similarity transforming by the zeroth order orbital rotations

$$e^{-\kappa_0}(H + V(t))e^{\kappa_0} = \widetilde{H} + \widetilde{V}(t) \tag{4.36}$$

simplifies the equation slightly

$$\begin{aligned} &i \sum_{\mu_1} \frac{d\kappa^e_{\mu_1}(t)}{dt} e^{-T(t)} e^{-\kappa(t)} \tau_{\mu_1} e^{\kappa(t)} e^{T(t)} |R\rangle + i \sum_{\mu_1} \frac{d\kappa^d_{\mu_1}(t)}{dt} e^{-T(t)} \tau^\dagger_{\mu_1} e^{T(t)} |R\rangle \\ &+ i \sum_{\mu} \frac{dt_\mu(t)}{dt} e^{-T(t)} \tau_\mu e^{T(t)} |R\rangle = e^{-T(t)} e^{-\kappa(t)} (\widetilde{H} + \widetilde{V}(t)) e^{\kappa(t)} e^{T(t)} |R\rangle \end{aligned} \tag{4.37}$$

Projecting by the set of all doubly excited determinants, writing the time-dependent similarity transforms as a series of nested commutators, and retaining only terms that are first order in the perturbation yields the equation for the perturbed doubles cluster amplitudes

$$\begin{aligned} i \frac{dt^{(1)}_\nu(t)}{dt} = &\langle \nu | e^{-T^{(0)}(t)} \left[\widetilde{H}, \kappa^{e(1)}_{\mu_1}(t) \right] |\Psi_0\rangle + \langle \nu | e^{-T^{(0)}(t)} \left[\widetilde{H}, T^{(1)}_\mu(t) \right] |\Psi_0\rangle \\ &+ \langle \nu | e^{-T^{(0)}(t)} \left[\widetilde{H}, \kappa^{d(1)}_{\mu_1}(t) \right] |\Psi_0\rangle \\ &- i \sum_{\mu_1} \frac{d\kappa^{d(1)}_{\mu_1}(t)}{dt} \langle \nu | e^{-T^{(0)}(t)} \tau^\dagger_{\mu_1} |\Psi_0\rangle + \langle \nu | e^{-T^{(0)}(t)} \widetilde{V}(t) |\Psi_0\rangle , \end{aligned} \tag{4.38}$$

where $|\Psi_0\rangle$ is the zeroth order right-hand NOCC wavefunction

$$|\Psi_0\rangle = e^{T^{(0)}} |R\rangle \,. \tag{4.39}$$

The frequency dependent expression is again obtained by inserting Fourier transforms of the same form as Equations (4.8) and (4.9) and differentiating

$$\begin{aligned} i\omega_1 X_\nu^{(1)}(\omega_1) = &\langle\nu| e^{-T^{(0)}} \left[\widetilde{H}, K_{\mu_1}^{e(1)}(\omega_1)\right] |\Psi_0\rangle + \langle\nu| e^{-T^{(0)}} \left[\widetilde{H}, X_\mu^{(1)}(\omega_1)\right] |\Psi_0\rangle \\ &+ \langle\nu| e^{-T^{(0)}} \left[\widetilde{H}, K_{\mu_1}^{d(1)}(\omega_1)\right] |\Psi_0\rangle \\ &- i\sum_{\mu_1} \omega_1 \langle\nu| e^{-T^{(0)}} K_{\mu_1}^{d(1)}(\omega_1) |\Psi_0\rangle + \langle\nu| e^{-T^{(0)}} \widetilde{V}(\omega_1) |\Psi_0\rangle \,. \end{aligned} \tag{4.40}$$

The equations for the three other parameters of interest $K_{\mu_1}^e(\omega_1)$, $K_{\mu_1}^d(\omega_1)$, and $Y_\nu(\omega_1)$, in the frequency domain are below:

$$\begin{aligned} \omega_1 \langle\Phi_0| \left[\tau_{\nu_1}^\dagger, K_{\mu_1}^{e(1)}(\omega_1)\right] |\Psi_0\rangle = &\langle\Phi_0| \left[\left[\widetilde{H}, \tau_{\nu_1}^\dagger\right], K_{\mu_1}^{e(1)}(\omega_1)\right] |\Psi_0\rangle + \langle\Phi_0| \left[\left[\widetilde{H}, \tau_{\nu_1}^\dagger\right], X_\mu^{(1)}(\omega_1)\right] |\Psi_0\rangle \\ &+ \langle\Phi_0| \left[\left[\widetilde{H}, \tau_{\nu_1}^\dagger\right], K_{\mu_1}^{d(1)}(\omega_1)\right] |\Psi_0\rangle \\ &+ Y_\mu^{(0)}(\omega_1) \langle\mu| e^{-T^{(0)}} \left[\widetilde{H}, \tau_{\nu_1}^\dagger\right] |\Psi_0\rangle - \omega_1 \langle\Phi_0| \left[\tau_{\nu_1}^\dagger, X_\mu^{(0)}(\omega_1)\right] |\Psi_0\rangle \\ &- Y_\nu^{(0)}(\omega_1) \langle\mu| e^{-T^{(0)}} \tau_{\nu_1}^\dagger |\Psi_0\rangle + \langle\Phi_0| \left[\widetilde{V}(\omega_1), \tau_{\nu_1}^\dagger\right] |\Psi_0\rangle \end{aligned} \tag{4.41}$$

$$\begin{aligned} -\omega_1 \langle\Phi_0| \left[\tau_{\nu_1}, K_{\mu_1}^{d(1)}(\omega_1)\right] |\Psi_0\rangle = &\langle\Phi_0| \left[\left[\widetilde{H}, \tau_{\nu_1}\right], K_{\mu_1}^{e(1)}(\omega_1)\right] |\Psi_0\rangle + \langle\Phi_0| \left[\left[\widetilde{H}, \tau_{\nu_1}\right], X_\mu^{(1)}(\omega_1)\right] |\Psi_0\rangle \\ &+ \langle\Phi_0| \left[\left[\widetilde{H}, \tau_{\nu_1}\right], K_{\mu_1}^{d(1)}(\omega_1)\right] |\Psi_0\rangle \\ &+ Y_\nu^{(0)}(\omega_1) \langle\nu| e^{-T^{(0)}} \left[\widetilde{H}, \tau_{\mu_1}\right] |\Psi_0\rangle + \langle\Phi_0| \left[\widetilde{V}(\omega_1), \tau_{\nu_1}\right] |\Psi_0\rangle \end{aligned} \tag{4.42}$$

$$\begin{aligned} \omega_1 Y_\nu^{(1)}(\omega_1) = &\langle\Phi_0| \left[\left[\widetilde{H}, \tau_\nu\right], K_{\mu_1}^{e(1)}(\omega_1)\right] |\Psi_0\rangle + \langle\Phi_0| \left[\left[\widetilde{H}, \tau_\nu\right], X_\mu^{(1)}(\omega_1)\right] |\Psi_0\rangle \\ &+ \langle\Phi_0| \left[\left[\widetilde{H}, \tau_\nu\right], K_{\mu_1}^{d(1)}(\omega_1)\right] |\Psi_0\rangle + \langle\nu| e^{-T^{(0)}} \left[\widetilde{H}, Y_\mu^{(1)}(\omega_1)\right] |\Psi_0\rangle \\ &+ \omega_1 \langle\Phi_0| \left[\tau_\nu, K_{\mu_1}^{d(0)}(\omega_1)\right] |\Psi_0\rangle + \langle\Phi_0| \left[\widetilde{V}(\omega_1), \tau_\nu\right] |\Psi_0\rangle \,, \end{aligned} \tag{4.43}$$

where the zeroth order left-hand NOCC wavefunction

$$\langle \Phi_0 | = \langle R | \, e^{-T^{(0)}} + \sum_{\mu} \lambda_{\mu}^{(0)} \, \langle \mu | \, e^{-T^{(0)}} \tag{4.44}$$

has been used.

It is perhaps not obvious, as they are hidden in similarity transformations and zeroth order wavefunctions, that the static limit amplitudes $\kappa_{\mu_1}^{e}$, t_{μ}, $\kappa_{\mu_1}^{d}$, and λ_{μ} must also be obtained. The static limit equations are very similar to those of standard CC theory shown earlier (Equation (2.10)).

$$0 = \langle \Phi_0 | \left[\widetilde{H}, \tau_{\mu_1}^{\dagger} \right] | \Psi_0 \rangle \tag{4.45}$$

$$0 = \langle \mu | \, e^{-T} \widetilde{H} \, | \Psi_0 \rangle \tag{4.46}$$

$$0 = \langle \Phi_0 | \left[\widetilde{H}, \tau_{\mu_1} \right] | \Psi_0 \rangle \tag{4.47}$$

$$0 = \langle \Phi_0 | \left[\widetilde{H}, \tau_{\mu} \right] | \Psi_0 \rangle \tag{4.48}$$

Just as in the standard response theory case, programmable algebraic equations may be obtained from these expressions using the standard CC diagrammatic approaches highlighted earlier (Section 2.2.1). However, there are two items of note: the first is that all commutators containing de-excitation operators must be rearranged so that all de-excitation operators are to the left of the Hamiltonian or excitation operators before converting the commutators into the connectivity relations for the diagrams. This is easily done through reversing the commutators while keeping up with any necessary sign changes. For instance the term in Equation (4.40) containing $\left[\widetilde{H}, K_{\mu_1}^{d}(\omega_1) \right]$:

$$\langle \nu | \, e^{-T^{(0)}} \left[\widetilde{H}, K_{\mu_1}^{d(1)}(\omega_1) \right] | \Psi_0 \rangle \rightarrow - \langle \nu | \, e^{-T^{(0)}} \left[K_{\mu_1}^{d(1)}(\omega_1), \widetilde{H} \right] | \Psi_0 \rangle \, . \tag{4.49}$$

Figure 4.3: Diagrammatic representation of placeholder operators used to represent τ_{μ_1} and $\tau^\dagger_{\mu_1}$ respectively. The interaction line is useful for tracking and enforcing connectivity to this amplitudeless operator, while the asterisk serves as a reminder during interpretation that the interaction line has no coefficient associated with it.

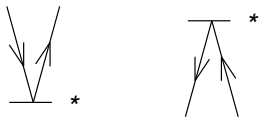

Secondly, a difference arises between the gauge invariant equations and any others seen thus far due to the presence of excitation and de-excitation operators that lack any associated coefficients (the remaining τs). In the diagrammatic techniques outlined earlier, all operators were evaluated algebraically as the associated coefficients. One way of handling these amplitudeless operators is to leave the appropriate lines from the operators they are "connected" to open; however, this complicates maintaining the correct connectivity relationships between operators as these dangling lines must be forced to come from the appropriate operators. This alteration of the diagram procedures is unusual and introduces unnecessary potential for mistakes. Using a placeholder operator eliminates this chance for mishaps and makes the connectivity immediately obvious, allowing the usual diagrammatic procedures to be used with no modifications. This placeholder operator (Figure 4.3) is represented diagrammatically by an interation line (similar to the T interaction line) with an asterisk nearby denoting the amplitudeless nature of the interaction line. During diagram interpretation this operator is ignored, contributing no coefficient and never appearing in the resulting algebra.

An example of this is seen in the first term of the expression for $K^e_{\mu_1}(\omega_1)$ (Equation (4.41)), $\langle\Phi_0|\left[\left[\widetilde{H},\tau^\dagger_{\mu_1}\right],K^e_{\nu_1}(\omega_1)\right]|\Psi_0\rangle$. Reversing the commutator and considering the Fock operator

Figure 4.4: Unique Fock operator diagrams for the reference wavefunction portion of $\langle\Phi_0|\left[\left[\widetilde{H},\tau^\dagger_{\mu_1}\right],K^e_{\nu_1}(\omega_1)\right]|\Psi_0\rangle$ contributing to the $K^e_{\mu_1}(\omega_1)$ equation (Equation (4.41)). The squiggly interaction line is used for the $K^e_{\mu_1}(\omega_1)$ as it is frequency dependent, and the tilde denotes that the Fock matrix elements are similarity transformed as in Equation (4.36).

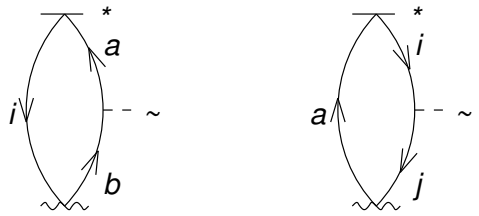

contribution to $-\langle R|\left((\tau^\dagger_{\mu_1}\widetilde{H})_{\rm c}K^e_{\nu_1}(\omega_1)\right)_{\rm c}|R\rangle$ yields the two unique diagrams shown in Figure 4.4. Enforcing the "connectivity" of the Fock fragment to the $\tau^\dagger_{\mu_1}$ operator is trivial in this case and could easily be done without the use of the placeholder operator. However, in the case of the two-electron integral terms of $\langle R|\,\Lambda_2((\tau^\dagger_{\mu_1}\widetilde{H})_{\rm c}K^e_{\nu_1}(\omega_1)T_2)_{\rm c}\,|R\rangle$ it becomes much more challenging to ensure that all 26 diagrams maintain the appropriate "connectivity". Three representative diagrams from this term are shown in Figure 4.5.

In addition to the above derivational complications, the gauge invariant response amplitudes above are all coupled to each other and must be solved simultaneously (the static amplitudes are this way as well), in contrast to the standard response theory formulation in which the time-dependent amplitudes are uncoupled and can be computed independently of one another.

Figure 4.5: Representative subset of the diagrams involving a two-electron integral fragment of the Hamiltonian for the $\langle R| \Lambda_2((\tau^\dagger_{\mu_1}\widetilde{H})_{\rm c}K^e_{\nu_1}(\omega_1)T_2)_{\rm c}\,|R\rangle$ term of the $K^e_{\mu_1}(\omega_1)$ equation. The squiggly interaction line is used for the $K^e_{\mu_1}(\omega_1)$ as it is frequency dependent, and the double dashed line denotes that the two-electron integrals have been similarity transformed as in Equation (4.36).

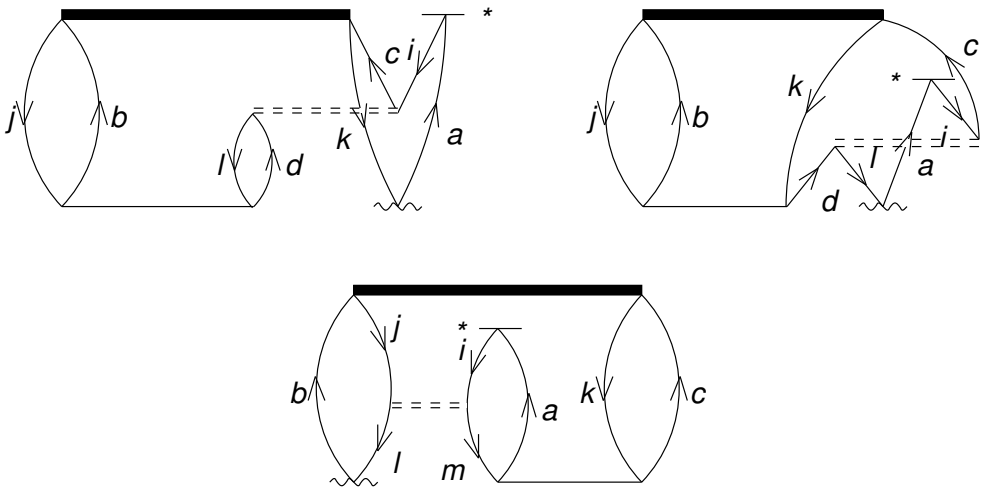

4.2.4 Gauge Invariant Coupled Cluster Response Function

The form of the gauge invariant response function is very similar to that of the response function shown earlier (Equation (4.7)). The introduction of orbital rotation parameters in the NOCC wavefunction parameterization results in additional terms in the perturbational expansion of the CC expectation value of A

$$\begin{aligned}\langle\Phi_{\rm CC}(t)|\,A\,|\Psi_{\rm CC}(t)\rangle = \langle\Phi_{\rm CC}|\,A\,|\Psi_{\rm CC}\rangle + \sum_{\mu_1}\langle\Phi_{\rm CC}|\left[A,\kappa^{e(1)}_{\mu_1}(t)\right]|\Psi_{\rm CC}\rangle \\ + \sum_{\mu}\langle\Phi_{\rm CC}|\left[A,T^{(1)}_{\mu}(t)\right]|\Psi_{\rm CC}\rangle + \sum_{\mu_1}\langle\Phi_{\rm CC}|\left[A,\kappa^{d(1)}_{\mu_1}(t)\right]|\Psi_{\rm CC}\rangle \\ + \sum_{\mu}\lambda^{(1)}_{\mu}(t)\,\langle\mu|\,e^{-T^{(0)}}A\,|\Psi_{\rm CC}\rangle + \cdots\end{aligned} \tag{4.50}$$

where only the first order terms have been shown for simplicity.

Equating orders of the CC expansion and that of exact states (Equation (4.4)) followed by Fourier transform yields the gauge invariant linear response function

$$\begin{aligned}\langle\langle A; V(\omega_1)\rangle\rangle = &\sum_{\mu_1} \langle \Phi_{\mathrm{CC}}| \left[A, \tau_{\mu_1}\right] |\Psi_{\mathrm{CC}}\rangle \, K^{e(1)}_{\mu_1}(\omega_1) + \sum_{\mu} \langle \Phi_{\mathrm{CC}}| \left[A, \tau_{\mu}\right] |\Psi_{\mathrm{CC}}\rangle \, X^{(1)}_{\mu}(\omega_1) \\ &+ \sum_{\mu_1} \langle \Phi_{\mathrm{CC}}| \left[A, \tau_{\mu_1}\right] |\Psi_{\mathrm{CC}}\rangle \, K^{d(1)}_{\mu_1}(\omega_1) + \sum_{\mu} Y^{(1)}_{\mu}(\omega_1) \, \langle \mu| \, e^{-T^{(0)}} A \, |\Psi_{\mathrm{CC}}\rangle \, .\end{aligned} \tag{4.51}$$

Utilizing this response function with the associated gauge invariant response amplitudes should produce gauge invariant linear response properties such as optical rotation. The full algebraic expressions for the NOCC response amplitudes and response function derived using diagrammatics can be seen in Appendix A.

Chapter 5

Condensed Phase Optical Rotation

The majority of experimental measurements of optical rotation are made in the condensed phase, while currently most high accuracy calculations are performed under conditions that simulate the gas phase. The leading section of this chapter (Section 5.1) presents a published study computing the optical rotation of solvated clusters via a simple many-body expansion. Sections 5.2 and 5.3 provide recent results improving this initial study and the unpublished details of the implementation utilized in the published study.

5.1 Computing Optical Rotation via an N-Body Approach

5.1.1 Introduction

Over the last two decades the quality with which optical properties of chiral molecules[5,8,17–21,100] can be computed has increased dramatically, including optical rotation,[15–17,22–24,27] electronic[74,101–110] and vibrational[111–118] circular dichroism, and Raman optical activity.[119–129] In the sixteen years since Polavarapu[22] published the first *ab initio* calculations of optical rotation, for example, comparison with *vapor phase* experimental measurements[25,53,130–134] has revealed that such response properties often require high levels of electron correlation,[24,33,34,52,95] large one-electron basis sets (including diffuse functions),[14,23,28,36,135] and, in some cases, vibrational corrections.[28,33–35,52,55,94–96,136–138] As a result of this effort, the number of remaining discrepancies between theory and experiment for gas-phase measurements of optical rotation has been significantly reduced.[27,53,139]

However, the vast majority of experimental measurements of such properties are made in condensed phases, either in solvent or in the neat state, and attempts to simulate such environments accurately for chiroptical properties have seen only limited success. Continuum-based

solvent models,[140–143] for example, have been reported to reproduce experimental trends (as opposed to absolute values) only for those sytems in which electrostatic solute-solvent interactions are dominant.[52,95,137,144,145] However, in cases where molecule-specific interactions are significant, implicit solvent models are not reliable. Microsolvation studies by Xu and co-workers[146,147] on the paradigmatic chiral compound methyloxirane have revealed that both the magnitude and sign of the computed optical rotation can vary substantially depending on the number and configuration of solvent molecules in the region closest to the solute. In addition, combined molecular dynamics and density-functional studies by Beratan and co-workers[148,149] on the same compound in water and benzene have demonstrated that the solute can produce a surprisingly strong transfer of chirality to the solvent.

Clearly a careful accounting of explicit solute-solvent interactions — at least in the cybotactic region — is vital to the accurate simulation of the exquisitely sensitive chiroptical response. However, the cost of such calculations is prohibitively expensive at present. Given the high-degree polynomial scaling of conventional quantum chemical methods — $\mathcal{O}(N^3)$ for Kohn-Sham density functional theory (DFT)[150] and $\mathcal{O}(N^5)$ for coupled cluster theory[12,84] — inclusion of even a few water molecules, much less larger solvents such as benzene or cyclohexane, is far beyond the current state of the art. The cost of such computations is further exacerbated by the need to average properties of large numbers of snapshots of solute-solvent configurations along dynamical trajectories. While reduced- or even linear-scaling density functional and coupled cluster methods exist,[29,151–155] their prefactors — and thus their algorithmic crossover points — lie too far out in terms of system size for them to

provide any significant advantage for such computations.

One possible means of reducing the computational cost of explicit-solvation models is to apply a many-body expansion to the (relatively) weak interactions of the solute and solvent components. This approach involves decomposition of the total energy, E, of the complete solute-solvent system into N-body contributions, *viz.*

$$E = \sum_{I}^{N} E_I + \sum_{I<J}^{N} V_{IJ} + \sum_{I<J<K}^{N} V_{IJK} + \cdots \tag{5.1}$$

where

$$V_{IJ} = E_{IJ} - E_I - E_J \tag{5.2}$$

and

$$V_{IJK} = E_{IJK} - V_{IJ} - V_{IK} - V_{JK} - E_I - E_J - E_K, \tag{5.3}$$

etc. In the above equations, E_I is the energy of fragment/monomer I, E_{IJ} is the energy of the dimer composed of fragments I and J, etc. Thus, the $V_{IJ\ldots}$ represent N-body corrections, and truncation of the expansion at a particular term may yield a cost-effective approximation to a computation on the complete system, provided that the concomitant loss of accuracy is sufficiently small. Such expansions have been widely used in quantum chemistry for decades, and we particularly note numerous applications of such an approach to water and other molecular clusters.[156–161] Often the scheme is enhanced by embedding the cluster in an electrostic (or other simple) potential,[159,162] or making use of theory and/or basis-set hierarchies that treat higher-body terms using less expensive quantum chemical methods.[160,163] Furthermore, while most applications of Eq. (5.1) have focused on (inter-

action) energies, extensions to first-order properties such as dipole moments[159] and energy gradients[160] have also been recently reported. For the properties investigated thus far, the many-body expansion is found to converge rapidly, with truncation at three-body terms yielding small errors — often a fraction of a percent — relative to the much more expensive computation performed on the aggregate system.[159,160]

The goal of the present work is to examine the convergence of the many-body expansion for higher-order solute properties such as frequency-dependent dipole-polarizabilities and optical rotations. As test cases, we have chosen several small chiral compounds whose chiroptical response has been well studied, both in vapor and condensed phases. However, our purpose here is not to reproduce experimental measurements, but instead to determine if truncation of Eq. (5.1) is still effective for properties that are much more sensitive to the quality of the wave function than are energies or first derivatives.

5.1.2 Computational Details

The molecular dynamics program Gromacs[164] was used to place each of the four test solutes — (*S*)-methyloxirane, (*S*)-methylthiirane, (*S*)-2-chloropropionitrile, and (*M*)-dimethylallene— in a fixed configuration of water molecules. From these snapshots only those solvent molecules lying completely within a sphere of radius of 5.5 Ångstroms from the solute's geometric center were retained, yielding clusters of six or seven water molecules surrounding the solute. (See the supporting information for coordinates of each cluster.) For each test case,

interaction energies, dipole moments, dipole polarizabilities, and specific optical rotations were computed using the many-body expansion of Eq. (5.1).

The specific rotation of a chiral compound may be computed using the Rosenfeld optical activity tensor,[5,6]

$$\mathbf{G}'(\omega) = -\frac{2\omega}{\hbar} \sum_{j \neq 0} \frac{\mathrm{Im}(\langle \psi_0 | \boldsymbol{\mu} | \psi_j \rangle \langle \psi_j | \mathbf{m} | \psi_0 \rangle)}{\omega_{j0}^2 - \omega^2}, \tag{5.4}$$

where $\boldsymbol{\mu}$ and $\mathbf{m}$ are the electric- and magnetic-dipole operators, respectively, and ω is the frequency of plane-polarized light. The summation in Eq. (5.4) runs over the excited electronic (unperturbed) wave functions, ψ_j, each associated with an excitation frequency, ω_{j0}. The Rosenfeld tensor was computed at four wavelengths — 355, 436, 589, and 633 nm — using time-dependent density functional theory (TD-DFT) with the B3LYP[41,42] functional in Gaussian 09.[165] Gauge-including atomic orbitals (GIAOs)[46,47] were employed with the length representation of the electric dipole operator to ensure origin independence of the computed rotations. All computations were performed with the aug-cc-pVDZ basis set of Dunning and co-workers based on previous studies of its efficacy, especially for DFT.[14,135]

The specific rotation is related to the trace of the $\mathbf{G}'$ tensor,[8]

$$[\alpha]_\omega = \frac{(72.0 \times 10^6)\, \hbar^2 N_A \omega}{c^2 m_e^2 M} \times \left[\frac{1}{3}\mathrm{Tr}(\mathbf{G}')\right] \tag{5.5}$$

where $\mathbf{G}'$ and ω are given in atomic units, N_A is Avogadro's number, c is the speed of light (m/s), m_e is the electron rest mass (kg), and M is the molecular mass (amu). In order to obtain the specific rotation of the solute within the solvent cluster, the many-body expansion of Eq. (5.1) was used to obtain the $\mathbf{G}'$ tensor for the complete solute-solvent system at a

selected truncation level. The coordinate system of the full molecular cluster was held fixed for all fragment computations to ensure that the separate tensors could be combined. The final specific rotation was obtained from this composite $\mathbf{G}'$ tensor, with the mass M taken to be only that of the solute.

In order to automate use of the many-body expansion of Eq. (5.1), a local version of the PSI4[166] program was modified to generate separate calculations automatically for all required fragment combinations based on a master input file containing the coordinates of the complete solvent-solute system. The individual fragment computations can then be carried out independently and in parallel fashion. The Python front end of PSI4 was modified to monitor the status of these automatically generated jobs, compiling the results as the various tasks complete. When all data required for a particular truncation level have been collected, the corrections are automatically computed by Python functions tied into the PSI4 driver. Furthermore, these functions are completely general, enabling easy extension to other properties of interest or higher levels of theory or approximation.

5.1.3 Results and Discussion

(*S*)-2-chloropropionitrile

The interaction energy of (*S*)-2-chloropropionitrile (Table 5.1) with seven water molecules in a configuration extracted from a molecular dynamics simulation is well represented by the truncated many-body expansion of Eq. (5.1). Limiting the expansion to only two-

Table 5.1: Absolute percent errors for (*S*)-2-chloropropionitrile in a cluster of water molecules relative to the full eight-body calculation.

N-Body Truncation	Interaction Energy	Dipole Moment	Polarizability (633 nm)	Specific Rotation (633 nm)
1	--	8.46	2.47	106.66
2	11.75	2.55	2.90	26.91
3	1.06	0.11	0.34	13.05
4	0.10	0.01	0.41	13.27
5	0.15	0.01	0.30	4.18
6	0.07	0.01	0.06	1.88
7	0.02	0.00	0.01	0.80

body terms yields an error of nearly 12% as compared to a computation on the full cluster. However, extension to three-body contributions reduces the error to ca. 1%, and four-body terms are accurate to 0.10%, comparable to the convergence observed for water clusters by Tschumper.[167]

For dipole moments, the convergence of the many-body expansion is somewhat faster, with two-body truncation yielding percent errors of less than 3% relative to the full cluster. Three-body truncation of the dipole moment is accurate to within 0.11%, and higher-order terms are essentially negligible. These results for dipole moments are consistent with trends observed by Truhlar and co-workers[159] for dipole moments of chloride or hydrogen fluoride in aqueous solution, as well as for pure hydrogen fluoride clusters. For solvated chloride, for example, they observed errors of under 3% at the two-body truncation (referred to as pairwise additive in Ref. 159) without employing electrostatic embedding.

The convergence of the expansion for frequency-dependent polarizabilities (evaluated at 633 nm) starts even better than interaction energies and dipole moments, with a simple sum

of monomer polarizabilities giving an error of only 2.5%. However, extension of the sum to pairwise contributions actually increases the error slightly to ca. 3%. While three-body components quickly reduce the error to under 0.5%, subsequent corrections are somewhat larger than observed for interaction energies and dipole moments.

Experimental and computational studies of the chiroptical properties of (*S*)-2-chloropropionitrile have been reported before by Wiberg *et al.*[133] and by Kowalczyk *et al.*[36] The latter reported modest basis-set dependence of both DFT (B3LYP) and coupled cluster methods. The specific rotation of the (*S*)-2-chloropropionitrile plus water cluster is found to be significantly larger and of opposite sign than that of the isolated solute molecule (+156.4 deg dm^{-1} (g/mL)$^{-1}$ vs. -12.3 deg dm^{-1} (g/mL)$^{-1}$ at 633 nm; see Ref. 36). Although the cluster is not energetically optimum, the large perturbation introduced by the solvent cage is additional evidence of the importance of molecule-specific interactions on this property.

Unfortunately, convergence of the specific rotation of the solvated chloropropionitrile with many-body contribution (Table 5.2) is substantially slower than observed for the other properties. Employing solely monomers yields the incorrect sign of the rotation (*e.g.*, -10.4 deg dm^{-1} (g/mL)$^{-1}$ vs. +156.4 deg dm^{-1} (g/mL)$^{-1}$ at 633 nm). Incorporation of dimers in the expansion produces a qualitatively correct specific rotation, but with a quantitative error of 27-33% for the wavelengths considered here. Extension to trimers cuts this error roughly in half, with the computed rotations still smaller in magnitude than those obtained for the full cluster. However, inclusion of four-body terms overshoots the correct value yielding the same percent error of approximately 13%. Only when five-body terms are employed does

the error finally decrease to under 5% for the specific rotation, and then to under 2% at the six-body truncation.

Table 5.2: Specific rotations (deg dm^{-1} $(g/mL)^{-1}$) and absolute percent errors (APE) relative to the full eight-body calculation for (*S*)-2-chloropropionitrile in water.

N-body	355 nm		436 nm		589 nm		633 nm	
Truncation	$[\alpha]_\omega$	APE	$[\alpha]_\omega$	APE	$[\alpha]_\omega$	APE	$[\alpha]_\omega$	APE
1	−52.4	109.23	−27.5	107.88	−12.4	106.81	−10.4	106.66
2	380.6	32.95	246.2	29.35	132.4	27.22	114.3	26.91
3	488.6	13.92	302.2	13.29	158.0	13.19	136.0	13.05
4	642.8	13.24	394.4	13.15	206.2	13.31	177.1	13.27
5	547.4	3.55	336.1	3.58	174.8	3.96	149.9	4.18
6	577.2	1.70	355.1	1.88	184.5	1.41	159.3	1.88
7	572.2	0.81	351.4	0.82	183.7	0.95	157.6	0.80
8	567.6	--	348.5	--	182.0	--	156.4	--

Table 5.3: Absolute percent errors for (*S*)-methyloxirane in a cluster of water molecules relative to the full eight-body calculation.

N-Body Truncation	Interaction Energy	Dipole Moment	Polarizability (633 nm)	Specific Rotation (633 nm)
1	--	12.34	2.06	69.88
2	6.57	1.80	2.94	19.35
3	0.09	0.22	0.24	0.36
4	0.14	0.09	0.60	7.52
5	0.07	0.04	0.52	3.81
6	0.05	0.01	0.18	1.12
7	0.01	0.00	0.00	0.00

(*S*)-methyloxirane

The many-body expansion converges for the interaction energy of (*S*)-methyloxirane (Table 5.3) with a surrounding cluster of water molecules slightly faster than for (*S*)-2-chloropropionitrile, with the pairwise truncation of Eq. (5.1) giving an error of less than 7%, as shown in Table 5.3. The errors are slightly oscillatory for (*S*)-methyloxirane, however, with that arising from the four-body expansion (0.14%) slightly higher than than from the three-body components (0.09%). Nevertheless, the errors beyond trimers are negligible for the interaction energy.

The dipole moment of the (*S*)-methyloxirane plus water cluster requires dimers to reproduce that of the full cluster to within 2%, and, unlike the interaction energy, the errors decay smoothly with the many-body expansion. In addition, just as for (*S*)-2-chloropropionitrile, the 633 nm dipole polarizability of (*S*)-methyloxirane converges more slowly than either the dipole moment or interaction energy expansions, and it exhibits an oscillatory pattern similar to that observed for the interaction energy.

(*S*)-methyloxirane has long served as a challenging test case for quantum chemical models of optical activity.[33,34,52,148,149,168] Its vapor-phase specific rotation is small and bisignate ($+7.49 \pm 0.30$ deg dm^{-1} (g/mL)$^{-1}$ at 355 nm and -8.39 ± 0.20 deg dm^{-1} (g/mL)$^{-1}$ at 633 nm; see Ref. 25) and thus exceedingly sensitive not only to the choice of theoretical method and basis set, but also to the inclusion of molecular vibrational corrections, which were found to be necessary to reproduce experimental results. In addition, the optical activity of (*S*)-methyloxirane exhibits strong solvent dependence, such that even the sign of its liquid-phase specific rotation varies with the choice of solvent.[51]

Like its (*S*)-2-chloropropionitrile counterpart, the specific rotation of (*S*)-methyloxirane contained within a cluster of seven water molecules (270.7 deg dm^{-1} (g/mL)$^{-1}$ at 633 nm) is larger than that of the isolated molecule. Furthermore, the rotation is monosignate (positive) at all wavelengths down to 355 nm, unlike the gas-phase property. The specific rotation of (*S*)-methyloxirane converges much more slowly in the many-body expansion (Table 5.4) than the other properties considered here, though the convergence is slightly better relative to (*S*)-2-chloropropionitrile. Monomer, dimer, and trimer truncations approach the full value from below with the last yielding a fortuitously small error (as small as 0.08% at 589 nm). However, like (*S*)-2-chloropropionitrile, the series is not converged at this point: the four-body truncation overshoots and the error increases to 5-8%, depending on the wavelength. Expansion to six-body terms is necessary to converge the error relative to the full cluster down to around 1%.

Table 5.4: Specific rotations (deg dm^{-1} (g/mL)$^{-1}$) and absolute percent errors (APE) relative to the full eight-body calculation for (*S*)-methyloxirane in water.

N-body	355 nm		436 nm		589 nm		633 nm	
Truncation	$[\alpha]_\omega$	APE	$[\alpha]_\omega$	APE	$[\alpha]_\omega$	APE	$[\alpha]_\omega$	APE
1	408.3	65.08	215.0	67.42	97.1	69.55	81.5	69.88
2	928.0	20.63	528.6	19.89	256.9	19.44	218.3	19.35
3	1185.3	1.38	666.6	1.02	318.6	0.08	269.7	0.36
4	1235.2	5.65	696.7	5.59	340.0	6.65	291.0	7.52
5	1156.0	1.12	647.4	1.89	311.0	2.47	260.4	3.81
6	1163.6	0.48	662.5	0.40	318.4	0.14	273.7	1.12
7	1174.7	0.48	661.0	0.18	320.4	0.48	270.7	0.00
8	1169.1	--	659.8	--	318.8	--	270.7	--

(*M*)-dimethylallene

The convergence of the many-body expansion for the interaction energy, dipole moment, and dipole polarizability of (*M*)-dimethylallene in a cluster of water molecules (Figures 5.1 and 5.2; Table 5.5) is very similar to that observed for (*S*)-2-chloropropionitrile and (*S*)-methyloxirane. Indeed, for all three properties, the series converges slightly faster, and the three-body truncation already provides errors of less than 1% as compared to the full cluster. The series oscillates only slightly for the interaction energy and polarizability with a slight increase in the error between three- and four-body contributions, but the errors remain small enough to be negligible.

(*M*)-dimethylallene is unique among the chiral molecules considered here in that it exhibits a sterogenic axis rather than a stereogenic center. Its specific rotation was the subject of a detailed investigation in 2008 by Wiberg *et al.*[134] who reported a surprisingly large difference between its measured values in the neat liquid and vapor. At long wavelengths (633 and 589

Figure 5.1: Absolute percent error in the interaction energy, dipole moment, polarizability (355 nm), and optical rotation (355 nm) for (*M*)-dimethylallene solvated by seven water molecules as a function of *n*-body approximation level. The monomer approximation is excluded due to its large error.

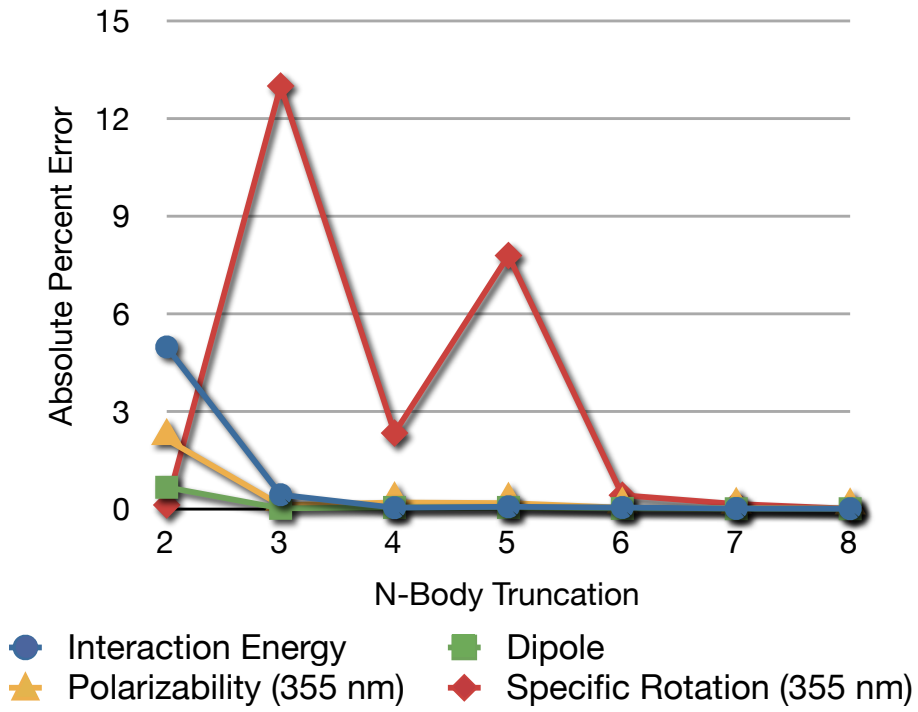

nm), the specific rotation of the isolated molecule (-108.4 and -125.1 deg dm^{-1} $(g/mL)^{-1}$; see Ref. 134) is approximately the same as that of the solute plus water snapshot extracted from the dynamical simulation. For the shorter wavelengths, however, the rotation is much larger for the cluster, suggesting that the lowest excited state shifts to lower energy due to the interaction with the nearby water molecules.

The specific rotation of (*M*)-dimethylallene, on the other hand, converges more slowly than either (*S*)-2-chloropropionitrile or (*S*)-methyloxirane, though the qualitative behavior is essentially the same (Table 5.6). At long wavelengths, the specific rotation of the cluster is

Table 5.5: Absolute percent errors for (*M*)-dimethylallene in a cluster of water molecules relative to the full eight-body calculation.

N-Body Truncation	Interaction Energy	Dipole Moment	Polarizability (355 nm)	Specific Rotation (355 nm)
1	--	11.27	2.68	75.66
2	4.97	0.66	2.13	0.12
3	0.43	0.01	0.11	12.99
4	0.03	0.04	0.19	2.33
5	0.06	0.04	0.17	7.78
6	0.04	0.01	0.03	0.42
7	0.01	0.00	0.02	0.15

approached from below (*i.e.*, from more negative values), with increasing many-body truncation, and the four-body expansion overshoots as before. The behavior is somewhat different at shorter wavelengths, however, with the many-body expansion approaching the full value from above and exhibiting greater oscillation. This is a result of the fact that the Rosenfeld tensor diverges in the vicinity of a resonance, and the lowest excitation energy is clearly also sensitive to the truncation of the series. In the case of (*M*)-dimethylallene, errors as large as 20% (corresponding to -21 deg dm^{-1} $(g/mL)^{-1}$ at 633 nm) remain even at the five-body truncation level.

Figure 5.2: (*M*)-dimethylallene solvated by seven water molecules within a 5.5 Å radius of the solute's geometric center.

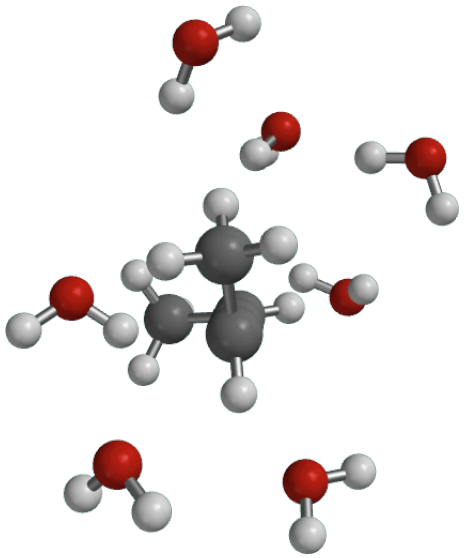

Table 5.6: Specific rotations (deg dm^{-1} (g/mL)$^{-1}$) and absolute percent errors (APE) relative to the full eight-body calculation for (*M*)-dimethylallene in water.

N-body	355 nm		436 nm		589 nm		633 nm	
Truncation	$[\alpha]_\omega$	APE	$[\alpha]_\omega$	APE	$[\alpha]_\omega$	APE	$[\alpha]_\omega$	APE
1	−190.5	75.66	−253.6	25.53	−163.9	23.65	−143.8	32.16
2	−783.4	0.12	−422.7	24.15	−187.6	41.56	−157.0	44.33
3	−884.1	12.99	−394.8	15.96	−156.6	18.17	−129.6	19.15
4	−800.7	2.33	−323.2	5.09	−123.7	6.67	−99.9	8.16
5	−843.4	7.78	−392.6	15.31	−155.5	17.28	−129.8	19.27
6	−785.7	0.42	−334.2	1.86	−133.4	0.67	−108.9	0.13
7	−781.4	0.15	−341.6	0.32	−131.9	0.52	−108.2	0.55
8	−782.5	--	−340.5	--	−132.5	--	−108.8	--

Table 5.7: Absolute percent errors for (*S*)-methylthiirane in a cluster of water molecules relative to the full seven-body calculation.

N-Body Truncation	Interaction Energy	Dipole Moment	Polarizability (589 nm)	Specific Rotation (589 nm)
1	--	11.51	3.37	797.96
2	8.31	1.68	1.98	2028.61
3	0.37	0.08	0.36	393.10
4	0.10	0.01	0.07	119.60
5	0.03	0.00	0.02	20.76
6	0.01	0.00	0.01	26.76

(*S*)-methylthiirane

The many-body expansion for the interaction energy, dipole moment, and dipole polarizability of (*S*)-methylthiirane in a cluster of six water molecules (Table 5.7) converges more smoothly than for (*S*)-methyloxirane and (*M*)-dimethylallene, with no oscillation apparent with increasing truncation level. The specific rotation of (*S*)-methylthiirane plus water, on the other hand, is much more difficult to model accurately. Vapor-phase specific rotations were measured in 2005 by Wilson *et al.*[25] who reported $+36.5\pm1.7$ deg dm^{-1} (g/mL)$^{-1}$ at 633 nm and $+64.7\pm2.3$ deg dm^{-1} (g/mL)$^{-1}$ at 355 nm for the (*R*) enantiomer. Crawford, Tam, and Abrams[35] reported DFT and coupled cluster specific rotations as well as electronic circular dichroism spectra for (*S*)-methylthiirane in 2007 and found that vibrational corrections were necessary to produce reasonable comparison with experiment in the long wavelength regime, but the same corrections distorted the comparison for shorter wavelengths.

The specific rotation of (*S*)-methylthiirane in the cluster of six water molecules (Table 5.8) modeled here is bisignate, with a strong positive Cotton pole as the wavelength of the

Table 5.8: Specific rotations (deg dm^{-1} (g/mL)$^{-1}$) and absolute percent errors (APE) relative to the full seven-body calculation for (*S*)-methylthiirane in water.

N-body	355 nm		436 nm		589 nm		633 nm	
Truncation	$[\alpha]_\omega$	APE	$[\alpha]_\omega$	APE	$[\alpha]_\omega$	APE	$[\alpha]_\omega$	APE
1	74.0	41.23	−50.7	464.48	−47.3	797.96	−42.5	647.85
2	665.2	428.46	262.0	1785.14	101.5	2028.61	83.9	1574.83
3	1.1	99.12	−35.7	356.77	−26.0	393.10	−23.1	306.56
4	138.4	9.93	7.5	45.71	−11.6	119.60	−10.9	91.30
5	114.4	9.10	14.2	1.83	−4.2	20.76	−4.8	15.05
6	125.5	0.30	12.4	11.11	−6.7	26.76	−6.7	17.24
7	125.9	--	13.9	--	−5.3	--	−5.7	--

polarized field becomes shorter. The specific rotation of the isolated molecule,[35] however, is monosignate according to both experiment and coupled cluster theory, though the B3LYP functional finds a bisginate dispersion due to its underestimation of the energy of lowest excited state. The convergence of the many-body expansion of the specific rotation of the (*S*)-methylthiirane plus water cluster is more erratic than that of the other species investigated here. At 633 nm, for example, the rotation shifts from −42.5 deg dm^{-1} (g/mL)$^{-1}$ using only monomers to +83.9 deg dm^{-1} (g/mL)$^{-1}$ using dimers, and then back to −23.1 deg dm^{-1} (g/mL)$^{-1}$ with trimers. At 355 nm, on the other hand, the variation is even more pronounced (though without concomitant sign changes), with a one-body truncation of +74.0 deg dm^{-1} (g/mL)$^{-1}$, two-body truncation of +665.2 deg dm^{-1} (g/mL)$^{-1}$, three-body +1.1 deg dm^{-1} (g/mL)$^{-1}$, and four-body +138.4 deg dm^{-1} (g/mL)$^{-1}$, before the series finally begins to approach the untruncated result. The relatively small total rotations at long wavelengths produce very large corresponding percent errors — more than 2000% for the pairwise expansion at 589 nm, for example.

5.1.4 Conclusions

When describing the interations between solute and solvent, the venerable many-body expansion converges rapidly and smoothly for energies, dipole moments, and dipole polarizabilities — that is, properties that are strongly localized and/or easily partitioned into local contributions. On the other hand, for properties such as optical rotations, whose values (both magnitude and sign) depend strongly on more distant interactions, Eq. (5.1) converges much more slowly. We have demonstrated that for four paradigmatic chiral compounds — (*S*)-methyloxirane, (*S*)-methylthiirane, (*S*)-2-chloropropionitrile, and (*M*)-dimethylallene— each contained in a small cluster of water molecules, the expansion is highly oscillatory and erratically convergent. Admittedly, the appearance of (relatively) strong hydrogen bonding interactions between the solute and solvent (and between solvent molecules themselves) makes the choice of water a worst-case scenario, and Eq. (5.1) may exhibit better behavior for more weakly interacting solvents such as cyclohexane. However, even in such cases, the transfer of chirality from the solute to the solvent (*e.g.* through the chiral hole analyzed by Beratan and co-workers[149]) yields widely disparate optical rotations among the various *N*-body fragments. As a result, the many-body expansion will still be exceedingly sensitive to truncation.

It may be possible to relieve at least some of the computational burden of explicit solvation models through, *e.g.*, multi-theory QM/MM schemes[160,162,169] or distance-based criteria to eliminate minor contributions to the many-body expansion.[170] However, the non-locality of chiroptical properties on which such schemes rely is still poorly understood. This work sug-

gests that the "chiral imprint" onto the solvent extends sufficiently far out from the solute as to require models of condensed phase dynamics that are much more robust — and potentially much more costly — than previously hoped. This is particularly discouraging considering the large number of molecular dynamics snapshots that must be averaged in the case of optical rotation to achieve a balanced representation of the opposing sign contributions from different molecular configurations.[171]

5.2 Improving N-Body Optical Rotations

The study in the previous section was an initial test of the quality of optical rotations computed using an N-body approach. In contrast to the success reported in the literature for properties such as interaction energies, dipole moments, and polarizabilities, the many-body expansion does not perform well for optical rotation. The expansion is not smoothly or monotonically convergent and must be truncated at much higher orders to achieve percent errors in the single digits. The oscillatory behavior of the optical rotation absolute percent error, along with significantly increased computational cost, appears to suggest that the many-body expansion is less useful for such higher order properties. However, the potential utility of such an approach to extend the calculation of optical rotation into the condensed phase warrants further testing and the pursuit of a robust N-body methodology for optical rotation. From the myriad remaining questions we have chosen three upon which to focus our attention: the effects of basis set quality, the many-body expansion's performance on larger molecular clusters, and the errors due to numerical accuracy of the individual component calculations.

5.2.1 Basis Set Effects

As seen in Chapter 3, the optical rotation of many systems has a high dependence on basis set quality, even occasionally changing sign with increasing basis size (Table 3.7). The aug-cc-pVDZ basis utilized in the previous study has been shown in the case of isolated molecules

Table 5.9: Basis set dependence of various properties of (*S*)-methyloxirane in a cluster of water molecules.

Property	aDZ	daDZ	aTZ
Interaction Energy (Hartrees)	0.0238	0.0234	0.0286
Dipole Moment (Debye)	9.04	9.03	9.04
Polarizability (Bohr^3) [633 nm]	110.91	111.97	111.51
Optical Rotation (deg dm^{-1} (g/mL)$^{-1}$) [633 nm]	270.69	287.93	281.94

to provide a balance of computational cost and optical rotation accuracy.[23] However, intermolecular interactions may increase the basis set demands for computing the optical rotation of molecular clusters. In addition, the nature of the *N*-body approximation and the associated additive corrections may also increase the basis set demands. Results for interaction energies, dipole moments, polarizabilities, and optical rotations computed in the d-aug-cc-pVDZ and aug-cc-pVTZ basis sets are shown alongside those of aug-cc-pVDZ in Table 5.9 for (*S*)-methyloxirane surrounded by seven water molecules.

The changes in the dipole moment and polarizability of the cluster are negligible at less than one percent and the interaction energy changes by roughly twenty percent when going to the aug-cc-pVTZ basis. The changes in the optical rotation fall between those of the interaction energy and the other two properties. The less than ten percent change hardly warrants the use of a basis larger than aug-cc-pVDZ for computing the optical rotation of the entire molecular cluster. However, the changes to the progression of the many-body expansion are more interesting. The aug-cc-pVDZ optical rotations (Table 3.1) show a slight hiccup at the four-body level with the error increasing from the three-body error of less than one percent to over seven percent. Increasing the basis to d-aug-cc-pVDZ (Table 5.10) exacerbates this

Table 5.10: Absolute percent errors for (*S*)-methyloxirane in a cluster of water molecules relative to the full eight-body calculation (d-aug-cc-pVDZ basis).

N-Body Truncation	Interaction Energy	Dipole Moment	Polarizability (633 nm)	Specific Rotation (633 nm)
1	--	12.33	1.23	70.73
2	8.36	1.23	0.81	5.55
3	0.89	0.20	0.20	31.00
4	3.48	0.13	0.35	57.25
5	3.51	0.06	0.38	83.48
6	1.65	0.03	0.26	21.82
7	0.15	0.01	0.08	39.61

behavior, creating much larger peaks in the error at the five-body truncation (83.48 percent error) and again at the seven-body level (39.61 percent error). The drastic nature of these oscillations is seen most clearly in Figure 5.3 where the performance of the aug-cc-pVDZ and d-aug-cc-pVDZ bases are plotted side by side. The dipole moment and polarizability performance remain stable, but the interaction energy performance decreases exhibiting an error increase from 0.89 percent error at the three-body approximation to approximately 3.5 percent error at both the four- and five-body levels.

The poor performance of the d-aug-cc-pVDZ basis is the result of basis set superposition error. Utilizing sub-clusters (monomers, dimers, etc.) computed in their own basis for the *N*-body corrections that approximate the properties of the cluster in its full basis is unbalanced. The additional diffuse functions in the d-aug-cc-pVDZ basis exaggerate the effects of this imbalance on the optical rotation causing the approximation at each subsequent truncation level to change wildly. We can see this is clearly the case by comparing the errors of the standard d-aug-cc-pVDZ *N*-body progression with that of an *N*-body expansion where all

Figure 5.3: Comparison of aug-cc-pVDZ (triangles) and d-aug-cc-pVDZ (circles) optical rotation absolute percent errors for (*S*)-methyloxirane solvated by seven water molecules as a function of *n*-body truncation level.

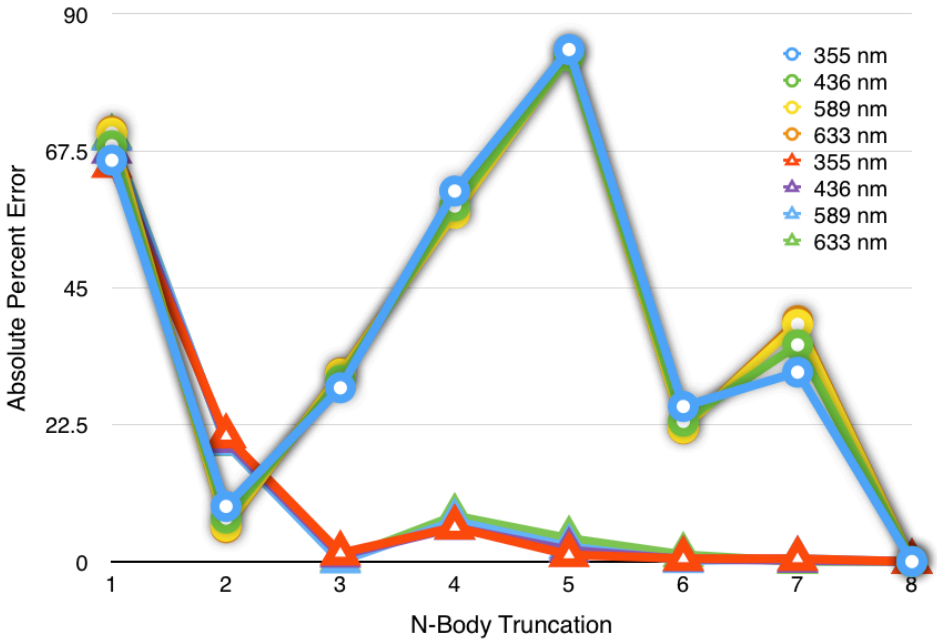

systems have been computed in the "cluster basis" (Table 5.11), that is all basis functions present on the entire cluster, not just the currently active fragment(s). The erratic nature of the optical rotation error disappears entirely, and the second maximum for the interaction energy no longer exists.

Admittedly the (*S*)-methyloxirane results are a best case scenario as the erratic behavior in the data for other molecules, namely (*M*)-dimethylallene (the worst case scenario from earlier), does not smooth out entirely in the cluster basis as seen in Table 5.12. However, the errors are reduced substantially at all levels of truncation, and with the exception of the 355 nm rotations there are no increases in error larger than 0.5 percent after the two-body approximation. Findings discussed in the upcoming subsections also show basis set incom-

Table 5.11: Absolute percent errors for (*S*)-methyloxirane in a cluster of water molecules relative to the full eight-body calculation (d-aug-cc-pVDZ basis). All calculations are done with all basis functions for the entire cluster present, the "cluster basis".

N-Body Truncation	Interaction Energy	Dipole Moment	Polarizability (633 nm)	Specific Rotation (633 nm)
1	--	12.36	1.40	68.63
2	5.18	1.40	0.67	28.45
3	0.12	0.01	0.17	8.72
4	0.01	0.01	0.29	6.12
5	0.01	0.04	0.27	2.46
6	0.00	0.02	0.13	0.44
7	0.00	0.01	0.05	0.22

Table 5.12: Specific rotations (deg dm^{-1} $(g/mL)^{-1}$) and absolute percent errors (APE) computed in the cluster basis relative to the full eight-body calculation for (*M*)-dimethylallene in water.

N-body	355 nm		436 nm		589 nm		633 nm	
Truncation	$[\alpha]_\omega$	APE	$[\alpha]_\omega$	APE	$[\alpha]_\omega$	APE	$[\alpha]_\omega$	APE
1	−123.6	84.20	−216.7	36.35	−146.8	10.72	−129.4	18.94
2	−746.9	4.54	−389.7	14.45	−167.3	26.20	−138.4	27.18
3	−771.8	1.37	−330.6	2.92	−122.6	7.47	−103.5	4.82
4	−851.3	8.80	−353.0	3.69	−137.3	3.60	−105.6	2.89
5	−751.1	4.01	−326.5	4.12	−127.1	4.11	−110.8	1.86
6	−790.6	1.03	−351.7	3.30	−135.2	2.04	−108.5	0.24
7	−783.7	0.15	−336.1	1.28	−132.3	0.17	−108.4	0.36
8	−782.5	--	−340.5	--	−132.5	--	−108.8	--

pleteness error playing a large role in undesirable error increases with increasing truncation level.

5.2.2 Larger Solvation Shell

All clusters mentioned thus far were created by including only those solvent molecules that are within 5.5 Å of the solute molecule. The resulting systems include at most eight molecules, and the tests of the many-body expansion reveal that five- or six-body contri-

butions are often necessary to attain sufficient accuracy for optical rotations. In an effort to determine whether these contributions are generally necessary or suffice only for small systems whose physics are encapsulated at this level of interaction, we have enlarged the radius yielding a system that increases the number of included solvent molecules to 13, nearly double that of the previous systems. (*S*)-methyloxirane has been used as the solute because it is the most highly tested of the smaller systems. Table 5.13 shows results for the standard *N*-body approach using the aug-cc-pVDZ basis. The dipole moment results are of similar accuracy as those for the eight-body system starting at an error of 14.86 percent at the monomer approximation and decaying to less than 1 percent error by the three-body truncation. The polarizability data initially appears to also be of similar quality with the monomer approximation giving lower error than that of the dipole moment at 2.28 percent. It then exhibits the characteristic increase upon inclusion of pair interactions, but decreases until the five-body level where it nearly doubles to 7.29 percent error. Increasing the *N*-body level further increases the error reaching a maximum error of 17.30 percent at the eight-body level. The one percent error threshold is only reached at the 13-body level. The optical rotation is also very similar starting out with a high error of 59.09 percent at the monomer approximation, as is typical. This error decreases rapidly crossing the one percent threshold at the four-body level. However, as was the case with the polarizability, examining higher *n*-body contributions reveals increases in the error which only drop below 10 percent at the 12-body level. Especially of note is the error trend for the interaction energy. The four-body error is slightly over one percent leading one to believe that the five-body level

Table 5.13: Absolute percent errors for (*S*)-methyloxirane in a cluster of water molecules relative to the full fourteen-body calculation.

N-Body Truncation	Interaction Energy	Dipole Moment	Polarizability (633 nm)	Specific Rotation (633 nm)
1	--	14.86	2.28	59.09
2	8.89	2.99	6.39	20.06
3	5.77	0.52	3.73	5.53
4	1.07	0.44	3.79	0.76
5	10.50	0.55	7.29	26.45
6	14.28	0.66	12.50	29.06
7	10.90	0.54	16.50	10.25
8	5.00	0.38	17.30	56.02
9	1.35	0.21	14.41	67.77
10	0.22	0.19	9.44	50.65
11	0.06	0.11	4.61	26.17
12	0.02	0.04	1.50	8.81
13	0.01	0.01	0.24	1.40

should be sufficient for this system. This seems reasonable, as the *N*-body expansion performed admirably for the previous systems needing the three-body truncation at most, and this system is larger and has more complicated interactions requiring the inclusion of four- or five-body interactions. However, the five-body error jumps up to over 10 percent where it stays until the eight-body level, finally dropping below one percent at 10-body. To our knowledge a failure of the many-body expansion for interaction energies such as this has yet to be presented in the literature.

In the aug-cc-pVDZ basis the smaller (*S*)-methyloxirane system has an optical rotation error curve that was nearly monotonically decreasing but contained a slightly concerning second maximum at the four-body level of approximation. This second maximum disappeared when computing all corrections in the cluster basis. The number of sub-clusters grows factorially

Table 5.14: Absolute percent errors for (*S*)-methyloxirane in a cluster of water molecules relative to the full fourteen-body calculation (cluster basis).

N-Body Truncation	Interaction Energy
1	--
2	3.75
3	3.31
4	1.87
5	1.09
6	0.99

with system size, thus computing the full progression for this larger system requires 16,383 separate computations compared to the 255 for the smaller system. The sheer number of calculations coupled with the increase in expense due to larger sub-cluster computations makes computing the full progression for the 14-body cluster in the cluster basis impractical. However, we have studied the interaction energy through truncation at the six-body level (Table 5.14) and find that the error decreases at each subsequent level being just over one percent error at the five-body level and dropping slightly under with the addition of six-body contributions. The resolution of this unprecedented interaction energy error makes us highly confident that computing in the cluster basis would eliminate the error increases in the polarizability and optical rotation as well.

5.2.3 Numerical Accuracy

All the *N*-body data discussed thus far has been calculated with Gaussian09 using its default convergence criteria. Initially there was some question if the default criteria were tight

Table 5.15: Absolute percent errors of aug-cc-pVDZ specific rotations (deg dm^{-1} $(g/mL)^{-1}$) at 633 nm for (*S*)-methyloxirane in a cluster of seven water molecules relative to the full eight-body calculation. Columns containing data from calculations with the convergence criteria for the SCF and CPHF portions increased to 10^{-12} are denoted by (10^{-12}).

N-Body	B3LYP	B3LYP (10^{-12})	HF	HF (10^{-12})	B3LYP (Cluster Basis)
1	69.88	68.82	68.71	68.71	83.23
2	19.35	16.34	15.29	15.26	19.43
3	0.36	2.40	1.23	1.28	4.35
4	7.52	15.05	7.14	7.22	2.17
5	3.81	1.37	4.57	4.74	0.29
6	1.12	1.12	0.80	1.01	0.38
7	0.00	0.00	0.64	0.55	0.23

enough to allow computation of robust corrections and whether loose convergence might be a contributing factor in the error increases and secondary maximum seen in the (*S*)-methyloxirane eight fragment cluster. In addition, Gaussian09's density functional code uses integration grids to compute two-electron integrals which can also introduce numerical accuracy issues. The cluster basis results suggest that convergence issues are not the main problem, and the results in Table 5.15 confirm this.

The B3LYP results shown in the second column of Table 5.15 are the same percent errors as shown earlier for (*S*)-methyloxirane in the aug-cc-pVDZ basis. The adjacent column contains data for which the only alteration is the convergence criteria which has been increased in both the SCF and CPHF portions of the code to 10^{-12} and utilization of the UltraFine integration grid for both the integrals and CPHF portions of the calculation. The differences between the two columns is small in most cases and when it is large (four-body) the tighter convergence results are worse, exhibiting a secondary maximum that is almost exactly double that of the lower convergence.

To completely remove the impact of integration grids, Hartree-Fock calculations were also run (columns four and five) with default criteria and the 10^{-12} settings. In this case the data show extremely small changes with increase in convergence differing at most by 0.21 percent. The secondary maximum at four-body appears in both data sets and they reach the one percent error threshold at six-body truncation independent of the convergence criteria. For comparison purposes the percent errors for B3LYP calculations using the default convergence criteria computed in the cluster basis are shown in the final column of Table 5.15. The error decreases at each subsequent level of truncation and drops under the one percent error mark one level earlier at five-body.

5.2.4 Conclusions and Prospectus

The strong basis set dependence exhibited by traditional optical rotation calculations manifests itself within the many-body framework as a large basis set incompleteness error. This unequal treatment between levels of truncation in terms of basis contributes substantial error, in some cases making the true contributions of the sub-clusters at each level difficult to determine. Besides the enormous cost associated with performing all required calculations in the cluster basis, this inability to analyze each fragment's contribution to a particular level of truncation motivates the use of more balanced means of counterpoise correcting each term in the expansion. Richard *et al.* have adapted the standard Boys-Bernardi[172] counterpoise correction to the many-body expansion as well as the more computationally intensive (and thus less utilized) Valiron-Mayer[173] function counterpoise correction.[161,174] They have formulated

these corrections which they label MBCP(n) and VMFC(n) as a perturbative expansion that is truncated at the same order as that of the many-body expansion of the property to provide an appropriate level of basis set error correction. The standard counterpoise correction can be formulated as an additive correction, $\varepsilon_{\mathrm{CP}}$,

$$E^{\mathrm{CP}} = E^{IJK\cdots N}_{IJK\cdots N} + \varepsilon_{\mathrm{CP}} \tag{5.6}$$

where E^{CP} is the counterpoise corrected total energy and

$$\varepsilon_{\mathrm{CP}} = \sum_I E^I_I - \sum_{i=I\cdots N} E^{IJK\cdots N}_i. \tag{5.7}$$

In the above expressions the subscripts index the fragments, and the superscripts denote the basis in which the fragments are computed. In the case of MBCP(n) the counterpoise correction expands as

$$\begin{aligned}\varepsilon_{\mathrm{CP}} = \sum_I E^I_I - \Bigg(&\sum_I E^I_I + \sum_I \sum_{J\neq I} (E^{IJ}_I - E^I_I) \\ &+ \sum_I \sum_{J\neq I} \sum_{\substack{K>J \\ K\neq I}} [E^{IJK}_I - (E^{IJ}_I - E^J_I) - (E^{IK}_I - E^K_I) - E^I_I] + \cdots \Bigg)\end{aligned} \tag{5.8}$$

enabling the counterpoised corrected energy to be written

$$E^{\mathrm{CP}} = E^{IJK\cdots N}_{IJK\cdots N} + \varepsilon^{(1)}_{\mathrm{CP}} + \varepsilon^{(2)}_{\mathrm{CP}} + \varepsilon^{(3)}_{\mathrm{CP}} + \cdots \tag{5.9}$$

where

$$\varepsilon^{(1)}_{\mathrm{CP}} = 0 \tag{5.10}$$

$$\varepsilon^{(2)}_{\mathrm{CP}} = -\sum_I \sum_{J\neq I} (E^{IJ}_I - E^I_I) \tag{5.11}$$

and

$$\varepsilon_{\mathrm{CP}}^{(3)} = -\sum_{I}\sum_{J\neq I}\sum_{\substack{K>J\\K\neq I}}[E_I^{IJK} - (E_I^{IJ} - E_I^I) - (E_I^{IK} - E_I^I) - E_I^I]. \tag{5.12}$$

The VMFC(n) scheme works very similarly with the nature of the Valiron-Mayer counterpoise correction changing only the definitions of the components of $\varepsilon_{\mathrm{CP}}$ to be

$$\varepsilon_{\mathrm{CP}}^{(1)} = \sum_{I}(E_I^I - E_I^{IJK\cdots N}) \tag{5.13}$$

$$\varepsilon_{\mathrm{CP}}^{(2)} = \sum_{I<J}(V_{IJ}^{IJ} - V_{IJ}^{IJK\cdots N}) \tag{5.14}$$

and

$$\varepsilon_{\mathrm{CP}}^{(3)} = \sum_{I<J<K}(V_{IJK}^{IJK} - V_{IJK}^{IJK\cdots N}) \tag{5.15}$$

where

$$V_{IJ}^{IJ} = E_{IJ}^{IJ} - E_I^{IJ} - E_J^{IJ}. \tag{5.16}$$

In order to eliminate the terms involving the entire cluster basis the VMFC(n) expansion is simplified by retaining only those terms with basis functions on n monomers or less.

$$\varepsilon_{\mathrm{CP}}^{(1)} = \sum_{I} E_I^I \tag{5.17}$$

$$\varepsilon_{\mathrm{CP}}^{(2)} = \sum_{I<J} V_{IJ}^{IJ} \tag{5.18}$$

and

$$\varepsilon_{\mathrm{CP}}^{(3)} = \sum_{I<J<K} V_{IJK}^{IJK}. \tag{5.19}$$

Many-body expansion approximations to complete basis set limit extrapolations of MP2 and CCSD(T) energies have been dramatically improved by incorporation of the above corrections. It is our hope that they show similar performance in the case of optical rotation, enabling cluster basis level results while significantly reducing the computational cost.

5.3 PSI4's N-Body Implementation

The N-body work described above has all been completed using recently implemented capabilities of the PSI4[166] computational chemistry package. In version 4 of the PSI code the driver is written in Python enabling very flexible and easily extensible program execution. If the job requested by the user includes a 'n_body' dictionary in its options then the N-body routines are called in lieu of the routines required to perform the requested quantum chemical calculation. The N-body routines then create the necessary directories placing within them input files containing all appropriate molecular fragments to accomplish the calculation type requested in the master input file. Each of these individual jobs is completely independent of the others and can be run by the user as they see fit. Currently only energy and property calculations are implemented in the PSI4 driver, and as PSI4 is unable to calculate density functional theory response properties, if such a property is requested the input files for Gaussian09[165] are created.

When PSI4 is executed after input file generation, the status of each job is checked. This has three possible outcomes, first the job could be 'not_started' meaning there is no output file present for that job. If an output file is present the job is marked as 'running', and if that output file contains "PSI4 exiting successfully" or "Normal termination of Gaussian" the status is changed to 'complete'. This means that 'running' is technically a misnomer as it truly means that an incomplete output file exists, which is also the case when a job terminates prior to success. However, the ability to run jobs in parallel across a cluster and

the idiosyncrasies of individual clusters and their submission queues prevents the automated determination of job failure.

When all jobs of a particular n-body level have completed the output files are parsed for all available quantities of interest depending on the user-requested calculation. If data for all levels less than that n-body level are also available, the corrections (V's) are computed and printed to the output file in the top level directory. The correction calculation is done in a recursive manner that is independent of the identity of the property and thus is arbitrarily extendible to higher n-body levels or quantum chemical properties.

In order to make PSI4's N-body capabilities black box the tracking of input file generation, job status, and data processing are all done simply by running PSI4 in the master directory. No flags or modifications to the input files are required as all relevant data is tracked automatically through the use of a Python dictionary stored on disk using the `shelve` module. This persistent dictionary is created during the initial PSI4 execution using whichever of the four Python dictionary protocols is available on the system. It is then automatically accessed upon each subsequent run of PSI4 to determine which tasks to run. The contents and layout of the dictionary are as follows:

Database Entry	Type	Description
`'initialized'`	BOOLEAN	Tracks database initialization
`'inputs_generated'`	BOOLEAN	Tracks successful input generation
`'jobs_complete'`	BOOLEAN	Tracks successful completion of all jobs
`'options'`	DICTIONARY	Contains user specified N-body options
→`'n_body_func'`	FUNCTION	User requested job type (*e.g.* property)
→`'methods'`	LIST	Contains strings of all user requested methods
`method` (*e.g.* `'cc2'`)	DICTIONARY	Contains method dependent options
→`'n_body_max'`	INTEGER	User requested upper bound to N-body expansion
→`'results'`	LIST	Contains strings of computed quantities
→`'n_body_level` (*e.g.* `1`)	DICTIONARY	Contains job status and data for n_body_level n
→`'num_jobs_complete'`	INTEGER	Number of jobs that are complete for n
→`'total_num_jobs'`	INTEGER	Total number of jobs for n
→`result` (*e.g.* `'scf_energy'`)	DICTIONARY	Contains data for each computed quantity
→`'raw_data'`	DICTIONARY	Contains unprocessed output file data
→`'cooked_data'`	DICTIONARY	Contains processed data (*i.e.* individual many-body corrections)
→`'correction'`	FLOAT	Many-body correction for n (sum of the `'cooked_data'`)
→`result`	FLOAT	Value of the property at n (sum of all previous corrections)
→`'job_status'`	DICTIONARY	Contains `'started'`, `'running'`, or `'complete'` for each job in n

The dictionary structure above gives a glimpse into the internals of the N-body implementation, but it doesn't show the syntax and flexibility of user defined input. Below are a few examples of how N-body can be called in PSI4 and a short explanation of what each accomplishes.

```
energy('cc2', n_body = True)
```

Setting the n_body keyword to True makes the code assume that the name given (cc2) is the desired method and that input files for all possible n up to the total number of fragments specified in the input file should be generated. The generated input files will each call a CC2 energy calculation.

```
property('b3lyp', n_body = 4, properties=[rotation])
```

Again, the given name (b3lyp) is utilized but the many-body expansion is truncated at $n = 4$. Each input file will call a B3LYP optical rotation calculation, as mentioned since PSI4 does not currently have the capability to compute B3LYP optical rotations the generated input files will be for Gaussian09.

```
property('cc2', n_body = {'b3lyp':  5, 'cc2':  3, 'cutoff':  3.0},
properties=[polarizability])
```

In this case both the B3LYP and CC2 methods are desired by the user. N-body will create two directories, one for B3LYP and one for CC2 jobs and create inside each the necessary input files to compute many-body corrections up through $n = 5$ and $n = 3$ respectively. In addition, the user has requested that only those fragments that are within a distance of

3.0 Ångstroms of each other be included in the approximation of the polarizability. The dictionary is the only input method that allows access to advanced N-body options such as 'cutoff'. When options are specified in a dictionary, as above, the name is irrelevant and the method(s) desired must be specified inside the dictionary.

Chapter 6

Conclusion

The theoretical prediction of optical rotation holds tremendous promise for the chemical community as the relationship between an enantiomer and its rotation of plane polarized light is unique spectroscopically. This relationship enables identification of absolute configuration based on specific rotation, however, in order for this to be the case the rotation of at least one enantiomer must be known *a priori*. Similarly, knowing the spatial arrangement of chemical groups and features provides absolutely no information about the rotation that will be produced upon introduction of plane polarized light. Despite these shortcomings the ease with which the spectra can be interpreted due to the disparate nature of the two responses makes it an especially powerful technique.

The potential utility of a robust predictive model for computing optical rotation has created a highly active community of researchers working to advance the state-of-the-art calculation

of optical rotation. These efforts have revealed that large one-electron basis sets (including diffuse functions)[14,23,28,36,135] and high levels of electron correlation[24,33,34,52,95] are required. In some systems even considerations of molecular motion through inclusion of vibrational corrections is needed to achieve agreement with experiment.[28,33–35,52,55,94–96,136–138] These necessary lengths have prevented truly predictive calculations of optical rotation from becoming commonplace despite the technical requirements for the gas phase being well understood. Basis sets for calculation of electrical properties and optical rotation specifically have been created in an effort to ease the cost of large basis sets. While the LPol[31] and ORP[61] basis sets perform as well or better than comparably sized general basis sets,[14,30] as shown in Chapter 3 they are no silver bullet. Further reductions in cost will be necessary for predictive calculation of optical rotation to become mainstream, for which algorithmic improvements such as utilization of a local treatment of electron correlation hold promise in terms of CC response properties.[29,155]

In addition to reducing the requirements stated above for calculation of gas phase optical rotation, computational predictions will have to reliably enter into the condensed phase, where the majority of experimental measurements are made, to become a tool routinely used by chemists. Perturbational expansions, such as the N-body work presented in Chapter 5, encompass initial endeavors into calculations of individual solute molecules which include explicit solvent molecules. The performance of such methods are in line with what perhaps should be expected based on the challenges of obtaining sufficient accuracy in the gas phase, that is the optical rotation of a non-bonded cluster is much harder to get right than its

interaction energy, dipole moment, or even polarizability. Initial basis set completeness corrections show promise; however, it is highly likely that the additional expense of these corrections will prevent their routine use until sufficient cost saving measures such as those mentioned above, distance based cluster exclusion, or multi-method and multi-basis schemes are implemented alongside them.

The non-variational nature of the CC wavefunction introduces the most fundamentally disturbing problem of all those studied in this document, but also the least worrisome. The lack of gauge invariance of CC response properties is similar to the loss of boundedness of the CC energy (which also arises due to the non-variational wavefunction) in that upon first consideration it is very disconcerting, but analysis of its performance alleviates some of this discomfort. The comparison of modified-velocity gauge CC optical rotations to gas-phase experimental results is quite good.[25,53,130–134] Nevertheless it is of fundamental importance to confirm this agreement and have the ability to compute gauge invariant CC optical rotations in the event of poor agreement or unexplained behavior. To this end an implementation within PSI4 of a gauge invariant CC response is underway with the ultimate goal of performing the first gauge invariant CC optical rotation calculations. This implementation is based on the theory outlined in Section 4.2.3 and the expressions given in Appendix A.

Bibliography

[1] F. A. Cotton. *Chemical Applications of Group Theory.* John Wiley & Sons Inc, 3rd edition, 1990.

[2] K. Mislow and J. Siegel. *J. Am. Chem. Soc.*, 106(11):3319–3328, 1984.

[3] T. W. G. Solomons and C. B. Fryhle. *Organic Chemistry.* Wiley, 8 edition, 2003.

[4] R. Bentley. *Chirality*, 22:1–2, 2010.

[5] L. D. Barron. *Molecular Light Scattering and Optical Activity.* Cambridge University Press, Camridge, U.K., 2nd edition edition, 2004.

[6] L. Rosenfeld. *Z. Physik*, 52:161–174, 1928.

[7] D. J. Caldwell and H. Eyring. *The Theory of Optical Activity.* Wiley, New York, 1971.

[8] T. D. Crawford. *Theor. Chem. Acc.*, 115:227–245, 2006.

[9] A. Szabo and N. S. Ostlund. *Modern Quantum Chemistry: Introduction to Advanced Electronic Structure Theory.* McGraw-Hill, New York, 1st edition, 1989.

[10] J. Čížek. *J. Chem. Phys.*, 45:4256–4266, 1966.

[11] J. Čížek. *Adv. Chem. Phys.*, 14:35, 1969.

[12] T. D. Crawford and H. F. Schaefer. An introduction to coupled cluster theory for computational chemists. In K. B. Lipkowitz and D. B. Boyd, editors, *Reviews in Computational Chemistry*, volume 14, chapter 2, pages 33–136. VCH Publishers, New York, 2000.

[13] T. Helgaker, P. Jørgensen, and J. Olsen. *Molecular Electronic-Structure Theory*. John Wiley & Sons Inc, 2000.

[14] T. J. Mach and T. D. Crawford. *J. Phys. Chem. A*, 115:10045–10051, 2011.

[15] S. Grimme. *Chem. Phys. Lett.*, 339:380–388, 2001.

[16] P. L. Polavarapu. *Chirality*, 14:768–781, 2002.

[17] M. Pecul and K. Ruud. *Adv. Quantum Chem.*, 50:185–212, 2005.

[18] T. D. Crawford, M. C. Tam, and M. L. Abrams. *J. Phys. Chem. A*, 111(48):12057–12068, 2007.

[19] P. L. Polavarapu. *Chem. Rec.*, 7:125–136, 2007.

[20] J. Autschbach. *Chirality*, 21(1E):E116–E152, 2009.

[21] T. D. Crawford. *High-Accuracy Quantum Chemistry and Chiroptical Properties*, volume 1 of *Comprehensive Chiroptical Spectroscopy*. Wiley and Sons, 2012.

[22] P. L. Polavarapu. *Mol. Phys.*, 91(3):551–554, 1997.

[23] J. R. Cheeseman, M. J. Frisch, F. J. Devlin, and P. J. Stephens. *J. Phys. Chem. A*, 104:1039–1046, 2000.

[24] K. Ruud, P. J. Stephens, F. J. Devlin, P. R. Taylor, J. R. Cheeseman, and M. J. Frisch. *Chem. Phys. Lett.*, 373:606–614, 2003.

[25] S. M. Wilson, K. B. Wiberg, J. R. Cheeseman, M. J. Frisch, and P. H. Vaccaro. *J. Phys. Chem. A*, 109(51):11752–11764, 2005.

[26] T. B. Pedersen, H. Koch, L. Boman, and A. M. J. S. de Meras. *Chem. Phys. Lett.*, 393(4-6):319–326, 2004.

[27] T. D. Crawford and P. J. Stephens. *J. Phys. Chem. A*, 112:1339–1345, 2008.

[28] T. B. Pedersen, J. Kongsted, and T. D. Crawford. *Chirality*, 21(1E):E68–E75, 2009.

[29] N. J. Russ and T. D. Crawford. *Phys. Chem. Chem. Phys.*, 10:3345–3352, 2008.

[30] A. Baranowska, K. Z. Laczkowski, and A. J. Sadlej. *J. Comp. Chem.*, 31(6):1176–1181, April 2010.

[31] A. Baranowska and A. J. Sadlej. *J. Comp. Chem.*, 31(3):552–560, February 2010.

[32] F. van Duijneveldt. *IBM J. Res. Dev.*, page 945, 1971.

[33] M. C. Tam, N. J. Russ, and T. D. Crawford. *J. Chem. Phys.*, 121(8):3550–3557, 2004.

[34] K. Ruud and R. Zanasi. *Angew. Chem. Int. Ed. Engl.*, 44(23):3594–3596, 2005.

[35] T. D. Crawford, M. C. Tam, and M. L. Abrams. *Mol. Phys.*, 105:2607–2617, 2007.

[36] T. D. Kowalczyk, M. L. Abrams, and T. D. Crawford. *J. Phys. Chem. A*, 110:7649–7654, 2006.

[37] H. Koch and P. Jørgensen. *J. Chem. Phys.*, 93(5):3333–3344, September 1990.

[38] O. Christiansen, P. Jørgensen, and C. Hättig. *Int. J. Quantum Chem.*, 68(1):1–52, May 1998.

[39] T. D. Crawford, C. D. Sherrill, E. F. Valeev, J. T. Fermann, R. A. King, M. L. Leininger, S. T. Brown, C. L. Janssen, E. T. Seidl, J. P. Kenny, and W. D. Allen. *J. Comp. Chem.*, 28:1610–1616, 2007.

[40] DALTON, a molecular electronic structure program, Release 2.0 (2005), see `http://www.kjemi.uio.no/software/dalton/dalton.html`.

[41] A. D. Becke. *J. Chem. Phys.*, 98(7):5648–5652, April 1993.

[42] C. Lee, W. Yang, and R. G. Parr. *Phys. Rev. B.*, 37:785–789, 1988.

[43] O. Christiansen, H. Koch, and P. Jørgensen. *Chem. Phys. Lett.*, 243(5-6):409–418, September 1995.

[44] H. Koch, H. J. Aa. Jensen, P. Jørgensen, and T. Helgaker. *J. Chem. Phys.*, 93(5): 3345–3350, 1990.

[45] R. Kobayashi, H. Koch, and P. Jørgensen. *Chem. Phys. Lett.*, 219(1-2):30–35, March 1994.

[46] F. London. *J. Phys. Radium*, 8:397–409, 1937.

[47] R. Ditchfield. *Mol. Phys.*, 27(4):789–807, 1974.

[48] T. H. Dunning. *J. Chem. Phys.*, 90(2):1007, 1989.

[49] R. A. Kendall, T. H. Dunning, and R. J. Harrison. *J. Chem. Phys.*, 96(9):6796–6806, 1992.

[50] D. E. Woon and T. H. Dunning. *J. Chem. Phys.*, 98(2):1358, 1993.

[51] Y. Kumata, J. Furukawa, and T. Fueno. *Bull. Chem. Soc. Japan*, 43(12):3920–3921, 1970.

[52] J. Kongsted, T. B. Pedersen, M. Strange, A. Osted, A. E. Hansen, K. V. Mikkelsen, F. Pawlowski, P. Jørgensen, and C. Hättig. *Chem. Phys. Lett.*, 401:385–392, 2005.

[53] T. Müller, K. B. Wiberg, and P. H. Vaccaro. *J. Phys. Chem. A*, 104:5959–5968, 2000.

[54] P. J. Stephens, F. J. Devlin, J. R. Cheeseman, and M. J. Frisch. *J. Phys. Chem. A*, 105(22):5356–5371, 2001.

[55] B. C. Mort and J. Autschbach. *J. Phys. Chem. A*, 109(38):8617–8623, 2005.

[56] K. Mislow and J. G. Berger. *J. Am. Chem. Soc.*, 84(10):1956–1961, 1962.

[57] J. M. Janusz, L. J. Gardiner, and J. A. Berson. *J. Am. Chem. Soc.*, 99(26):8509–8510, 1977.

[58] D. A. Lightner, J. K. Gawronski, and T. D. Bouman. *J. Am. Chem. Soc.*, 102(18): 5749–5754, 1980.

[59] P. Stephens, D. M. McCann, J. Cheeseman, and M. Frisch. *Chirality*, 17:S52–S64, 2005.

[60] D. M. McCann and P. J. Stephens. *J. Org. Chem.*, 71(16):6074–6098, August 2006.

[61] A. Baranowska-Łaczkowska and K. Z. Łaczkowski. *J. Comp. Chem.*, 2013.

[62] A. Schäfer, H. Horn, and R. Ahlrichs. *J. Chem. Phys.*, 97:2571–2577, 1992.

[63] J. Stiehler and J. Hinze. *J. Phys. B: At. Mol. Opt. Phys.*, 28:4055–4071, 1995.

[64] G. D. Lindh, T. J. Mach, and T. D. Crawford. *Chem. Phys.*, 401:125–129, 2012.

[65] S. Grimme, F. Furche, and R. Ahlrichs. *Chem. Phys. Lett.*, 361:321–328, 2002.

[66] K. Ruud and T. Helgaker. *Chem. Phys. Lett.*, 352:533–539, 2002.

[67] J. Autschbach, S. Patchkovskii, T. Ziegler, S. van Gisbergen, and E. J. Baerends. *J. Chem. Phys.*, 117(2):581–592, 2002.

[68] T. B. Pedersen, H. Koch, and C. Hättig. *J. Chem. Phys.*, 110(17):8318–8327, 1999.

[69] K. Wolinski, J. F. Hinton, and P. Pulay. *J. Am. Chem. Soc.*, 112(23):8251–8260, 1990.

[70] T. Helgaker and P. Jørgensen. *J. Chem. Phys.*, 95(4):2595–2601, 1991.

[71] T. B. Pedersen. Introduction to response theory. In *Handbook of Computational Chemistry*, pages 135–156. Springer, 2012.

[72] P. Jørgensen and J. Simons. *Second Quantization-Based Methods in Quantum Chemistry*. Academic Press, New York, 1981.

[73] T. B. Pedersen and H. Koch. *Chem. Phys. Lett.*, 293:251–260, 1998.

[74] T. B. Pedersen and H. Koch. *J. Chem. Phys.*, 112(5):2139–2147, 2000.

[75] T. B. Pedersen, B. Fernández, and H. Koch. *J. Chem. Phys.*, 114(16):6983–6993, 2001.

[76] G. D. Purvis and R. J. Bartlett. *J. Chem. Phys.*, 76:1910–1918, 1982.

[77] G. E. Scuseria and H. F. Schaefer. *Chem. Phys. Lett.*, 142(5):354, 1987.

[78] R. A. Chiles and C. E. Dykstra. *J. Chem. Phys.*, 74(8):4544, 1981.

[79] N. C. Handy, J. A. Pople, M. Head-Gordon, K. Raghavachari, and G. W. Trucks. *Chem. Phys. Lett.*, 164(2,3):185, 1989.

[80] C. D. Sherrill, A. I. Krylov, E. F. C. Byrd, and M. Head-Gordon. *J. Chem. Phys.*, 109 (11):4171–4181, 1998.

[81] A. I. Krylov, C. D. Sherrill, E. F. C. Byrd, and M. Head-Gordon. *J. Chem. Phys.*, 109 (24):10669–10678, 1998.

[82] S. R. Gwaltney, C. D. Sherrill, M. Head-Gordon, and A. I. Krylov. *J. Chem. Phys.*, 113(9):3548–3560, 2000.

[83] A. I. Krylov, C. D. Sherrill, and M. Head-Gordon. *J. Chem. Phys.*, 113(16):6509–6527, 2000.

[84] I. Shavitt and R. J. Bartlett. *Many-Body Methods in Chemistry and Physics: MBPT and Coupled-Cluster Theory*. Cambridge University Press, Cambridge, 2009.

[85] J. E. Rice, R. D. Amos, N. C. Handy, T. J. Lee, and H. F. Schaefer. *J. Chem. Phys.*, 85(2):963–968, 1986.

[86] L. Adamowicz, W. D. Laidig, and R. J. Bartlett. *Int. J. Quantum Chem. Symp.*, 18: 245, 1984.

[87] A. C. Scheiner, G. E. Scuseria, J. E. Rice, T. J. Lee, and H. F. Schaefer. *J. Chem. Phys.*, 87(9):5361, 1987.

[88] Y. Yamaguchi, Y. Osamura, J. D. Goddard, and H. F. Schaefer. *A New Dimension to Quantum Chemistry: Analytic Derivative Methods in* Ab Initio *Molecular Electronic Structure Theory*. Number 29 in International Series of Monographs on Chemistry. Oxford Univ. Press, New York, 1994.

[89] N. C. Handy and H. F. Schaefer. *J. Chem. Phys.*, 81(11):5031–5033, 1984.

[90] A. Köhn and J. Olsen. *J. Chem. Phys.*, 122(8):084116, 2005.

[91] T. D. Crawford. High-accuracy quantum chemistry and chiroptical properties. In N. Berova, K. Nakanishi, R. W. Woody, and P. Polavarapu, editors, *Comprehensive Chiroptical Spectroscopy*, volume 1, pages 675–697. Wiley, 2011.

[92] P. L. Polavarapu, D. K. Chakraborty, and K. Ruud. *Chem. Phys. Lett.*, 319:595–600, 2000.

[93] T. J. Lee and P. R. Taylor. *Int. J. Quantum Chem. Symp.*, 23:199, 1989.

[94] K. Ruud, P. R. Taylor, and P.-O. Åstrand. *Chem. Phys. Lett.*, 337:217–223, 2001.

[95] J. Kongsted, T. B. Pedersen, L. Jensen, A. E. Hansen, and K. V. Mikkelsen. *J. Am. Chem. Soc.*, 128(3):976–982, 2006.

[96] T. B. Pedersen, J. Kongsted, T. D. Crawford, and K. Ruud. *J. Chem. Phys.*, 130: 034310, 2009.

[97] J. Olsen and P. Jørgensen. *J. Chem. Phys.*, 82(7):3235–3264, 1985.

[98] T. B. Pedersen and H. Koch. *J. Chem. Phys.*, 106(19):8059–8072, 1997.

[99] T. J. Mach and T. D. Crawford. *Theor. Chem. Acc.*, 133:1449, 2014.

[100] A. Koslowski, N. Sreerama, and R. W. Woody. Theoretical approach to electronic optical activity. In N. Berova, K. Nakanishi, and R. W. Woody, editors, *Circular Dichroism: Principles and Applications*, chapter 3, pages 55–95. Wiley, New York, 2nd edition, 2000.

[101] S. Grimme, S. D. Peyerimhoff, S. Bartram, F. Vögtle, A. Breest, and J. Hormes. *Chem. Phys. Lett.*, 213(1-2):32–40, 1993.

[102] S. Grimme. *Chem. Phys. Lett.*, 259:128–137, 1996.

[103] F. Pulm, J. Schramm, J. Hormes, S. Grimme, and S. D. Peyerimhoff. *Chem. Phys.*, 224:143–155, 1997.

[104] S. Grimme and M. Waletzke. *J. Chem. Phys.*, 111(13):5645–5655, 1999.

[105] M. Carnell, S. Grimme, and S. D. Peyerimhoff. *Chem. Phys.*, 179(3):385–394, 1994.

[106] A. E. Hansen and K. L. Bak. *Enantiomer*, 4(5):455, 1999.

[107] J. Autschbach, T. Ziegler, S. J. A. van Gisbergen, and E. J. Baerends. *J. Chem. Phys.*, 116(16):6930–6940, 2002.

[108] J. Autschbach, F. E. Jorge, and T. Ziegler. *Inorg. Chem.*, 42(9):2867–2877, 2003.

[109] M. Pecul, K. Ruud, and T. Helgaker. *Chem. Phys. Lett.*, 388:110–119, 2004.

[110] S. Grimme. Calculation of the electronic spectra of large molecules. In K. B. Lipkowitz, R. Larter, and T. R. Cundari, editors, *Reviews in Computational Chemistry*, volume 20, chapter 3, pages 153–218. VCH Publishers, New York, 2004.

[111] P. J. Stephens, K. J. Jalkanene, F. J. Devlin, and C. F. Chabalowski. *J. Phys. Chem.*, 97:6107–6110, 1993.

[112] K. L. Bak, P. Jørgensen, T. Helgaker, K. Ruud, and H. J. Aa. Jensen. *J. Chem. Phys.*, 98(11):8873–8887, 1993.

[113] K. L. Bak, P. Jørgensen, T. Helgaker, and K. Ruud. *Faraday Discuss.*, 99:121–129, 1994.

[114] K. L. Bak, O. Bludský, and P. Jørgensen. *J. Chem. Phys.*, 103(24):10548–10555, 1995.

[115] J. R. Cheeseman, M. J. Frisch, F. J. Devlin, and P. J. Stephens. *Chem. Phys. Lett.*, 252:211–220, 1996.

[116] F. J. Devlin, P. J. Stephens, J. R. Cheeseman, and M. J. Frisch. *J. Phys. Chem. A*, 101:9912–9924, 1997.

[117] P. J. Stephens and F. J. Devlin. *Chirality*, 12:172–179, 2000.

[118] F. J. Devlin, P. J. Stephens, P. Scafato, S. Superchi, and C. Rosini. *Chirality*, 14: 400–406, 2002.

[119] P. L. Polavarapu. *J. Phys. Chem.*, 94:8106–8112, 1990.

[120] L. A. Nafie. *Ann. Rev. Phys. Chem.*, 48:357–386, 1997.

[121] T. Helgaker, K. Ruud, K. L. Bak, P. Jørgensen, and J. Olsen. *Faraday Discuss.*, 99: 165–180, 1994.

[122] L. D. Barron, L. Hecht, I. H. McColl, and E. W. Blanch. *Mol. Phys.*, 102(8):731–744, 2004.

[123] P. Bouř. *J. Comp. Chem.*, 22(4):426–435, 2001.

[124] M. Pecul and A. Rizzo. *Mol. Phys.*, 101(13):2073–2081, 2003.

[125] M. Pecul and K. Ruud. *Int. J. Quantum Chem.*, 104(5):816–829, 2005.

[126] T. D. Crawford and K. Ruud. *ChemPhysChem*, 12:3442–3448, 2011.

[127] W. Hug. *Chem. Phys.*, 264:53–69, 2001.

[128] S. Luber and M. Reiher. *Chem. Phys.*, 346:212–223, 2008.

[129] K. Ruud and A. J. Thorvaldsen. *Chirality*, 21:E54–E67, 2009.

[130] T. Müller, K. B. Wiberg, P. H. Vaccaro, J. R. Cheeseman, and M. J. Frisch. *J. Opt. Soc. Am. B*, 19(1):125–141, 2002.

[131] K. B. Wiberg, P. H. Vaccaro, and J. R. Cheeseman. *J. Am. Chem. Soc.*, 125:1888–1896, 2003.

[132] K. B. Wiberg, Y. G. Wang, P. H. Vaccaro, J. R. Cheeseman, G. Trucks, and M. J. Frisch. *J. Phys. Chem. A*, 108(1):32–38, 2004.

[133] K. B. Wiberg, Y. Wang, S. M. Wilson, P. H. Vaccaro, and J. R. Cheeseman. *J. Phys. Chem. A*, 109(15):3448–3453, 2005.

[134] K. B. Wiberg, Y. Wang, S. M. Wilson, P. H. Vaccaro, W. L. Jorgensen, T. D. Crawford, M. L. Abrams, J. R. Cheeseman, and M. Luderer. *J. Phys. Chem. A*, 112:2415–2422, 2008.

[135] P. J. Stephens, F. J. Devlin, J. R. Cheeseman, M. J. Frisch, O. Bortolini, and P. Besse. *Chirality*, 15:S57–S64, 2003.

[136] B. C. Mort and J. Autschbach. *J. Phys. Chem. A*, 110:11381–11383, 2006.

[137] J. Kongsted and K. Ruud. *Chem. Phys. Lett.*, 451:226–232, 2008.

[138] T. D. Crawford and W. D. Allen. *Mol. Phys.*, 107:1041–1057, 2009.

[139] P. Lahiri, K. B. Wiberg, P. H. Vaccaro, M. Caricato, and T. D. Crawford. *Angew. Chem. Int. Ed.*, 53:1386–1389, 2014.

[140] J.Tomasi and M. Persico. *Chem. Rev.*, 94:2027–2094, 1994.

[141] C. J. Cramer and D. G. Truhlar. *Chem. Rev.*, 99:2161–2200, 1999.

[142] J. Tomasi, R. Cammi, B. Mennucci, C. Cappelli, and S. Corni. *Phys. Chem. Chem. Phys.*, 4:5697–5712, 2002.

[143] J. Tomasi, B. Mennucci, and R. Cammi. *Chem. Rev.*, 105:2999–3093, 2005.

[144] B. Mennucci, J. Tomasi, R. Cammi, J. R. Cheeseman, M. J. Frisch, F. J. Devlin, S. Gabriel, and P. J. Stephens. *J. Phys. Chem. A*, 106(25):6102–6113, 2002.

[145] M. Pecul, D. Marchesan, K. Ruud, and S. Coriani. *J. Chem. Phys.*, 122(2):024106, 2005.

[146] Z. Su and Y. Xu. *Angew. Chem. Int. Ed. Engl.*, 46:6163–6166, 2007.

[147] M. Losada, P. Nguyen, and Y. Xu. *J. Phys. Chem. A*, 112:5621–5627, 2008.

[148] P. Mukhopadhyay, G. Zuber, M. Goldsmith, P. Wipf, and D. N. Beratan. *Chem. Phys. Chem.*, 7:2483–2486, 2006.

[149] P. Mukhopadhyay, G. Zuber, P. Wipf, and D. N. Beratan. *Angew. Chem. Int. Ed. Engl.*, 46:6450–6452, 2007.

[150] R. G. Parr and W. Yang. *Density-Functional Theory of Atoms and Molecules*. Oxford University, New York, 1989.

[151] C. Choi, K. Ruedenberg, and M. Gordon. *J. Comp. Chem.*, 22(13):1484–1501, OCT 2001. ISSN 0192-8651.

[152] M. S. Gordon, D. G. Federov, S. R. Pruitt, and L. V. Slipchenko. *Chem. Rev.*, 112: 632–672, 2011.

[153] M. Schütz and H.-J. Werner. *J. Chem. Phys.*, 114(2):661–681, 2001.

[154] N. J. Russ and T. D. Crawford. *Chem. Phys. Lett.*, 400(1-3):104–111, December 2004.

[155] H. R. McAlexander, T. J. Mach, and T. D. Crawford. *Phys. Chem. Chem. Phys.*, 14: 7830–7836, 2012.

[156] D. Hankins and J. W. Moskowitz. *J. Chem. Phys.*, 53(12):4544–4554, 1970.

[157] S. S. Xantheas. *J. Chem. Phys.*, 100(10):7523–7534, 1994.

[158] R. A. Christie and K. D. Jordan. *n*-body decomposition approach to the calculation of interaction energies of water clusters. In D. J. Wales, editor, *Intermolecular Forces and Clusters II*, volume 116 of *Structure and Bonding*, pages 27–41. Springer, 2005.

[159] H. R. Leverentz, K. A. Maerzke, S. J. Keasler, J. I. Siepmann, and D. G. Truhlar. *Phys. Chem. Chem. Phys.*, 14:7669–7678, 2012.

[160] D. M. Bates, J. R. Smith, T. Janowski, and G. S. Tschumper. *J. Chem. Phys.*, 135: 044123, 2011.

[161] R. M. Richard, K. U. Lao, and J. M. Herbert. *J. Chem. Phys.*, 139:224102, 2013.

[162] K. L. Theel, S. Wen, and G. J. O. Beran. *J. Chem. Phys.*, 139:081103, 2013.

[163] N. Ferré and X. Assfeld. *J. Mol. Struct. (Theochem)*, 632:83–90, 2003.

[164] S. Pronk, S. Páll, R. Schulz, P. Larsson, P. Bjelkmar, R. Apostolov, M. R. Shirts, J. C. Smith, P. M. Kasson, D. van der Spoel, B. Hess, and E. Lindahl. *Bioinformatics*, 29 (7):845–854, 2013.

[165] M. J. Frisch, G. W. Trucks, H. B. Schlegel, G. E. Scuseria, M. A. Robb, J. R. Cheeseman, G. Scalmani, V. Barone, B. Mennucci, G. A. Petersson, H. Nakatsuji, M. Caricato, X. Li, H. P. Hratchian, A. F. Izmaylov, J. Bloino, G. Zheng, J. L. Sonnenberg, M. Hada, M. Ehara, K. Toyota, R. Fukuda, J. Hasegawa, M. Ishida, T. Nakajima, Y. Honda, O. Kitao, H. Nakai, T. Vreven, J. J. A. Montgomery, J. E. Peralta, F. Ogliaro, M. Bearpark, J. J. Heyd, E. Brothers, K. N. Kudin, V. N. Staroverov, R. Kobayashi, J. Normand, K. Raghavachari, A. Rendell, J. C. Burant, S. S. Iyengar, J. Tomasi, M. Cossi, N. Rega, J. M. Millam, M. Klene, J. E. Knox, J. B. Cross, V. Bakken, C. Adamo, J. Jaramillo, R. Gomperts, R. E. Stratmann, O. Yazyev, A. J. Austin, R. Cammi, C. Pomelli, J. W. Ochterski, R. L. Martin, K. Morokuma, V. G. Zakrzewski, G. A. Voth, P. Salvador, J. J. Dannenberg, S. Dapprich, A. D. Daniels, Ö. Farkas, J. B. Foresman, J. V. Ortiz, J. Cioslowski, and D. J. Fox. Gaussian 09 Revision A.1. Gaussian Inc. Wallingford CT 2009.

[166] J. M. Turney, A. C. Simmonett, R. M. Parrish, E. G. Hohenstein, F. A. Evangelista,

J. T. Fermann, B. J. Mintz, L. A. Burns, J. J. Wilke, M. L. Abrams, N. J. Russ, M. L. Leininger, C. L. Janssen, E. T. Seidl, W. D. Allen, H. F. Schaefer, R. A. King, E. F. Valeev, C. D. Sherrill, and T. D. Crawford. *WIREs Comput. Mol. Sci.*, 2(4):556–565, 2012.

[167] G. S. Tschumper. *Chem. Phys. Lett.*, 427:185–191, 2006.

[168] F. Lipparini, F. Egidi, C. Cappelli, and V. Barone. *J. Chem. Theory Comp.*, 2013.

[169] D. M. Bates, J. R. Smith, and G. S. Tschumper. *J. Chem. Theory Comp.*, 7:2753–2760, 2011.

[170] E. E. Dahlke and D. G. Truhlar. *J. Chem. Theory Comp.*, 3:1342–1348, 2007.

[171] M. D. Kundrat and J. Autschbach. *J. Chem. Theory Comp.*, 4:1902–1914, 2008.

[172] S. B. Boys and F. Bernardi. *Mol. Phys.*, 19:553, 1970.

[173] P. Valiron and I. Mayer. *Chem. Phys. Lett.*, 275:46–55, 1997.

[174] R. M. Richard, K. U. Lao, and J. M. Herbert. *J. Phys. Chem. Lett.*, 4:2674–2680, 2013.

Appendix A

Gauge Invariant Coupled Cluster Algebra

A.1 Response Amplitudes

A.1.1 κ^e Equation

$$
\begin{aligned}
0 = &- \sum_{b} \widetilde{F}_{ab}\kappa^{e}_{ib} + \sum_{j} \widetilde{F}_{ji}\kappa^{e}_{ja} - \sum_{\substack{j\\b}} \widetilde{V}_{jabi}\kappa^{e}_{jb} + \frac{1}{2}\sum_{\substack{jk\\bc}} \widetilde{V}_{acjk}\kappa^{e}_{ib}\lambda^{jk}_{bc} + \frac{1}{2}\sum_{\substack{jk\\bc}} \widetilde{V}_{bcik}\kappa^{e}_{ja}\lambda^{jk}_{bc} + \frac{1}{2}\sum_{\substack{jk\\bcd}} \widetilde{F}_{ad}\kappa^{e}_{kd}\lambda^{jk}_{bc} \\
&- \frac{1}{2}\sum_{\substack{jkl\\bc}} \widetilde{F}_{li}\kappa^{e}_{lc}t^{ba}_{jk}\lambda^{jk}_{bc} - \frac{1}{2}\sum_{\substack{jkl\\bc}} \widetilde{F}_{li}\kappa^{e}_{ja}t^{bc}_{lk}\lambda^{jk}_{bc} + \frac{1}{2}\sum_{\substack{jk\\bcd}} \widetilde{F}_{ad}\kappa^{e}_{ib}t^{dc}_{jk}\lambda^{jk}_{bc} + \frac{1}{2}\sum_{\substack{jkl\\bcd}} \widetilde{V}_{ladi}\kappa^{e}_{kd}t^{bc}_{jl}\lambda^{jk}_{bc} + \frac{1}{2}\sum_{\substack{jkl\\bcd}} \widetilde{V}_{ladi}\kappa^{e}_{lc}t^{bd}_{jk}\lambda^{jk}_{bc} \\
&+ \sum_{\substack{jkl\\bcd}} \widetilde{V}_{lcdi}\kappa^{e}_{ka}t^{bd}_{jl}\lambda^{jk}_{bc} + \sum_{\substack{jkl\\bcd}} \widetilde{V}_{ladk}\kappa^{e}_{ic}t^{bd}_{jl}\lambda^{jk}_{bc} + \frac{1}{2}\sum_{\substack{jkl\\bcd}} \widetilde{V}_{ladj}\kappa^{e}_{ld}t^{bc}_{ik}\lambda^{jk}_{bc} + \frac{1}{2}\sum_{\substack{jkl\\bcd}} \widetilde{V}_{lbdi}\kappa^{e}_{ld}t^{ac}_{jk}\lambda^{jk}_{bc} - \sum_{\substack{jkl\\bcd}} \widetilde{V}_{ladk}\kappa^{e}_{lb}t^{dc}_{ji}\lambda^{jk}_{bc} \\
&- \frac{1}{2}\sum_{\substack{jkl\\bcd}} \widetilde{V}_{ladk}\kappa^{e}_{jd}t^{bc}_{li}\lambda^{jk}_{bc} - \frac{1}{2}\sum_{\substack{jkl\\bcd}} \widetilde{V}_{ladk}\kappa^{e}_{id}t^{bc}_{jl}\lambda^{jk}_{bc} - \frac{1}{2}\sum_{\substack{jkl\\bcd}} \widetilde{V}_{lcdi}\kappa^{e}_{la}t^{bd}_{jk}\lambda^{jk}_{bc} - \frac{1}{2}\sum_{\substack{jkl\\bcd}} \widetilde{V}_{lcdi}\kappa^{e}_{lb}t^{da}_{jk}\lambda^{jk}_{bc} - \sum_{\substack{jkl\\bcd}} \widetilde{V}_{lcdi}\kappa^{e}_{jd}t^{ba}_{lk}\lambda^{jk}_{bc} \\
&- \sum_{\substack{jk\\bcde}} \widetilde{V}_{bade}\kappa^{e}_{jd}t^{ec}_{ik}\lambda^{jk}_{bc} - \sum_{\substack{jklm\\bc}} \widetilde{V}_{lmji}\kappa^{e}_{lb}t^{ac}_{mk}\lambda^{jk}_{bc} - \frac{1}{2}\sum_{\substack{jk\\bcde}} \widetilde{V}_{cade}\kappa^{e}_{ie}t^{bd}_{jk}\lambda^{jk}_{bc} - \frac{1}{2}\sum_{\substack{jklm\\bc}} \widetilde{V}_{lmki}\kappa^{e}_{ma}t^{bc}_{jl}\lambda^{jk}_{bc} + \sum_{\substack{jk\\bcde}} \widetilde{V}_{bade}\kappa^{e}_{ke}t^{dc}_{ji}\lambda^{jk}_{bc} \\
&+ \sum_{\substack{jklm\\bc}} \widetilde{V}_{lmji}\kappa^{e}_{mc}t^{ba}_{lk}\lambda^{jk}_{bc} + \frac{1}{2}\sum_{\substack{jk\\bcde}} \widetilde{V}_{bade}\kappa^{e}_{ic}t^{de}_{jk}\lambda^{jk}_{bc} + \frac{1}{2}\sum_{\substack{jklm\\bc}} \widetilde{V}_{lmji}\kappa^{e}_{ka}t^{bc}_{lm}\lambda^{jk}_{bc} - \frac{1}{2}\sum_{\substack{j\\bc}} \widetilde{V}_{jabc}X^{bc}_{ji} + \frac{1}{2}\sum_{\substack{jk\\b}} \widetilde{V}_{jkbi}X^{ba}_{jk} \\
&+ \frac{1}{2}\sum_{\substack{jk\\bc}} \widetilde{F}_{ak}X^{bc}_{ji}\lambda^{jk}_{bc} + \frac{1}{2}\sum_{\substack{jk\\bc}} \widetilde{F}_{ci}X^{ba}_{jk}\lambda^{jk}_{bc} + \frac{1}{2}\sum_{\substack{jkl\\bc}} \widetilde{V}_{alij}X^{bc}_{lk}\lambda^{jk}_{bc} - \frac{1}{2}\sum_{\substack{jk\\bcd}} \widetilde{V}_{abid}X^{dc}_{jk}\lambda^{jk}_{bc} - \sum_{\substack{jk\\bcd}} \widetilde{V}_{bajd}X^{dc}_{ik}\lambda^{jk}_{bc} + \sum_{\substack{jkl\\bc}} \widetilde{V}_{blji}X^{ac}_{lk}\lambda^{jk}_{bc} \\
&+ \frac{1}{4}\sum_{\substack{jkl\\bcde}} \widetilde{V}_{lade}X^{de}_{ki}t^{bc}_{jl}\lambda^{jk}_{bc} + \frac{1}{2}\sum_{\substack{jkl\\bcde}} \widetilde{V}_{lade}X^{ce}_{li}t^{bd}_{jk}\lambda^{jk}_{bc} - \frac{1}{2}\sum_{\substack{jklm\\bcd}} \widetilde{V}_{lmdi}X^{da}_{km}t^{bc}_{jl}\lambda^{jk}_{bc} - \frac{1}{4}\sum_{\substack{jklm\\bcd}} \widetilde{V}_{lmdi}X^{ca}_{lm}t^{bd}_{jk}\lambda^{jk}_{bc} + \frac{1}{4}\sum_{\substack{jkl\\bcde}} \widetilde{V}_{lade}X^{bc}_{jl}t^{de}_{ki}\lambda^{jk}_{bc} \\
&+ \frac{1}{2}\sum_{\substack{jkl\\bcde}} \widetilde{V}_{lade}X^{bd}_{jk}t^{ce}_{li}\lambda^{jk}_{bc} - \frac{1}{2}\sum_{\substack{jklm\\bcd}} \widetilde{V}_{lmdi}X^{bc}_{jl}t^{da}_{km}\lambda^{jk}_{bc} - \frac{1}{4}\sum_{\substack{jklm\\bcd}} \widetilde{V}_{lmdi}X^{bd}_{jk}t^{ca}_{lm}\lambda^{jk}_{bc} - \sum_{\substack{jkl\\bcde}} \widetilde{V}_{lade}X^{ec}_{ik}t^{bd}_{jl}\lambda^{jk}_{bc} + \sum_{\substack{jklm\\bcd}} \widetilde{V}_{lmdi}X^{ac}_{mk}t^{bd}_{jl}\lambda^{jk}_{bc} \\
&- \sum_{\substack{jkl\\bcde}} \widetilde{V}_{lade}X^{bd}_{jl}t^{ec}_{ik}\lambda^{jk}_{bc} + \sum_{\substack{jklm\\bcd}} \widetilde{V}_{lmdi}X^{bd}_{jl}t^{ac}_{mk}\lambda^{jk}_{bc} + \frac{1}{4}\sum_{\substack{jkl\\bcde}} \widetilde{V}_{lade}X^{bc}_{ik}t^{de}_{lj}\lambda^{jk}_{bc} - \frac{1}{2}\sum_{\substack{jklm\\bcd}} \widetilde{V}_{lmdi}X^{ac}_{jk}t^{db}_{lm}\lambda^{jk}_{bc} + \frac{1}{4}\sum_{\substack{jkl\\bcde}} \widetilde{V}_{lade}X^{de}_{lj}t^{bc}_{ik}\lambda^{jk}_{bc} \\
&- \frac{1}{2}\sum_{\substack{jklm\\bcd}} \widetilde{V}_{lmdi}X^{db}_{lm}t^{ac}_{jk}\lambda^{jk}_{bc} + \frac{1}{8}\sum_{\substack{jklm\\bcd}} \widetilde{V}_{lmdi}X^{da}_{jk}t^{bc}_{lm}\lambda^{jk}_{bc} - \frac{1}{8}\sum_{\substack{jkl\\bcde}} \widetilde{V}_{lade}X^{bc}_{li}t^{de}_{jk}\lambda^{jk}_{bc} + \frac{1}{8}\sum_{\substack{jklm\\bcd}} \widetilde{V}_{lmdi}X^{bc}_{lm}t^{da}_{jk}\lambda^{jk}_{bc} - \frac{1}{8}\sum_{\substack{jkl\\bcde}} \widetilde{V}_{lade}X^{de}_{jk}t^{bc}_{li}\lambda^{jk}_{bc}
\end{aligned}
$$

$$
\begin{aligned}
&+\sum_{\substack{j\\b}}\widetilde{V}_{baji}\kappa^{d}_{bj}-\sum_{\substack{jk\\bc}}\widetilde{V}_{kbci}\kappa^{d}_{bj}t^{ca}_{kj}-\sum_{\substack{jk\\bc}}\widetilde{V}_{kacj}\kappa^{d}_{bj}t^{cb}_{ki}+\frac{1}{2}\sum_{\substack{j\\bcd}}\widetilde{V}_{bacd}\kappa^{d}_{bj}t^{cd}_{ji}\\
&+\frac{1}{2}\sum_{\substack{jkl\\b}}\widetilde{V}_{klji}\kappa^{d}_{bj}t^{ba}_{kl}-\sum_{\substack{jkl\\bcd}}\widetilde{V}_{bcik}\kappa^{d}_{bj}t^{ad}_{jl}\lambda^{kl}_{cd}-\sum_{\substack{jkl\\bcd}}\widetilde{V}_{acjk}\kappa^{d}_{bj}t^{bd}_{il}\lambda^{kl}_{cd}\\
&-\frac{1}{2}\sum_{\substack{jkl\\bcd}}\widetilde{V}_{bajk}\kappa^{d}_{bj}t^{cd}_{il}\lambda^{kl}_{cd}-\frac{1}{2}\sum_{\substack{jkl\\bcd}}\widetilde{V}_{bcji}\kappa^{d}_{bj}t^{ad}_{kl}\lambda^{kl}_{cd}-\frac{1}{2}\sum_{\substack{jkl\\bcd}}\widetilde{V}_{abik}\kappa^{d}_{bj}t^{cd}_{jl}\lambda^{kl}_{cd}\\
&-\frac{1}{2}\sum_{\substack{jkl\\bcd}}\widetilde{V}_{acij}\kappa^{d}_{bj}t^{bd}_{kl}\lambda^{kl}_{cd}+\frac{1}{2}\sum_{\substack{jklm\\bcde}}\widetilde{V}_{mdei}\kappa^{d}_{dl}t^{be}_{jk}t^{ca}_{ml}\lambda^{jk}_{bc}+\frac{1}{2}\sum_{\substack{jklm\\bcde}}\widetilde{V}_{mdei}\kappa^{d}_{dl}t^{bc}_{jm}t^{ea}_{kl}\lambda^{jk}_{bc}\\
&+\frac{1}{2}\sum_{\substack{jklm\\bcde}}\widetilde{V}_{macl}\kappa^{d}_{dl}t^{be}_{jk}t^{cd}_{mi}\lambda^{jk}_{bc}+\frac{1}{2}\sum_{\substack{jklm\\bcde}}\widetilde{V}_{macl}\kappa^{d}_{dl}t^{bc}_{jm}t^{ed}_{ki}\lambda^{jk}_{bc}+\frac{1}{2}\sum_{\substack{jkl\\bcdef}}\widetilde{V}_{acef}\kappa^{d}_{ck}t^{be}_{ji}t^{fd}_{kl}\lambda^{jl}_{bd}\\
&+\frac{1}{2}\sum_{\substack{jklmn\\bcd}}\widetilde{V}_{mnik}\kappa^{d}_{ck}t^{ba}_{jm}t^{cd}_{nl}\lambda^{jl}_{bd}-\frac{1}{2}\sum_{\substack{jklm\\bcde}}\widetilde{V}_{kacl}\kappa^{d}_{dl}t^{bc}_{jk}t^{de}_{im}\lambda^{jm}_{be}\\
&+\frac{1}{2}\sum_{\substack{jklm\\bcde}}\widetilde{V}_{jdbi}\kappa^{d}_{dk}t^{bc}_{jk}t^{ae}_{lm}\lambda^{lm}_{ce}+\frac{1}{2}\sum_{\substack{jklm\\bcde}}\widetilde{V}_{jcbi}\kappa^{d}_{cl}t^{ba}_{jk}t^{de}_{lm}\lambda^{km}_{de}-\frac{1}{2}\sum_{\substack{jklm\\bcde}}\widetilde{V}_{kdci}\kappa^{d}_{dl}t^{bc}_{jk}t^{ae}_{lm}\lambda^{jm}_{be}\\
&+\frac{1}{2}\sum_{\substack{jklm\\bcde}}\widetilde{V}_{jabl}\kappa^{d}_{cl}t^{bc}_{jk}t^{de}_{im}\lambda^{km}_{de}+\frac{1}{2}\sum_{\substack{jklm\\bcde}}\widetilde{V}_{jabk}\kappa^{d}_{dk}t^{bc}_{ji}t^{de}_{lm}\lambda^{lm}_{ce}+\frac{1}{4}\sum_{\substack{jklm\\bcde}}\widetilde{V}_{kedi}\kappa^{d}_{ej}t^{bc}_{jk}t^{da}_{lm}\lambda^{lm}_{bc}\\
&+\frac{1}{4}\sum_{\substack{jklm\\bcde}}\widetilde{V}_{lacm}\kappa^{d}_{bm}t^{bc}_{jk}t^{de}_{li}\lambda^{jk}_{de}-\frac{1}{4}\sum_{\substack{jkl\\bcdef}}\widetilde{V}_{acbd}\kappa^{d}_{cj}t^{bd}_{ik}t^{ef}_{jl}\lambda^{kl}_{ef}-\frac{1}{4}\sum_{\substack{jkl\\bcdef}}\widetilde{V}_{bacd}\kappa^{d}_{bj}t^{cd}_{jk}t^{ef}_{il}\lambda^{kl}_{ef}\\
&-\frac{1}{4}\sum_{\substack{jklmn\\bcd}}\widetilde{V}_{jlik}\kappa^{d}_{bk}t^{ac}_{jl}t^{bd}_{mn}\lambda^{mn}_{cd}-\frac{1}{4}\sum_{\substack{jklmn\\bcd}}\widetilde{V}_{klji}\kappa^{d}_{bj}t^{bc}_{kl}t^{ad}_{mn}\lambda^{mn}_{cd}\\
&+\frac{1}{8}\sum_{\substack{jkl\\bcdef}}\widetilde{V}_{bacd}\kappa^{d}_{bk}t^{cd}_{jl}t^{ef}_{ki}\lambda^{jl}_{ef}+\frac{1}{8}\sum_{\substack{jklmn\\bcd}}\widetilde{V}_{klji}\kappa^{d}_{cj}t^{bd}_{kl}t^{ca}_{mn}\lambda^{mn}_{bd}
\end{aligned}
$$

$$
\begin{aligned}
&+\frac{1}{2}\sum_{\substack{jk\\bc}}\widetilde{F}_{ci}Y^{jk}_{bc}t^{ba}_{jk}+\frac{1}{2}\sum_{\substack{jk\\bc}}\widetilde{F}_{ak}Y^{jk}_{bc}t^{bc}_{ji}-\frac{1}{2}\sum_{\substack{jk\\bcd}}\widetilde{V}_{abid}Y^{jk}_{bc}t^{dc}_{jk}+\frac{1}{2}\sum_{\substack{jkl\\bc}}\widetilde{V}_{alij}Y^{jk}_{bc}t^{bc}_{lk}\\
&-\sum_{\substack{jk\\bcd}}\widetilde{V}_{cakd}Y^{jk}_{bc}t^{bd}_{ji}+\sum_{\substack{jkl\\bc}}\widetilde{V}_{clki}Y^{jk}_{bc}t^{ba}_{jl}-\frac{1}{4}\sum_{\substack{jklm\\bcd}}\widetilde{V}_{lmdi}Y^{jk}_{bc}t^{db}_{lm}t^{ac}_{jk}\\
&+\frac{1}{4}\sum_{\substack{jkl\\bcde}}\widetilde{V}_{lade}Y^{jk}_{bc}t^{de}_{lj}t^{bc}_{ik}-\frac{1}{2}\sum_{\substack{jkl\\bcde}}\widetilde{V}_{kade}Y^{jl}_{bc}t^{bc}_{jk}t^{ec}_{il}+\frac{1}{2}\sum_{\substack{jklm\\bcd}}\widetilde{V}_{lmdi}Y^{jk}_{bc}t^{bd}_{jl}t^{ac}_{mk}\\
&+\frac{1}{4}\sum_{\substack{jkl\\bcde}}\widetilde{V}_{lade}Y^{jk}_{bc}t^{bc}_{jl}t^{de}_{ki}+\frac{1}{2}\sum_{\substack{jklm\\bcd}}\widetilde{V}_{lmdi}Y^{jk}_{bc}t^{bc}_{jl}t^{da}_{km}+\frac{1}{2}\sum_{\substack{jkl\\bcde}}\widetilde{V}_{lade}Y^{jk}_{bc}t^{bd}_{jk}t^{ce}_{li}\\
&-\frac{1}{4}\sum_{\substack{jklm\\bcd}}\widetilde{V}_{lmdi}Y^{jk}_{bc}t^{bd}_{jk}t^{ca}_{lm}+\frac{1}{4}\sum_{\substack{jk\\bcd}}\widetilde{V}_{bcid}Y^{jk}_{bc}t^{ad}_{jk}-\frac{1}{4}\sum_{\substack{jkl\\bc}}\widetilde{V}_{aljk}Y^{jk}_{bc}t^{bc}_{il}\\
&-\frac{1}{8}\sum_{\substack{jklm\\bcd}}\widetilde{V}_{lmci}Y^{jk}_{bd}t^{ac}_{jk}t^{bd}_{lm}+\frac{1}{8}\sum_{\substack{jkl\\bcde}}\widetilde{V}_{jacd}Y^{kl}_{be}t^{be}_{ij}t^{cd}_{kl}+\widetilde{C}_{ai}-\frac{1}{2}\sum_{\substack{jk\\bc}}\widetilde{C}_{ci}t^{ba}_{jk}\lambda^{jk}_{bc}\\
&-\frac{1}{2}\sum_{\substack{jk\\bc}}\widetilde{C}_{ak}t^{bc}_{ji}\lambda^{jk}_{bc}+\omega\kappa^{e}_{ia}-\frac{1}{2}\omega\sum_{\substack{jk\\bc}}\kappa^{e}_{ic}t^{ba}_{jk}\lambda^{jk}_{bc}-\frac{1}{2}\omega\sum_{\substack{jk\\bc}}\kappa^{e}_{ka}t^{bc}_{ji}\lambda^{jk}_{bc}
\end{aligned}
\tag{A.1}
$$

A.1.2 X_2 Equation

$$
\begin{aligned}
0 = &-P_{ab}\sum_{k}\overline{V}_{akij}\kappa^{e}_{kb} + P_{ij}\sum_{c}\overline{V}_{abic}\kappa^{e}_{jc} + \sum_{\substack{k\\c}}\overline{W}_{kabcij}\kappa^{e}_{kc} + \sum_{c}\overline{F}_{bc}X^{ac}_{ij} - \sum_{c}\overline{F}_{ac}X^{bc}_{ij} - \sum_{k}\overline{F}_{kj}X^{ab}_{ik} \\
&+ \sum_{k}\overline{F}_{ki}X^{ab}_{jk} + P_{ij}P_{ab}\sum_{\substack{k\\c}}\overline{V}_{kbcj}X^{ac}_{ij} + \frac{1}{2}\sum_{cd}\overline{V}_{abcd}X^{cd}_{ij} + \frac{1}{2}\sum_{kl}\overline{V}_{klij}X^{ab}_{kl} - \frac{1}{2}P_{ab}\sum_{\substack{kl\\c}}\overline{W}_{kalcij}X^{cb}_{kl} \\
&+ \frac{1}{2}P_{ij}\sum_{\substack{k\\cd}}\overline{W}_{kabcid}X^{cd}_{kj} + P_{ij}\sum_{\substack{k\\c}}\widetilde{F}_{cj}\kappa^{d}_{ck}t^{ab}_{ik} + P_{ab}\sum_{\substack{k\\c}}\widetilde{F}_{bk}\kappa^{d}_{ck}t^{ac}_{ij} + P_{ij}P_{ab}\sum_{\substack{kl\\c}}\widetilde{V}_{alik}\kappa^{d}_{ck}t^{cb}_{lj} \\
&- P_{ij}P_{ab}\sum_{\substack{k\\cd}}\widetilde{V}_{acid}\kappa^{d}_{ck}t^{db}_{kj} - P_{ab}\sum_{\substack{k\\cd}}\widetilde{V}_{cakd}\kappa^{d}_{ck}t^{db}_{ij} + P_{ij}\sum_{\substack{kl\\c}}\widetilde{V}_{clki}\kappa^{d}_{ck}t^{ab}_{lj} + P_{ij}P_{ab}\sum_{\substack{k\\cd}}\widetilde{V}_{cbid}\kappa^{d}_{ck}t^{ab}_{kj} \\
&- \sum_{\substack{kl\\c}}\widetilde{V}_{clij}\kappa^{d}_{ck}t^{ab}_{kl} + \sum_{\substack{k\\cd}}\widetilde{V}_{abkd}\kappa^{d}_{ck}t^{cd}_{ij} - P_{ij}P_{ab}\sum_{\substack{kl\\c}}\widetilde{V}_{alkj}\kappa^{d}_{ck}t^{cb}_{il} + \frac{1}{2}P_{ij}\sum_{\substack{kl\\cde}}\widetilde{V}_{lcde}\kappa^{d}_{ck}t^{ab}_{il}t^{de}_{jk} \\
&- P_{ij}\sum_{\substack{klm\\cd}}\widetilde{V}_{lmdk}\kappa^{d}_{ck}t^{ab}_{il}t^{dc}_{jm} + P_{ab}\sum_{\substack{kl\\cde}}\widetilde{V}_{lcde}\kappa^{d}_{ck}t^{ad}_{ij}t^{be}_{lk} - \frac{1}{2}P_{ab}\sum_{\substack{klm\\cd}}\widetilde{V}_{lmdk}\kappa^{d}_{ck}t^{ad}_{ij}t^{bc}_{lm} \\
&- P_{ij}P_{ab}\sum_{\substack{kl\\cde}}\widetilde{V}_{kdce}\kappa^{d}_{dl}t^{ac}_{ik}t^{eb}_{lj} + \frac{1}{2}P_{ij}\sum_{\substack{kl\\cde}}\widetilde{V}_{kdce}\kappa^{d}_{dl}t^{ce}_{ki}t^{ab}_{lj} + \frac{1}{2}\sum_{\substack{kl\\cde}}\widetilde{V}_{ldce}\kappa^{d}_{dk}t^{ab}_{kl}t^{ce}_{ij} \\
&+ P_{ij}P_{ab}\sum_{\substack{klm\\cd}}\widetilde{V}_{kmcl}\kappa^{d}_{dl}t^{ac}_{ik}t^{db}_{mj} - \frac{1}{2}P_{ab}\sum_{\substack{klm\\cd}}\widetilde{V}_{kmcl}\kappa^{d}_{dl}t^{ca}_{km}t^{db}_{ij} - \frac{1}{2}\sum_{\substack{klm\\cd}}\widetilde{V}_{kmdl}\kappa^{d}_{cl}t^{cd}_{ij}t^{ab}_{km}\overline{C}_{abij} - \omega X^{ab}_{ij}
\end{aligned}
\tag{A.2}
$$

A.1.3 κ^d Equation

$$
\begin{aligned}
0 = &+ \sum_{\substack{j\\b}} \overline{V}_{ijab}\kappa^e_{jb} - \sum_{\substack{jk\\bc}} \overline{V}_{ibck}\kappa^e_{jc}\lambda^{jk}_{ab} - \sum_{\substack{jk\\bc}} \overline{V}_{kcaj}\kappa^e_{kb}\lambda^{ij}_{bc} + \frac{1}{2}\sum_{\substack{j\\bcd}} \overline{V}_{bcad}\kappa^e_{jd}\lambda^{ij}_{bc} \\
&+ \frac{1}{2}\sum_{\substack{jkl\\b}} \overline{V}_{iljk}\kappa^e_{lb}\lambda^{jk}_{ab} - \frac{1}{2}\sum_{\substack{jkl\\bc}} \overline{W}_{lbicjk}\kappa^e_{lc}\lambda^{jk}_{ba} + \frac{1}{2}\sum_{\substack{jk\\bcd}} \overline{W}_{kbcdja}\kappa^e_{kd}\lambda^{ji}_{bc} - \frac{1}{2}\sum_{\substack{jkl\\bc}} \overline{W}_{iblajk}\kappa^e_{lc}\lambda^{jk}_{bc} \\
&+ \frac{1}{2}\sum_{\substack{jk\\bcd}} \overline{W}_{ibcajd}\kappa^e_{kd}\lambda^{jk}_{bc} - \frac{1}{2}\sum_{\substack{jk\\bc}} \overline{F}_{ic}X^{cb}_{jk}\lambda^{jk}_{ab} - \frac{1}{2}\sum_{\substack{jk\\bc}} \overline{F}_{ka}X^{bc}_{kj}\lambda^{ij}_{bc} + \sum_{\substack{jkl\\bc}} \overline{V}_{ilck}X^{cb}_{jl}\lambda^{jk}_{ab} \\
&- \frac{1}{4}\sum_{\substack{jk\\bcd}} \overline{V}_{ibcd}X^{cd}_{jk}\lambda^{jk}_{ab} + \frac{1}{4}\sum_{\substack{jkl\\bc}} \overline{V}_{klaj}X^{bc}_{kl}\lambda^{ij}_{bc} - \sum_{\substack{jk\\bcd}} \overline{V}_{kcad}X^{bd}_{kj}\lambda^{ij}_{bc} - \frac{1}{2}\sum_{\substack{jkl\\bc}} \overline{V}_{ilaj}X^{bc}_{lk}\lambda^{jk}_{bc} \\
&+ \frac{1}{2}\sum_{\substack{jk\\bcd}} \overline{V}_{ibad}X^{dc}_{jk}\lambda^{jk}_{bc} - \sum_{b} \widetilde{F}_{ba}\kappa^d_{bi} + \sum_{j} \widetilde{F}_{ij}\kappa^d_{aj} - \sum_{\substack{j\\b}} \widetilde{V}_{ibaj}\kappa^d_{bj} + \frac{1}{2}\sum_{\substack{jk\\bc}} \widetilde{V}_{bcjk}\kappa^d_{bi}\lambda^{jk}_{ac} \\
&+ \frac{1}{2}\sum_{\substack{jk\\bc}} \widetilde{V}_{bcjk}\kappa^d_{aj}\lambda^{ik}_{bc} + \frac{1}{2}\sum_{\substack{jk\\bcd}} \widetilde{F}_{da}\kappa^d_{dk}t^{bc}_{jk}\lambda^{ji}_{bc} - \frac{1}{2}\sum_{\substack{jkl\\bc}} \widetilde{F}_{il}\kappa^d_{cl}t^{bc}_{jk}\lambda^{jk}_{ba} + \frac{1}{2}\sum_{\substack{jk\\bcd}} \widetilde{F}_{bd}\kappa^d_{bi}t^{dc}_{jk}\lambda^{jk}_{ac} \\
&- \frac{1}{2}\sum_{\substack{jkl\\bc}} \widetilde{F}_{lj}\kappa^d_{aj}t^{cb}_{lk}\lambda^{ik}_{cb} + \frac{1}{2}\sum_{\substack{jkl\\bcd}} \widetilde{V}_{icdl}\kappa^d_{cl}t^{bd}_{jk}\lambda^{jk}_{ba} + \frac{1}{2}\sum_{\substack{jkl\\bcd}} \widetilde{V}_{ldak}\kappa^d_{da}t^{bc}_{jl}\lambda^{ji}_{bc} + \frac{1}{2}\sum_{\substack{jkl\\bcd}} \widetilde{V}_{ibaj}\kappa^d_{bk}t^{cd}_{kl}\lambda^{jl}_{cd} \\
&+ \frac{1}{2}\sum_{\substack{jkl\\bcd}} \widetilde{V}_{ibaj}\kappa^d_{cj}t^{cd}_{kl}\lambda^{kl}_{bd} - \sum_{\substack{jkl\\bcd}} \widetilde{V}_{ibdk}\kappa^d_{bl}t^{dc}_{jl}\lambda^{jk}_{ac} - \frac{1}{2}\sum_{\substack{jkl\\bcd}} \widetilde{V}_{ibdl}\kappa^d_{cl}t^{dc}_{jk}\lambda^{jk}_{ab} - \frac{1}{2}\sum_{\substack{jkl\\bcd}} \widetilde{V}_{lcaj}\kappa^d_{ck}t^{bd}_{lk}\lambda^{ij}_{bd} \\
&- \sum_{\substack{jkl\\bcd}} \widetilde{V}_{lcak}\kappa^d_{dk}t^{bd}_{lj}\lambda^{ij}_{bc} - \frac{1}{2}\sum_{\substack{jk\\bcde}} \widetilde{V}_{cdea}\kappa^d_{di}t^{be}_{jk}\lambda^{jk}_{bc} - \frac{1}{2}\sum_{\substack{jklm\\bc}} \widetilde{V}_{mikl}\kappa^d_{al}t^{bc}_{jm}\lambda^{jk}_{bc} - \sum_{\substack{jk\\bcde}} \widetilde{V}_{bcae}\kappa^d_{cj}t^{cd}_{jk}\lambda^{ik}_{bd} \\
&- \sum_{\substack{jklm\\bc}} \widetilde{V}_{imjk}\kappa^d_{bk}t^{bc}_{ml}\lambda^{jl}_{ac} + \sum_{\substack{jkl\\bcd}} \widetilde{V}_{kdcl}\kappa^d_{al}t^{bc}_{jk}\lambda^{ji}_{bd} + \sum_{\substack{jkl\\bcd}} \widetilde{V}_{kdcl}\kappa^d_{di}t^{bc}_{jk}\lambda^{jl}_{ba} + \frac{1}{4}\sum_{\substack{jklm\\bc}} \widetilde{V}_{kmjl}\kappa^d_{al}t^{bc}_{km}\lambda^{ji}_{bc} \\
&+ \frac{1}{4}\sum_{\substack{jk\\bcde}} \widetilde{V}_{bdce}\kappa^d_{di}t^{ce}_{jk}\lambda^{jk}_{ba} + \frac{1}{2}\sum_{\substack{j\\bc}} \overline{V}_{bcja}Y^{ji}_{bc} - \frac{1}{2}\sum_{\substack{jk\\b}} \overline{V}_{bijk}Y^{jk}_{ba} + \frac{1}{4}\sum_{\substack{jk\\bc}} \overline{W}_{ibcajk}Y^{jk}_{bc} - \overline{C}_{ia} \\
&- \frac{1}{2}\sum_{\substack{j\\bc}} \overline{C}_{cbaj}\lambda^{ij}_{cb} + \frac{1}{2}\sum_{\substack{jk\\b}} \overline{C}_{ibkj}\lambda^{kj}_{ab} - \omega\kappa^d_{ai} + \frac{1}{2}\omega\sum_{\substack{jk\\bc}} \kappa^d_{ak}t^{bc}_{jk}\lambda^{ji}_{bc} + \frac{1}{2}\omega\sum_{\substack{jk\\bc}} \kappa^d_{ci}t^{bc}_{jk}\lambda^{jk}_{ba}
\end{aligned}
\tag{A.3}
$$

A.1.4 Y_2 Equation

$$
\begin{aligned}
0 = &-P_{ij}\sum_{\substack{k\\c}}\overline{F}_{jc}\kappa^e_{kc}\lambda^{ik}_{ab} - P_{ab}\sum_{\substack{k\\c}}\overline{F}_{kb}\kappa^e_{kc}\lambda^{ij}_{ac} + P_{ij}P_{ab}\sum_{\substack{kl\\c}}\overline{V}_{ljak}\kappa^e_{lc}\lambda^{ik}_{cb} - \sum_{\substack{k\\cd}}\overline{V}_{kdab}\kappa^e_{lc}\lambda^{ij}_{cd}\\
&+\sum_{\substack{kl\\c}}\overline{V}_{ijcl}\kappa^e_{kc}\lambda^{kl}_{ab} - P_{ij}P_{ab}\sum_{\substack{k\\cd}}\overline{V}_{icdb}\kappa^e_{kd}\lambda^{kj}_{ac} + P_{ab}\sum_{\substack{k\\cd}}\overline{V}_{kcda}\kappa^e_{kd}\lambda^{ij}_{cb} - P_{ij}\sum_{\substack{kl\\c}}\overline{V}_{lick}\kappa^e_{lc}\lambda^{kj}_{ab}\\
&-\frac{1}{2}P_{ij}\sum_{\substack{kl\\cd}}\overline{V}_{jlcd}X^{cd}_{kl}\lambda^{ik}_{ab} - \frac{1}{2}P_{ab}\sum_{\substack{kl\\cd}}\overline{V}_{klbd}X^{cd}_{kl}\lambda^{ij}_{ac} - \frac{1}{2}P_{ij}\sum_{\substack{kl\\cd}}\overline{V}_{ljab}X^{cd}_{kl}\lambda^{ki}_{cd}\\
&-\frac{1}{2}P_{ab}\sum_{\substack{kl\\cd}}\overline{V}_{ijdb}X^{cd}_{kl}\lambda^{kl}_{ca} + P_{ij}P_{ab}\sum_{\substack{kl\\cd}}\overline{V}_{jlbd}X^{dc}_{lk}\lambda^{ik}_{ac} + \frac{1}{4}\sum_{\substack{kl\\cd}}\overline{V}_{ijcd}X^{cd}_{kl}\lambda^{kl}_{ab} + \frac{1}{4}\sum_{\substack{kl\\cd}}\overline{V}_{klab}X^{cd}_{kl}\lambda^{ij}_{cd}\\
&+P_{ab}\sum_{k}\widetilde{V}_{ijak}\kappa^d_{bk} - P_{ij}\sum_{c}\widetilde{V}_{icab}\kappa^d_{cj} + P_{ij}\sum_{\substack{k\\c}}\widetilde{F}_{ck}\kappa^d_{ci}\lambda^{kj}_{ab} + P_{ab}\sum_{\substack{k\\c}}\widetilde{F}_{ck}\kappa^d_{ak}\lambda^{ij}_{cb}\\
&+P_{ij}\sum_{\substack{kl\\c}}\widetilde{V}_{cikl}\kappa^d_{ck}\lambda^{lj}_{ab} - P_{ab}\sum_{\substack{k\\cd}}\widetilde{V}_{cdka}\kappa^d_{ck}\lambda^{ij}_{db} + P_{ij}P_{ab}\sum_{\substack{kl\\c}}\widetilde{V}_{cikl}\kappa^d_{al}\lambda^{kj}_{cb} - P_{ij}P_{ab}\sum_{\substack{k\\cd}}\widetilde{V}_{cdka}\kappa^d_{di}\lambda^{kj}_{cb}\\
&+\frac{1}{2}P_{ab}\sum_{\substack{k\\cd}}\widetilde{V}_{cdkb}\kappa^d_{ak}\lambda^{ij}_{cd} - \frac{1}{2}P_{ij}\sum_{\substack{kl\\c}}\widetilde{V}_{cjkl}\kappa^d_{ci}\lambda^{kl}_{ab} - P_{ij}P_{ab}\sum_{\substack{kl\\cde}}\widetilde{V}_{jcbe}\kappa^d_{ck}t^{ed}_{kl}\lambda^{il}_{ad}\\
&+P_{ij}P_{ab}\sum_{\substack{klm\\cd}}\widetilde{V}_{jmbk}\kappa^d_{ck}t^{cd}_{ml}\lambda^{il}_{ad} - P_{ij}P_{ab}\sum_{\substack{kl\\cde}}\widetilde{V}_{ldea}\kappa^d_{di}t^{ce}_{kl}\lambda^{kj}_{cb} + P_{ij}P_{ab}\sum_{\substack{klm\\cd}}\widetilde{V}_{midl}\kappa^d_{al}t^{cd}_{km}\lambda^{kj}_{cb}\\
&+\frac{1}{2}P_{ij}\sum_{\substack{kl\\cde}}\widetilde{V}_{ldab}\kappa^d_{dj}t^{ce}_{lk}\lambda^{ik}_{ce} + \frac{1}{2}P_{ab}\sum_{\substack{klm\\cd}}\widetilde{V}_{ijdk}\kappa^d_{bk}t^{dc}_{lm}\lambda^{lm}_{ac} + \frac{1}{2}P_{ij}\sum_{\substack{kl\\cde}}\widetilde{V}_{icde}\kappa^d_{cl}t^{de}_{kl}\lambda^{kj}_{ab}\\
&-\frac{1}{2}P_{ab}\sum_{\substack{klm\\cd}}\widetilde{V}_{lmak}\kappa^d_{dk}t^{cd}_{lm}\lambda^{ij}_{cb} + \frac{1}{2}\sum_{\substack{kl\\cde}}\widetilde{V}_{leab}\kappa^d_{ek}t^{cd}_{kl}\lambda^{ij}_{cd} - \frac{1}{2}\sum_{\substack{klm\\cd}}\widetilde{V}_{ijcm}\kappa^d_{bm}t^{bc}_{kl}\lambda^{kl}_{ab}\\
&+\frac{1}{4}P_{ij}\sum_{\substack{kl\\cde}}\widetilde{V}_{jdce}\kappa^d_{di}t^{ce}_{kl}\lambda^{kl}_{ab} - \frac{1}{4}P_{ab}\sum_{\substack{klm\\cd}}\widetilde{V}_{kmbl}\kappa^d_{al}t^{cd}_{km}\lambda^{ij}_{cd} + \sum_{c}\overline{F}_{cb}Y^{ij}_{ac} - \sum_{c}\overline{F}_{ca}Y^{ij}_{bc}\\
&-\sum_{k}\overline{F}_{jk}Y^{ik}_{ab} + \sum_{k}\overline{F}_{ik}Y^{jk}_{ab} + P_{ij}P_{ab}\sum_{\substack{k\\c}}\overline{V}_{icak}Y^{kj}_{cb} + \frac{1}{2}\sum_{cd}\overline{V}_{cdab}Y^{ij}_{cd} + \frac{1}{2}\sum_{kl}\overline{V}_{ijkl}Y^{kl}_{ab}\\
&+\frac{1}{2}P_{ij}\sum_{\substack{k\\cd}}\overline{W}_{icdakb}Y^{kj}_{cd} - \frac{1}{2}P_{ab}\sum_{\substack{kl\\c}}\overline{W}_{icjakl}Y^{kl}_{cb} - P_{ab}\sum_{c}\overline{C}_{cb}\lambda^{ij}_{ac} + P_{ij}\sum_{k}\overline{C}_{jk}\lambda^{ik}_{ab} + \omega Y^{ij}_{ab}
\end{aligned}
\tag{A.4}
$$

A.2 Response Function

$$\begin{aligned}\langle\langle A; V(\omega_1)\rangle\rangle = &+\overline{C}_{ia}\kappa^e_{ia} + \frac{1}{2}\sum_{\substack{j\\bc}}\overline{C}_{cbaj}\lambda^{ij}_{cb}\kappa^e_{ia} - \frac{1}{2}\sum_{\substack{jk\\b}}\overline{C}_{ibkj}\lambda^{kj}_{ab}\kappa^e_{ia} + P_{ab}\sum_c \overline{C}_{cb}\lambda^{ij}_{ac}X^{ab}_{ij}\\ &- P_{ij}\sum_k \overline{C}_{jk}\lambda^{ik}_{ab}X^{ab}_{ij} - \widetilde{C}_{ai}\kappa^d_{ai} + \frac{1}{2}\sum_{\substack{jk\\bc}}\widetilde{C}_{ci}t^{ba}_{jk}\lambda^{jk}_{bc}\kappa^d_{ai} + \frac{1}{2}\sum_{\substack{jk\\bc}}\widetilde{C}_{ak}t^{bc}_{ji}\lambda^{jk}_{bc}\kappa^d_{ai} + \widetilde{C}_{abij}Y^{ij}_{ab}\end{aligned} \tag{A.5}$$